The Astrophysical Journal Supplement Series, 264:7 (39pp), 2023 January https://doi.org/10.3847/1538-4365/ac9838

CCAT-prime Collaboration: Science Goals and Forecasts with Prime-Cam on the Fred Young Submillimeter Telescope

CCAT-Prime Collaboration[1], Manuel Aravena[2,1], Jason E. Austermann[3], Kaustuv Basu[4], Nicholas Battaglia[5], Benjamin Beringue[6], Frank Bertoldi[4], Frank Bigiel[4], J. Richard Bond[7], Patrick C. Breysse[8], Colton Broughton[9], Ricardo Bustos[10], Scott C. Chapman[11,12,13], Maude Charmetant[4], Steve K. Choi[5,14], Dongwoo T. Chung[7,15], Susan E. Clark[16,17], Nicholas F. Cothard[18], Abigail T. Crites[14], Ankur Dev[4], Kaela Douglas[9], Cody J. Duell[14], Rolando Dünner[19], Haruki Ebina[14], Jens Erler[4,20], Michel Fich[21], Laura M. Fissel[22], Simon Foreman[23,24], R. G. Freundt[5], Patricio A. Gallardo[14], Jiansong Gao[3], Pablo García[25,26], Riccardo Giovanelli[5], Joseph E. Golec[27], Christopher E. Groppi[28], Martha P. Haynes[5], Douglas Henke[13], Brandon Hensley[29], Terry Herter[5], Ronan Higgins[30], Renée Hložek[15,31], Anthony Huber[32], Zachary Huber[14], Johannes Hubmayr[3], Rebecca Jackson[27], Douglas Johnstone[9,13], Christos Karoumpis[4], Laura C. Keating[33], Eiichiro Komatsu[34,35], Yaqiong Li[14,36], Benjamin Magnelli[4,37], Brenda C. Matthews[9,13], Philip D. Mauskopf[28,38], Jeffrey J. McMahon[27,39,40,41], P. Daniel Meerburg[42], Joel Meyers[43], Vyoma Muralidhara[34], Norman W. Murray[7], Michael D. Niemack[5,14,36], Thomas Nikola[44], Yoko Okada[30], Roberto Puddu[19], Dominik A. Riechers[30], Erik Rosolowsky[45], Kayla Rossi[44], Kaja Rotermund[11], Anirban Roy[5], Sarah I. Sadavoy[22], Reinhold Schaaf[4], Peter Schilke[30], Douglas Scott[12], Robert Simon[30], Adrian K. Sinclair[28], Gregory R. Sivakoff[45], Gordon J. Stacey[5], Amelia M. Stutz[46,47], Juergen Stutzki[30], Mehrnoosh Tahani[23], Karun Thanjavur[9], Ralf A. Timmermann[4], Joel N. Ullom[3], Alexander van Engelen[28], Eve M. Vavagiakis[14], Michael R. Vissers[3], Jordan D. Wheeler[3], Simon D. M. White[34], Yijie Zhu[5], and Bugao Zou[18]

[1] CCAT Observatory Inc.
[2] Núcleo de Astronomía, Facultad de Ingeniería y Ciencias, Universidad Diego Portales, Av. Ejército 441, Santiago, Chile
[3] Quantum Sensors Group, National Institute of Standards and Technology, Boulder, CO 80305, USA
[4] Argelander Institute for Astronomy, University of Bonn, Auf dem Hügel 71, D-53121 Bonn, Germany
[5] Department of Astronomy, Cornell University, Ithaca, NY 14853, USA; stacey@astro.cornell.edu
[6] DAMTP, Centre for Mathematical Sciences, Wilberforce Road, Cambridge, CB3 0WA, UK
[7] Canadian Institute for Theoretical Astrophysics, University of Toronto, 60 St. George Street, Toronto, ON M5S 3H8, Canada
[8] Center for Cosmology and Particle Physics, Department of Physics, New York University, 726 Broadway, New York, NY 1003, USA
[9] Department of Physics and Astronomy, University of Victoria, 3800 Finnerty Road, Elliot Building, Victoria, BC, V8P 5C2, Canada
[10] Departamento de Ingeniería Eléctrica, Universidad Católica de la Santísima Concepción, Alonso de Ribera 2850, Concepción, Chile
[11] Dalhousie University, Halifax, NS B3H 4R2, Canada
[12] University of British Columbia, Vancouver, BC V6T 1Z1, Canada
[13] Herzberg Astronomy and Astrophysics Research Centre, National Research Council Canada, 5071 West Saanich Road, Victoria, BC, V9E 2E7, Canada
[14] Department of Physics, Cornell University, Ithaca, NY 14853, USA
[15] Dunlap Institute for Astronomy and Astrophysics, University of Toronto, 50 St. George Street, Toronto, ON M5S 3H4, Canada
[16] Department of Physics, Stanford University, Stanford, CA 94305, USA
[17] Kavli Institute for Particle Astrophysics & Cosmology, P.O. Box 2450, Stanford University, Stanford, CA 94305, USA
[18] Department of Applied and Engineering Physics, Cornell University, Ithaca, NY 14853, USA
[19] Instituto de Astrofísica and Centro de Astro-Ingeniería, Facultad de Física, Pontificia Universidad Católica de Chile, Av. Vicuña Mackenna 4860, 7820436, Macul, Santiago, Chile
[20] Deutsches Zentrum für Luft- und Raumfahrt e.V. (DLR) Projektträger, Joseph-Beuys-Allee 4, D-53113 Bonn, Germany
[21] Waterloo Centre for Astrophysics, Department of Physics and Astrophysics, University of Waterloo, Waterloo, ON N2L 3G1, Canada
[22] Department of Physics, Engineering Physics, and Astronomy, Queen's University, Kingston, ON K7L 3N6, Canada
[23] Dominion Radio Astrophysical Observatory, Herzberg Astronomy and Astrophysics Research Centre, National Research Council Canada, P.O. Box 248, Penticton, BC V2A 6J9, Canada
[24] Perimeter Institute for Theoretical Physics, 31 Caroline Street North, Waterloo, ON N2L 2Y5, Canada
[25] Chinese Academy of Sciences South America Center for Astronomy, National Astronomical Observatories, CAS, Beijing 100101, People's Republic of China
[26] Instituto de Astronomía, Universidad Católica del Norte, Av. Angamos 0610, Antofagasta 1270709, Chile
[27] Department of Astronomy and Astrophysics, University of Chicago, Chicago, IL 60637, USA
[28] School of Earth and Space Exploration, Arizona State University, Tempe, AZ 85287, USA
[29] Department of Astrophysical Sciences, Princeton University, Princeton, NJ 08544, USA
[30] I. Physikalisches Institut, Universität zu Köln, Zülpicher Str. 77, D-50937 Köln, Germany
[31] David A. Dunlap Department of Astronomy and Astrophysics, University of Toronto, 50 St. George Street, Toronto ON M5S3H4, Canada
[32] Department of Physics and Astronomy, University of Lethbridge, Alberta, Canada
[33] Leibniz Institute for Astrophysics Potsdam (AIP), An der Sternwarte 16, 14482 Potsdam, Germany
[34] Max-Planck-Institut für Astrophysik, Karl-Schwarzschild Str. 1, D-85741 Garching, Germany
[35] Kavli Institute for the Physics and Mathematics of the Universe (Kavli IPMU, WPI), University of Tokyo, Chiba 277-8582, Japan
[36] Kavli Institute at Cornell for Nanoscale Science, Cornell University, Ithaca, NY 14853, USA
[37] AIM, CEA, CNRS, Université Paris-Saclay, Université Paris Diderot, Sorbonne Paris Cité, F-91191 Gif-sur-Yvette, France
[38] Department of Physics, Arizona State University, Tempe, AZ 85287, USA
[39] Kavli Institute for Cosmological Physics, University of Chicago, Chicago, IL 60637, USA
[40] Department of Physics, University of Chicago, Chicago, IL 60637, USA
[41] Enrico Fermi Institute, University of Chicago, Chicago, IL 60637, USA
[42] Van Swinderen Institute for Particle Physics and Gravity, University of Groningen, Nijenborgh 4, 9747 AG Groningen, The Netherlands
[43] Department of Physics, Southern Methodist University, 3215 Daniel Ave, Dallas, TX 75275, USA
[44] Cornell Center for Astrophysics and Planetary Sciences, 210 Space Sciences Building, Cornell University, Ithaca, NY 14853, USA
[45] Department of Physics, University of Alberta, CCIS 4-181, Edmonton, AB T6G 2E1, Canada
[46] Departamento de Astronomía, Universidad de Concepción, Casilla 160-C, Concepción, Chile

[47] Max-Planck-Institut für Astronomie, Königstuhl 17, D-69117 Heidelberg, Germany
Received 2021 July 16; revised 2022 July 11; accepted 2022 October 5; published 2022 December 16

Abstract

We present a detailed overview of the science goals and predictions for the Prime-Cam direct-detection camera–spectrometer being constructed by the CCAT-prime collaboration for dedicated use on the Fred Young Submillimeter Telescope (FYST). The FYST is a wide-field, 6 m aperture submillimeter telescope being built (first light in late 2023) by an international consortium of institutions led by Cornell University and sited at more than 5600 m on Cerro Chajnantor in northern Chile. Prime-Cam is one of two instruments planned for FYST and will provide unprecedented spectroscopic and broadband measurement capabilities to address important astrophysical questions ranging from Big Bang cosmology through reionization and the formation of the first galaxies to star formation within our own Milky Way. Prime-Cam on the FYST will have a mapping speed that is over 10 times greater than existing and near-term facilities for high-redshift science and broadband polarimetric imaging at frequencies above 300 GHz. We describe details of the science program enabled by this system and our preliminary survey strategies.

Unified Astronomy Thesaurus concepts: Wide-field telescopes (1800); Astronomical instrumentation (799); Galaxy evolution (594); Reionization (1383); Protogalaxies (1298); Time domain astronomy (2109); Observational cosmology (1146); Interstellar dust (836); Star formation (1569); Sunyaev-Zeldovich effect (1654); Galaxy clusters (584); Recombination (cosmology) (1365)

1. Introduction

The CCAT-prime Collaboration is an international group of institutions led by Cornell University that is brought together by a common desire to address pressing astrophysical questions ranging from Big Bang cosmology and the large-scale structure of the universe, through the formation of the first stars and galaxies and on to the formation of stars and planetary systems in the Galaxy. These types of studies involve large-scale, high-sensitivity polarimetric, photometric, and spectroscopic mapping at frequencies spanning the electromagnetic spectrum. Indeed, a wide variety of such programs are ongoing or planned from the optical to the centimeter-wave bands (e.g., Rubin Observatory, Rubin, formerly LSST; Euclid, Roman Space Telescope, Roman, formerly WFIRST; ASKAP; Square Kilometer Array, hereafter SKA, etc.). We have undertaken the construction of a new high-efficiency, wide-field telescope, the Fred Young Submillimeter Telescope (FYST, pronounced *feest*), which together with its Prime-Cam instrument will enable wide-field and very deep mapping through the telluric windows from 100 to 900 GHz (3 to 0.33 millimeter wavelength). This spectral regime has been explored through a variety of surveys including those using ground-based telescopes (e.g., Caltech Submillimeter Observatory, James Clerk Maxwell Telescope (JCMT), APEX, South Pole Telescope (SPT), and Atacama Cosmology Telescope (ACT)) and space telescopes (e.g., Planck and Herschel) with many striking discoveries. With its 6 m aperture at a superb site, FYST and its associated instrumentation move beyond these surveys in terms of confusion-limited depth, areal coverage, and/or frequency coverage, enabling new science as well as greatly expanding the science returns from these surveys and those at other frequencies. Within this paper, we outline the science plans for FYST focusing on the following science programs:

1. *Epoch of reionization.* The first stars and galaxies dominated reionization processes during the epoch of reionization (EoR) at $6 \lesssim z \lesssim 20$. Stars form at local overdensities of matter so that, if we can trace the star formation (SF) process, we both trace the history of star and galaxy formation and the growth of large-scale structure, which is governed by fundamental physics in the evolving universe. The [C II] 1.901 THz (158 μm) and [O III] 3.393 THz (88 μm) fine-structure lines are exceptionally luminous and provide uniquely powerful probes of SF in the early universe. These lines are redshifted into the FYST windows by the cosmic expansion because the EoR, and the aggregate line emission from faint galaxies tomographically, reveals the large-scale structure of reionization and the galaxy assembly process (see Section 4).
2. *Tracing galaxy evolution over cosmic time.* Half the SF in the universe over cosmic time is obscured to optical–UV observers by the presence of dust. The dust is heated by stellar photons and reradiates its energy in the far-infrared (FIR), with its spectral energy distribution typically peaking at frequencies from 2 to 6 THz. Tracing this power peak reveals the star-forming luminosity of these dusty star-forming galaxies (DSFGs). This power peak is shifted into the FYST windows at redshifts at and beyond the peak of cosmic SF activity, so-called *cosmic noon* at $1 \leqslant z \leqslant 3$. Therefore, by mapping the 3D distribution and energetics of DSFGs, we track the process of galaxy assembly and the evolving structure of the universe from times between the EoR through Cosmic Noon, when dark energy begins to have important impacts on the expansion (see Section 5).
3. *Measuring CMB foregrounds.* The scale of structures in the cosmic microwave background (CMB) are controlled by the fundamental physics of the universe. For instance, wide-field mapping of the CMB has revealed that the universe is flat, it is 13.8 Gyrs old, and its energy content is about 5% matter, 27% dark matter (DM), and 68% dark energy. Encoded within the polarization patterns and scales of the CMB are signals that reflect the earliest moments of the expansion. In particular, B-mode

polarization patterns promise to constrain models of cosmic inflation. Unfortunately, strong B-mode patterns are present in foreground emission as well (e.g., dust emission from the Milky Way, hereafter MW), so the measurement of primordial B-modes is very challenging. FYST is uniquely suited to unravelling this foreground emission from the CMB B-mode emission with its access to the high-frequency submillimeter-wavelength bands (see Section 6).

4. *Galactic polarization.* Magnetic fields help govern the accumulation and collapse of neutral gas within galaxies and therefore play an important role in regulating the SF process. Magnetic fields are probed in several ways: spectroscopically through, for example, Zeeman splitting of line emission or absorption; selective extinction of starlight due to aligned dust grains in the visible–IR; synchrotron emission; or the rotational measures of radio emission from background pulsars. These probes have their limits—extinction for visible light, and limited lines of sight and appropriate excitation conditions for Zeeman splitting or rotation measure (RM) observations. Magnetic fields are also traced through linearly polarized thermal dust emission in the FIR to millimeter-wave bands from dust grains aligned with respect to the local magnetic field. The degree of polarization and its morphology reflect intrinsic grain properties and the underlying magnetic field direction, strength, and energetic importance relative to turbulence and gravity. Dust emission arises from all phases of the interstellar medium (ISM), and FYST provides the platform to trace this radiation continuously from kiloparsec to the subparsec scales at which individual stars form (see Section 7).
5. *Galaxy-cluster evolution.* The CMB is also a backlight for studies of large-scale structure and galaxy assembly through the inverse Compton scattering of CMB photons off of hot electrons deep in the gravitational wells of galaxy clusters. This energy-shifting of CMB photons, called the Sunyaev–Zel'dovich (SZ) effect, is used to trace the mass, spatial distribution, and peculiar motions of these clusters, which are the most massive self-gravitating structures in the universe. The SZ effect centers at 220 GHz in the millimeter-wave bands, and its spectrum is very effectively mapped through the FYST windows (see Section 8).
6. *Rayleigh scattering.* The process of recombination was not instantaneous. Neutral hydrogen and helium atoms began to appear early in the recombination epoch and could then Rayleigh scatter the CMB radiation, producing a frequency-dependent signal that traces the cosmic structure during the epoch of recombination. The detection of this signal is quite challenging but made more manageable with the broad frequency coverage of the Prime-Cam on FYST (see Section 9).
7. *Time domain phenomena.* Time domain astrophysics is an exciting area of research that is being reinvigorated by the new generation of large-field survey facilities spanning the electromagnetic spectrum. While typically discovered at other frequencies, the understanding of very energetic transients such as supernovae (SNe), gamma-ray bursts (GRBs), X-ray binaries, merging neutron stars, and tidal disruption events (TDEs) will benefit greatly from the FYST spectral coverage, which, for example, can trace shocks and energy deposition in the enveloping circumstellar or ISM. The utility of the submillimeter bands is especially evident for dust-enshrouded sources such as protostars, where changes in the submillimeter brightness likely reflect the heating of the enshrouding protostellar core by the accretion luminosity of matter flowing onto the protostar itself (see Section 10).

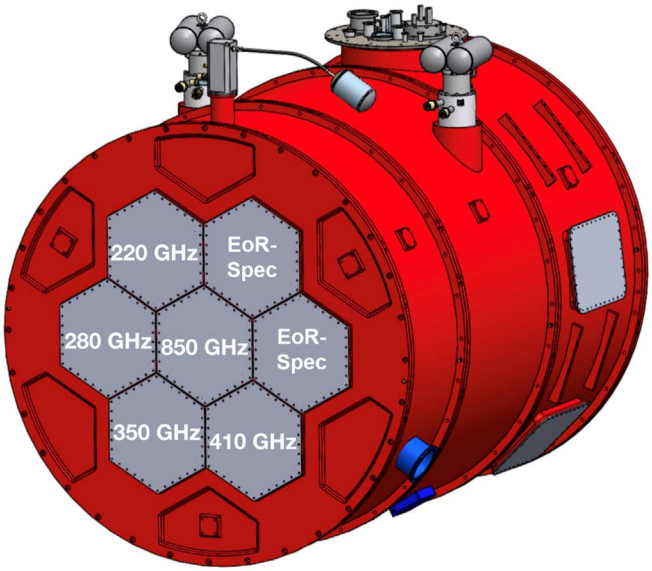

Figure 1. Prime-Cam instrument design showing the placement of the seven instrument module entrance windows including the five polarization-sensitive modules at nominal band center frequencies from 220 to 850 GHz, and the two spectrometer (EoR-Spec) modules. (Vavagiakis et al. 2018).

FYST, with its 6 m aperture, wide field-of-view design, as well as its location at more than 5600 m elevation on Cerro Chajnantor in northern Chile (Parshley et al. 2018a, 2018b), and together with Prime-Cam (Vavagiakis et al. 2018), is uniquely well suited to pursue these science programs. The aperture is appropriate for diffraction-limited imaging with a beam size appropriate for our studies, especially the CMB B-mode polarization and submegaparsec scales for line intensity mapping (LIM) experiments. Prime-Cam imaging arrays take advantage of the wide field of view of FYST to yield mapping speeds that are over 10 times greater than existing and near-term facilities for the various experiments.

The paper is organized as follows: First we describe the Prime-Cam instrument, the camera optics, the spectrometer design, the arrays, and expected performance (Section 2). Next, the surveys to address the science goals are presented in Section 3. Then, each science program and its goal that we expect to accomplish with these surveys in the context of a 5 yr observing plan is presented in detail in Sections 4 to 10. We summarize the paper in Section 11.

2. Instrument Overview

The Prime-Cam instrument is designed to fill the central 4.°9 of the 8° diameter field of view delivered by the FYST (Niemack 2016; Parshley et al. 2018a). To do so, the field is split up into seven independent instrument modules, with six modules arranged in a compact configuration around a central module (Figure 1). Each module fills up to a 1.°3 diameter field of view, and is separated from its neighbors by 1.°8 within a 1.8 m diameter cryostat. Externally, the instrument modules are

close to identical, but the interiors are independently optimized with regard to optical elements and detectors for specific science programs. The baseline plan for the Prime-Cam modules includes the following: two imaging spectrometer modules that use Fabry–Perot interferometers (FPIs) for LIM from 210 to 420 GHz, and five broadband polarization-sensitive modules for observations at five frequencies (220, 280, 350, 410, and 850 GHz; Choi et al. 2020a). Each module is contained within a cylindrical casing ∼45 cm in diameter and ∼1.6 m long (Vavagiakis et al. 2018).

2.1. Optical Design

The seven entrance window, silicon optics design of the instrument modules is similar to ideas put forth for the proposed 25 m CCAT telescope (Stacey et al. 2014). These ideas evolved through collaboration with the Simons Observatory (SO) project (Dicker et al. 2018; Simons Observatory Collaboration 2019) into the nearly interchangeable instrument module design for Prime-Cam (Vavagiakis et al. 2018). Each module has a roughly 40 cm diameter entrance window made of ultra-high-molecular-weight polyethylene that has been antireflection (AR) coated with a layer of expanded Teflon. The focus of FYST is about 20 cm inside of the window of each module. Within the module are lenses and the optical filters that are required to block unwanted radiation. Each of the lenses and filters are thermally attached to the temperature bus (80, 40, 4, or 0.1 K) appropriate for their function. The powered optics include a field lens near the FYST focus followed by a pair of plano-convex lenses. The first of these lenses forms a pupil image at about 20 cm diameter, and the second reimages the beam onto the detector array at $f/2.0$. The FPI optics incorporate an additional powered lens to provide the smaller (14 cm) diameter pupil and more collimated illumination required by the FPI relative to the broadband cameras. Lenses are made from high-purity silicon with metamaterial AR coatings (Datta et al. 2013). High resistivity silicon has a high index of refraction and, at low temperatures, has both very low optical loss to millimeter-wave radiation and high thermal conductivity. These properties combined enable the manufacturing of the large diameter (∼40 cm) optical components that are required for our instrument modules that can be kept uniformly cool, resulting in both high transmission and very low thermal emission.

2.2. EoR-spec

The Epoch of Reionization Spectrometer (EoR-Spec) LIM modules are optimized to measure the 158 μm [C II] fine-structure line emission from $z = 8.05$ (which is within the EoR) to $z = 3.5$ (which is nearly at the peak of SF per unit comoving volume in the universe). The spectrometer is based on a cryogenic imaging FPI that spectrally scans this redshift interval detecting the [C II] line over wide fields (Cothard et al. 2020). Since the [C II] line tracks SF (Stacey et al. 1991, 2010), it reveals the reionization process that is driven by the first stars and galaxies *and* the subsequent growth and evolution of these early galaxies.

The FPI utilizes silicon-substrate-based mirrors, a new technology that enables tuning of FPI cavity finesse so as to deliver near-uniform spectral resolving power and high efficiency over the octave bandwidth of the spectrometer (210 to 420 GHz; Cothard et al. 2018, 2020). The goal is a resolving power of ∼100. Each EoR-Spec module will have three focal-plane arrays. Two arrays will have architectures and filtration centered at 260 GHz for LIM from 210 to 315 GHz, while the third will be centered at 370 GHz for work at 315 to 425 GHz. The high frequency cutoffs for each array will be set by low-pass filters directly in front of the arrays, while the low-frequency cutoffs are set by the feedhorn design for each pixel in an array. The FPI will be set in second order to address the 260 GHz array so that the third-order fringe will be detected by the 370 GHz array.

2.3. Focal-plane Arrays

The primary technologies for large-scale arrays suitable for broadband polarimetry and photometry, or low-resolving-power spectroscopy in the submillimeter to millimeter-wave bands are transition-edge-sensor (TES) bolometers and kinetic inductance detectors (KIDs). While comparatively less mature, the KID technology is significantly easier to manufacture and read out than TES arrays, so that the costs per detector can be substantially smaller. Recent laboratory and on-sky measurements indicate that the KID technology can reach the fundamental background limits required for our instruments in large-format array architectures (Hubmayr et al. 2015; Calvo et al. 2016). Therefore, KID arrays have been adopted as the baseline technology for Prime-Cam (Duell et al. 2020).

The focal planes of each camera or EoR-Spec module are well populated with three KID arrays constructed on 150 mm silicon wafers in a tightly packed configuration (Vavagiakis et al. 2018). For each camera module, the three arrays will typically be identical, while, for the EoR-Spec modules, we will have two low-frequency arrays and one high-frequency array, as described above. The reason for this choice in EoR-Spec is that the low-frequency LIM signal is much more difficult to detect than the high-frequency (low-redshift) signal.

The arrays that we baseline for both the 280 and 350 GHz cameras and the corresponding bands in EoR-Spec are quite similar. Each element of the focal-plane array consists of a feedhorn, which defines the received radiation pattern (beam), coupled to a waveguide terminated by the TiN/Ti/TiN inductor of a KID. The inductor is designed to efficiently absorb the waveguide emission measure (EM) wave (Austermann et al. 2018; Duell et al. 2020). The absorber is fabricated over a backshort etched into a silicon-on-insulator wafer for optimal detector quantum efficiency. The major difference between the camera arrays and EoR-Spec arrays is that the camera arrays will be sensed in two polarizations by distinct KIDs while the two polarizations are tied together in the EoR-Spec arrays to detect the total power through just one KID per feedhorn. For all arrays, we maximize the numbers of beams on the sky, consistent with efficient coupling to the astrophysical source and array readout limitations. Table 1 lists the detector counts for the five camera bands and the two EoR-Spec bands. More information about the Prime-Cam instrument is available in Vavagiakis et al. (2018), Choi et al. (2020a).

2.4. Noise Model

The expected sensitivities for each type of module are summarized in Table 1. We estimate the expected system sensitivity by first calculating the fundamental limits imposed by the presence of thermal backgrounds under the parameters imposed by the system as described within Stacey (2011).

Table 1
Sensitivity Estimates for Three Surveys

Broadband Channels Wide Survey (20,000 deg^2; 4000 hr)[a]								
ν (GHz)	$\Delta\nu$ (GHz)	Beam (arcseconds)	$N_{\rm det}$	NEI (Jy sr$^{-1}\sqrt{\rm s}$)	Sensitivity (μK-arcmin)	NET (μK $\sqrt{\rm s}$)	$N_{\rm white}$ (μK^2 sr)	$N_{\rm red}$ (μK^2 sr)
220	56	59	7938	3300	15	6.8	2.0×10^{-5}	0.021
280	60	47	10,368	5500	28	13	6.8×10^{-5}	0.14
350	35	37	20,808	14,600	107	48	9.4×10^{-4}	3.6
410	30	32	20,808	37,300	407	182	1.4×10^{-2}	22
850	97	15	20,808	479,000	680000	310,000	3.9×10^{4}	8.1×10^{6}

Broadband Channels for Star Formation Survey in First Quartile PWV (100 deg^2; 500 hr)[b]						
ν (GHz)	$\Delta\nu$ (GHz)	Beam (arcseconds)	$N_{\rm det}$	NEFD beam^{-1} (mJy $\sqrt{\rm s}$ beam^{-1})	$\sigma_{\rm survey}$ beam^{-1} Q1: (μJy beam^{-1})	$\sigma_{\rm survey}$ beam^{-1} Q1–Q3: (μJy beam^{-1})
220	56	59	7938	14/17/23	110	130
280	60	47	10,368	16/21/30	140	170
350	35	37	20,808	37/52/94	270	370
410	30	32	20,808	66/120/230	560	810
850	97	15	20,808	170/400/1700	3100	4900

DSS: Selected Spectrometer Channel Parameters[c]							
ν (GHz)	[C II] Redshift	$\Delta\nu$ (GHz)	Beam (arcseconds)	$N_{\rm beams}$	NEFD beam^{-1} (mJy $\sqrt{\rm s}$ beam^{-1})	NEI (Jy sr$^{-1}\sqrt{\rm s}$)	$N_{\rm white}$ (Mpc^3 Jy^2 sr^{-2})
220	7.64	2.2	58	6912	68/81/110	13,000	2.6×10^{9}
280	5.79	2.8	48	6912	64/81/120	18,000	4.9×10^{9}
350	4.43	3.5	37	6144	100/140/260	53,000	3.9×10^{10}
410	3.64	4.1	33	6144	140/230/470	98,000	1.2×10^{11}

Notes.
[a] The top table gives the properties, instantaneous sensitivities, and noise power spectrum parameters of broadband channels for the wide area survey (20,000 deg^2). All temperatures are given in CMB temperature units. $N_{\rm det}$ is the total number of KID detectors. For each beam, there is one detector per polarization, so the total number of beams on the sky $N_{\rm beams} = N_{\rm det}/2$. In all calculations, we assume a conservative 80% yield for the detectors so that the actual number of active beams on the sky is $0.8 \times N_{\rm det}/2$. The detector quantum efficiency is taken as 80%. The quoted sensitivities are the weighted average of the top three quartile (Q1, Q2, Q3) weather expectations. We use the zenith precipitable water vapor (PWV) quartile estimates derived from 350 μm radiometer measurements made over a 5 yr period at the FYST site (Radford & Peterson 2016; as recalibrated by Cortés et al. 2020). The values are 0.36, 0.67, and 1.28 mm zenith PWV in Q1, Q2, and Q3, respectively, averaged over the year. Sensitivity estimates refer to source elevations of 45° for all three tables.
[b] The middle table broadband sensitivities refer to the smaller field (100 deg^2) pilot DSFG survey (5.1), where the relevant units are Jy beam^{-1}. In the fifth column, the noise equivalent flux density (NEFD) is quoted for weather quartiles Q1–Q2–Q3. Columns (6) and (7) list the expected noise per beam in the star formation survey if the observations are restricted to Q1 or all three weather quartiles (Q1–Q3) respectively.
[c] The bottom table gives properties and sensitivities at four representative EoR-Spec frequencies. Here we feed both polarizations into a single KID so that $N_{\rm det} = N_{\rm beams}$. As for the middle table, the NEFD per beam in a given resolution element is quoted for Q1–Q2–Q3. The NEI is the average over the field of view and is taken as a weighted average over the top three weather quartiles. Calculation of $N_{\rm white}$ from NEI accounts for scanning of the full spectral range, so the 4000 hr survey time is divided up across the 42 spectral elements for each order of the EoR-Spec FPI. Note that the resolution bandwidth of EoR-Spec is equal to $\Delta\nu = \nu/R$, but the noise bandwidth is $\pi/2$ larger, because the FPI spectral profile is Lorentzian in form.

Important parameters include the following: the sky, telescope, and cryostat window emissivities; the sky, telescope, and instrumental transmission efficiencies; the thermal backgrounds that arise from within the instrument (expected to be small); the detector quantum efficiency; the numbers of polarizations accepted; and the spectral resolving power. The result is then degraded by mixing in the expected detector noise in quadrature. The system performance is further degraded by the noise angular power spectrum in the atmospheric transmission commonly referred to as *sky noise*. The integrated angular noise power spectrum is given by

$$N_\ell = N_{\rm red}\left(\frac{\ell}{\ell_{\rm knee}}\right)^{\alpha_{\rm knee}} + N_{\rm white},$$

with $N_{\rm red}$ and $N_{\rm white}$ given in Table 1 for $\ell_{\rm knee} = 1000$, and $\alpha_{\rm knee} = -3.5$ for the temperature noise power spectrum (Simons Observatory Collaboration 2019; Choi et al. 2020a). For the polarization noise power spectrum, we use $N_{\rm red} = N_{\rm white}$ (multiplied by 2 to account for polarization noise), and $\ell_{\rm knee} = 700$, and $\alpha_{\rm knee} = -1.4$. Mapping speed is calculated based on the number of beams per instrument module on the sky taking into account the expected pixel yields.

For convenience, we include sensitivities calculated both in units of noise equivalent temperature (NET) and noise equivalent intensity (NEI). The NET unit (μK$\sqrt{\rm s}$) is appropriate for CMB-based studies, while the NEI unit (Jy sr^{-1} $\sqrt{\rm s}$) is appropriate for studies based on dust or spectral line emission. The sensitivities for the wide survey are given in CMB temperature units.

3. Surveys Mapping into Science

Multiple complementary surveys will be pursued with the seven instrument modules motivated by the variety of science programs outlined below. Different science programs call for different science survey strategies and instrument modules. It is

Table 2
Overview of Planned Survey Regions (See Figure 2) and Observing Parameters

Survey	Field(s) or Targets	Area (deg^2)	Time (10^2 hr)	Science Case	Supporting Surveys[a]	Section Number
DSS	E-COSMOS	4	20	Reionization LIM	(1), (2)	4
	and E-CDFS	4	20	Galaxy Evolution		5
				Time Domain Astrophysics		10
WFS	AdvACT/SO	20,000	40	Primordial Gravitational Waves	(3)	6
				Galaxy Evolution		5
				Galactic Polarization Science		7
				Galaxy-cluster Evolution via SZ		8
				Rayleigh Scattering		9
				Time Domain Astrophysics		10
CIB-Mid	GAMA	100	5	CIB Galaxy Evolution		5
GalPol	MW and LMC ISM and clouds	125	5.25	Galactic Polarization Science		7
PS Monitor	MW clouds and protostars	10×4	5	Episodic Protostellar Accretion		10

Note.
[a] (1) Deep Subaru HSC+PFS spectroscopy (current) and COSMOS X-Ray-to-meter-wave multiwavelength survey; (2) deep Euclid grism spectroscopy (upcoming), HERA HI 21 cm (upcoming), and H-UDF/CDF-S multiwavelength surveys (including JWST guaranteed time observations); (3) Planck Collaboration Int. XI (2013), SDSS, DES, ACT (current), SO, DESI, Rubin, and eROSITA (upcoming).

critical to merge these surveys, with an eye toward synergies, into a complete plan covering the relevant sidereal times during the year with high observing efficiency. An overview of the planned surveys is presented in Table 2.

FYST will support two distinct science instruments during normal operations. The first, described here, is Prime-Cam with its camera and broadband, low-resolving-power direct-detection spectrometer modules. The second is the CCAT Heterodyne Array Instrument (CHAI; Graf et al. 2019), which is designed for high-efficiency velocity-resolved mapping of important diagnostic lines from the Galaxy and nearby galaxies in the high-frequency submillimeter windows. Approximately three-quarters and one-quarter of the FYST time on the sky will be devoted to Prime-Cam and CHAI observations, respectively. We plan block campaigns for Prime-Cam and CHAI instrumentation; the fundamental time unit of a block is likely to be 2 weeks. The two instruments cannot be operated simultaneously.

3.1. Operations

Based on long-term Chajnantor weather statistics, we estimate about 2500 hr yr^{-1} will be available for Prime-Cam science observations. Within our 5 yr plan, the total available time will be about 12,500 hr. We expect to devote up to 2500 hr to commissioning and early science activities, and the remaining 10,000 hr will be devoted to our baseline science, described below. Most of this time (8000 hr) will be spent on two large surveys, while an additional 2000 hr will be spent on focused and unique observational niche (e.g., location on sky, depth, or cadence) surveys.

3.2. Survey Overview

Our two large surveys (4000 hr each) are the Wide Field Survey (WFS), and the Deep Spectroscopic Survey (DSS). There are also smaller-scale surveys that we outline below.

The WFS is a 4000 hr wide-field survey, covering all declinations from $-61°$ to $+18°$ over the entire range of R.A. This survey will uniformly cover over 20,000 deg^2 and have high synergy with lower-frequency cosmological surveys envisioned for the SO and CMB Stage 4 survey (CMB-S4). It is optimized to address the science programs that we outline below: "Measuring CMB Foregrounds to Aid the Search for Primordial Gravitational Waves" (Section 6); "Probing Galaxy and Galaxy Cluster Evolution with Sunyaev–Zel'dovich Effects" (Section 8); and "Rayleigh Scattering: A New, Blue Surface of Last Scattering" (Section 9). Its broad spatial coverage includes a large fraction of the MW, enabling much of the "Galactic Polarization Science: Magnetic Fields and Dust Properties" (Section 7) and the time domain astrophysics (Section 10) science programs as well. The DSS is a 4000 hr survey that will yield very deep spectroscopic images of two fields (2000 hr each). It is designed to measure the growth of galaxies and large-scale structure as well as the process of reionization in the universe through [C II] and [O III] LIM, outlined in Section 4 "Reionization Intensity Mapping." This LIM will focus on two $\sim$4 deg^2 fields: the Extended-COSMOS (E-COSMOS; Aihara et al. 2018); and Extended Chandra Deep Field South (E-CDFS) field (Lehmer et al. 2005, which includes the Hubble Ultra Deep Field, or H-UDF; Beckwith et al. 2006).

These two major surveys deliver most of the science outlined in Section 5 "Tracing Galaxy Evolution from the First Billion Years to Cosmic Noon with the Cosmic Infrared Background," Section 7 "Galactic Polarization Science: Magnetic Fields and Dust Properties," and Section 10 "A New Submillimeter Window into Time Domain Astrophysics." Galaxy evolution studies have both shallow–large and deep–small area science requirements that are very well addressed by piggybacking its 850 GHz imaging onto both surveys above. The remaining time ($\sim$2000 hr) will be spent commissioning instrument modules and on first-light and/or demonstration science.

Each of the science programs outlined below will have components that cover either smaller fields or fields with shallower integration time requirements oriented toward first light and/or demonstration science. The Galaxy Evolution

program requires the addition of the middle-scale, middle-depth Galaxy and Mass Assembly (GAMA[48]) fields, which we call cosmic infrared background (hereafter CIB), CIB-Mid). The Galactic Polarization Science requires eight small-field observations of Galactic SF regions and the Large Magellanic Cloud (LMC), with deep integrations totalling about 525 hr (Galactic/LMC SF). The Time Domain Astrophysics program requires repeated short (1/2 hr) observations of 10 fields about 20 times year^{-1}, totalling about 500 hr (Protostar Monitoring Survey, hereafter PS Monitor). An overview of the planned surveys is presented in Table 2.

3.3. Scan Patterns

Prime-Cam will be mounted on the Nasmyth focus of the altitude-azimuth mounted FYST telescope. As such the field of view rotates with both the parallactic angle and the elevation of the telescope. Furthermore, all instrument modules except the 850 GHz camera module are off the optical axis by 1°.8 so that their 1°.3 fields will circulate at a radius of 1°.8 about the optical axis. As such, it is not trivial to optimize scan strategies or to calculate scan efficiencies. Optimization involves understanding the complex interplay between instantaneous field of view, the science field rotation during an observation, cross-linking of polarization knowledge (for polarimetry), cross-linking of spectral sampling (for spectral scanning), and pointing knowledge and stability under both the uniform motion and acceleration of the telescope. Coupled into these science requirements and telescope performance parameters are the noise spectrum of the detectors and that of the sky, which fold into the scan speed required for minimizing sky noise. Sky noise is a function of wavelength and weather conditions and the required spatial scales needed to be recovered for the science case. The final scan pattern must be repeated until the desired sensitivity levels are reached. Here we define scan efficiency as the fraction of time that is spent *on-source and pointed* relative to the wall-clock time, which includes the time *off-source and/or not well pointed*, which is presumed mostly to occur in the turnaround events. Clearly these are complex optimizations. Much thought has already been invested in WFS-like surveys with constant elevation scans by Advanced ACTPol, SO, and CMB-S4 (Stevens et al. 2018), and the WFS scan strategy will most likely employ a similar strategy. For these surveys, we estimated scan efficiencies in excess of 90%. The smaller-scale surveys (e.g., DSS) involve fields not much bigger than the instrument module field of view. For these fields, we will most likely adopt "daisy" or "pong" patterns widely used at the JCMT (Holland et al. 2013). Preliminary estimates of scan efficiencies for these modes are roughly 70%.

We have described the instrument and its capabilities and our survey strategies. The following sections discuss the seven primary areas of scientific focus that are enabled by this instrumentation and these surveys.

4. Reionization, Structure Growth, and Galaxy Emergence through Line-intensity Mapping

Intensity mapping is a technique that measures the spatial fluctuations of signals due to large-scale structure at low spatial resolution. The perhaps best-known examples of this application are the temperature and polarization fluctuation maps of the CMB as measured by COBE, Wilkinson Microwave Anisotropy Probe, and Planck. While CMB maps are integrated along the line of sight and thus do not contain 3D information without other assumptions, intensity mapping studies in spectral lines can recover redshift structure (and therefore measure signals at early epochs as a function of cosmic time). Compared to other intensity mapping techniques, spectral LIM therefore has the advantage of providing 3D spatial information about the sources of emission (or absorption) that can be used to probe the processes of structure formation. Intensity maps can also be used as cosmological probes, because the fluctuations in the emission–absorption lines are correlated with the underlying DM density fluctuations.

In Section 4.1, we describe the background and general concept of the intensity mapping survey planned with Prime-Cam. In Section 4.2, we provide additional details on science to be extracted from foregrounds in the survey. In Section 4.3, we describe the detailed survey strategy, and provide information on the ancillary data available in the survey fields. In Section 4.4, we give a detailed description on the methods used to extract the main survey signal. In Section 4.5, we give a detailed description on how to separate the main signal from foreground emission.

4.1. [C II] and [O III] Intensity Mapping in the Epoch of Reionization

The EoR, approximately $6 \leqslant z \leqslant 8$ to 20, is the last largely unexplored cosmic epoch in which stars and galaxies govern and shape the overall properties of the universe (Fan et al. 2006). With telescopes like Hubble Space Telescope and Atacama Large Millimeter/submillimeter Array (ALMA; and JWST in the near future), it has become possible to probe small samples of star-forming galaxies in the EoR. These studies provide compelling evidence that the first galaxies, which formed within the first billion years, are likely to be mostly responsible for cosmic reionization (e.g., Robertson et al. 2015). However, the overall properties of the sources of reionization and the connection between large-scale structure and the topology of reionization remain poorly understood (Finlator et al. 2009) because the main sources of reionization are numerous but intrinsically extremely faint (e.g., Robertson et al. 2013). It is therefore challenging to detect them individually. To make significant progress, large-scale 3D surveys of the universe during the EoR are of fundamental importance. Such surveys become possible by employing new observational strategies, in particular spectral LIM (Kovetz et al. 2017). Since intensity mapping detects the *aggregate* signal from faint but numerous sources, the sensitivity requirements are less demanding than those for individual source detection studies such as with ALMA or JWST, providing the potential for a shortcut toward detection with a carefully designed experiment (see model predictions by, e.g., Silva et al. 2015; Yue et al. 2015; Padmanabhan 2019).

21 cm H I EoR mapping was proposed as such a pathway a long time ago. Indeed, as shown by the claimed recent detection of the unexpectedly strong H I 21 cm absorption signal at $z \sim 17$ due to the first stars near the onset of reionization (Bowman et al. 2018), our current understanding is still incomplete, making direct measurements of all phases of reionization critical. These experiments are very challenging and easily contaminated by strong foregrounds. Also, while a firm detection of the cosmological H I signal should be within

[48] www.gama-survey.org

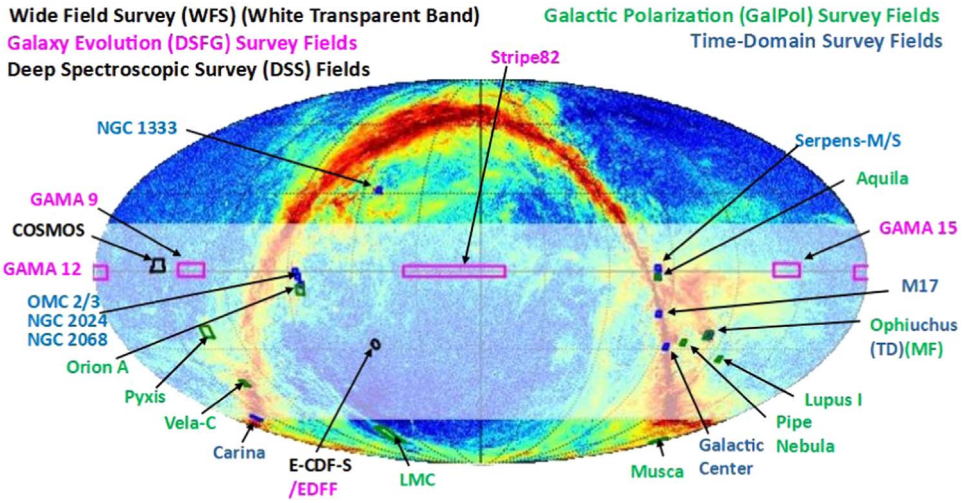

Figure 2. Overview of Prime-Cam survey fields in equatorial coordinates overlaid on the Planck dust polarization map (Planck Collaboration Int. XI 2013). The planned wide-field survey field for the CMB foregrounds, galaxy-cluster evolution, and Rayleigh-scattering science cases is approximated by the white transparent band (overlapping with Advanced ACTPol and SO fields; De Bernardis et al. 2016; Stevens et al. 2018). The deep intensity mapping–reionization surveys, the galaxy evolution survey fields, the galactic polarization science targets, and the specific time-domain science fields are outlined in black, magenta, green, and blue frames respectively. See Tables 2, 3, and 6 for survey coordinates, areas, and planned integration times.

reach with pathfinder experiments like HERA (DeBoer et al. 2017), a very large facility like the full SKA (Santos et al. 2015) is needed to reach the required mapping capabilities.

Promising complementary and alternative probes of the EoR are [C II] 158 μm and [O III] 88 μm LIM. The clear advantage of using these lines are that they much stronger than the H I 21 cm line, and it takes only a small single-dish telescope with wide field of view and modest resolution spectroscopic capabilities to map the line intensities. Additionally, these observations will not be hampered by radio frequency interference, a major concern for H I surveys. In contrast to traditional UV–optical diagnostic tracers (e.g., Lyα and Hα) that will be accessible to SPHEREx, the [C II] and [O III] signal will not be subject to absorption due to the increasingly neutral intergalactic medium (IGM) when probing deeper into the EoR or due to dust extinction in galaxies and along the line of sight (e.g., Silva et al. 2015; Yue et al. 2015). As described in more detail in Section 4.2, CO will be a powerful probe of structure at low to intermediate redshifts, up to the peak epoch of galaxy formation at $z = 1$–4. One concern for CO at higher redshifts is that the observable CO luminosity per unit H_2 mass is strongly affected by metallicity (e.g., Bolatto et al. 2013), which is expected to steeply drop in the EoR when galaxies first form. Thus, fine-structure lines like [C II] and [O III], which are significantly less affected, are perhaps the most promising pathway toward obtaining tomographic maps of the EoR in the near-term future. While [C II] typically is the strongest ISM emission line in star-forming galaxies (Stacey et al. 1991), [O III] 88 μm can be even stronger than [C II] in low-metallicity galaxies (e.g., Cormier et al. 2015), but it is expected to be weaker than the (factor of $\sim$2) lower-redshift [C II] line at the same observing frequencies. Compared to the 21 cm H I signal, which is primarily sensitive to the IGM, [C II] and [O III] have the advantage that they enable direct mapping of the distribution of the sources of reionization.

The EoR-Spec DSS survey is designed to obtain a tomographic map of the EoR through fluctuations in the aggregate clustering signal encoded in the [C II] cooling radiation from faint star-forming galaxies from $z \sim 3.5$ to 8.05 (e.g., Riechers et al. 2014; Hashimoto et al. 2018; see Figure 3), and through cross-correlation of [C II] and [O III] at $z > 7$ (and cross-correlation of [C II] and [O III] at lower redshift from balloon-based surveys similar to EXCLAIM; Ade et al. 2020; see also Padmanabhan et al. 2022). This can be done most efficiently with intermediate-size telescopes like FYST that have a spatial resolution matched to the key structures and very wide fields-of-view and can therefore map much more quickly than larger facilities. We will map a $\gtrsim$8 deg^2 region over at least two deep multiwavelength extragalactic survey fields (E-COSMOS and CDF-S/H-UDF; see Figure 2, Table 2, and Section 4.3). The full survey area will be sufficient to obtain a significant detection of the clustering signal in [C II] out to $z \sim 5$–8 (e.g., Silva et al. 2015; Yue et al. 2015; see Figure 3), and to enable cross-correlation at the high-redshift end with H I 21 cm maps from experiments like HERA covering some of the same fields. While direct detection of [O III] will likely be more challenging than [C II], cross-correlation of [O III] and H I could be a promising avenue to push to even higher redshifts.

4.2. CO Intensity Mapping from Present Day to the Peak Epoch of Star Formation

While the bright [C II] line from the EoR is the primary intensity mapping target for the EoR-Spec DSS survey, many other emission lines from different redshifts fall into the same frequency bands (Figure 4). Among the most important of these are lines emitted by carbon monoxide molecules. CO is the second most abundant molecule in the ISM and has a series of rotational transitions that are easily excited in typical molecular cloud conditions. The resulting emission lines are evenly spaced in energy, with frequencies $115 J_u$ GHz, where J_u is the upper angular momentum quantum number of the transition. Because CO lines are both bright and relatively accessible from the ground, they provide the primary means we have of probing molecular gas properties, and because molecular gas is the ISM phase that immediately precedes SF, observations of CO play a crucial role in understanding the ecosystems within and of galaxies across cosmic history (see reviews by, e.g., Kennicutt & Evans 2012; Bolatto et al. 2013; Carilli & Walter 2013; Heyer & Dame 2015).

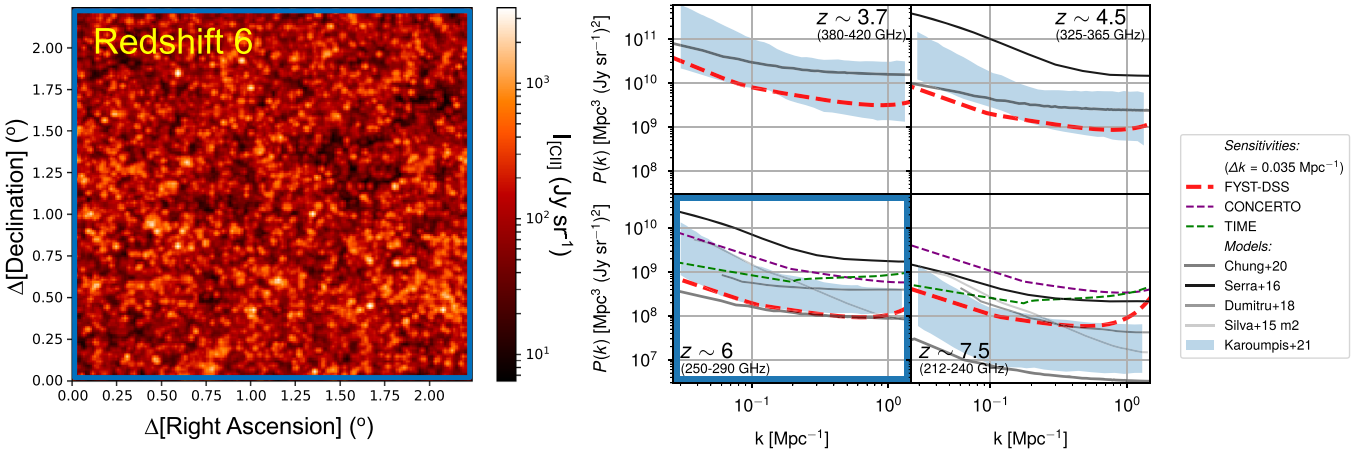

Figure 3. (Left) Simulated *redshift slice* of the area covered by the [C II] intensity mapping survey in the epoch of reionization (EoR), representing a small spectral bin (2.7 GHz wide, or $\Delta z = 0.07$ at the adopted redshift) within the vast $z = 3.5$–8.0 redshift range covered by the EoR-Spec DSS [C II] measurements. (Right) Power spectrum of the [C II] emission, revealing the topology of reionization and the [C II] luminosity functions at redshifts of 3.7 to 7.5. The range of recent model predictions (solid lines; Silva et al. 2015; Serra et al. 2016; Dumitru et al. 2019; Chung et al. 2020) differs by factors of 10 to 50, and an ensemble of state-of-the-art models from C. Karoumpis et al. (2021, in preparation) spans an order of magnitude in power spectrum predictions at each redshift. Overlaid are our predicted EoR-Spec sensitivities. Our proposed survey is as much as 10× more sensitive than other proposed surveys (TIME; Crites et al. 2014; Sun et al. 2021; CONCERTO; Concerto Collaboration et al. 2020; raw sensitivities are shown for all experiments) leading to an expectation for detection of the intensity mapping signal at redshifts approaching 8 for most models. ALMA cannot make these measurements, since its field of view is smaller than a single pixel of EoR-Spec on FYST so that it requires enormous numbers of pointings to map the large spatial scales required for these measurements. Furthermore, an interferometer is insensitive to extended low surface brightness emission and individual faint sources below its point-source detection limit, which would be recovered by the intensity mapping signal.

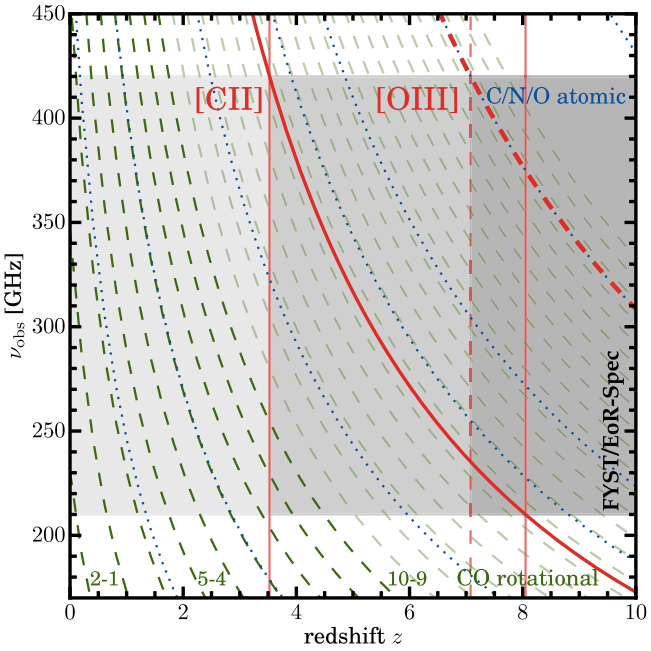

Figure 4. Lines accessible to EoR-Spec at different redshifts (gray shaded regions). Dashed green lines correspond to transitions of the CO rotational ladder, where lighter shading is used for lines that will likely be faint. All these CO lines are the foreground (Section 4.5) to the [C II] and [O III] lines (solid and dashed–dotted red lines; Section 4.1) targeted by the main experiment, but they will also provide line-intensity maps at intermediate redshifts (Section 4.2). Fainter fine-structure lines due to [C I], [O I], and [N II] are indicated as dotted blue lines.

EoR-Spec DSS intensity mapping with CO can therefore open a unique window into the molecular universe. CO lines from the $(2-1)$ transition and above fall into the EoR-Spec frequency band, with the brightest lines spanning $z \sim 0$–2. As discussed below, these lines are typically treated as foreground contaminants to the high-redshift [C II] signal (Silva et al. 2015; Sun et al. 2018), but they can also serve as an interesting science target in their own right. Dedicated CO intensity-mapping experiments exist, primarily targeting the CO(1-0) transition at $z \sim 3$ (Keating et al. 2016; Li et al. 2016), but the EoR-Spec DSS offers two distinct advantages over these surveys. First, it is sensitive to a unique redshift range, enabling continuous tomographic mapping of galaxies from cosmic noon to the present day (Madau & Dickinson 2014a). Second, the wide frequency coverage of EoR-Spec means that there are several different CO transitions accessible at each redshift. This enables the recovery of more detailed galaxy properties than can be obtained from single line observations (Kamenetzky et al. 2018).

Just as the CO transitions are a foreground to the [C II] line, care must be taken to separate out individual transitions from the full ladder of lines. This is typically done using cross-correlations, using the fact that two populations at the same redshift will trace the same large-scale structure, while interlopers at other redshifts will not be correlated (see, e.g., Switzer et al. 2019). In addition to removing contaminating emission, these cross-correlations also provide the opportunity for further science output. Spectroscopic galaxy maps are available in abundance in the EoR-Spec target fields, and correlating these surveys with our intensity maps will allow us to isolate the CO properties of specific galaxy populations (Wolz et al. 2017). This type of measurement has many uses, such as probing the interaction between active galactic nuclei (AGN) and their host galaxies (Breysse & Alexandroff 2019). One can gain additional information through internal cross-correlations within the EoR-Spec data. By matching up frequency bands corresponding to different CO lines at the same redshift, one can not only isolate specific pairs of lines but also obtain a measurement of how the intensity of one line varies with respect to another, allowing for comprehensive studies of high-redshift galaxy properties (Breysse & Rahman 2017; Sun et al. 2019; Schaan & White 2021).

4.3. Survey Strategy and Ancillary Data

To maximize the potential for cross-correlation with spectroscopy at other wavelengths, it is critical to survey the fields that have both the most sensitive observations across the broadest coverage in wavelength bands from X-ray to meter wavelengths and that have the densest spectroscopic coverage across fields that are many degrees in size on the sky (including, where possible, overlap with the best cosmological H I 21 cm surveys). The combination of data sets enables removal of foreground sources as well as the extraction of the ancillary physical properties of some of the galaxies that contribute to the LIM signal. These considerations have resulted in the choice of the E-COSMOS and E-CDFS (including the H-UDF) fields as the highest-priority survey fields for the LIM surveys with EoR-Spec. The UDS/SXDS, and Euclid South Ecliptic Pole fields and a region around 18^{h} in the HERA constant decl. strip serve as backup fields. E-COSMOS and E-CDFS will have deep $Y + Z + HK$ band coverage, including grism spectroscopy across 4.4 and 10 $\deg^2$ from Euclid, and deep–ultra-deep optical Subaru/Hyper Suprime-Cam (HSC) grizY + 4 narrow-band imaging and Prime Focus Spectrograph spectroscopy as part of the HSC strategic program and Hawaii-Two-0 (H20) surveys—both of which are essential for the selection of the highest-redshift galaxies. The Euclid deep fields are expected to lead to the identification of thousands of galaxies at $z \sim 8$. The same E-CDFS area is covered by the 6000 hr Spitzer/IRAC Spitzer Legacy Survey at 3.6 and 4.5 μm in preparation for JWST, Roman, and Euclid. The Euclid deep field has also been selected for deep imaging in the Large Millimeter Telescope (LMT)/TolTEC large-scale structure survey at 1.1, 1.4, and 2.1 mm and additional deep optical–near-infrared (O–NIR) imaging with CFHT and UKIRT. Thus, by the time of first light of FYST, the multiwavelength coverage in these fields will extend far beyond their current nominal sizes, providing the necessary ancillary data over the full anticipated EoR-Spec field sizes (4 $\deg^2$ each). The E-CDFS field also falls within the much larger HERA 21 cm constant decl. survey strip.

The EoR-Spec DSS survey will scan the full 210–420 GHz[49] frequency range at a spectral resolution of $R \sim 100$. As shown in Figure 4, this will give access to the [C II] 158 μm line at $z \sim 3.5$–8.05, to the [O III] 88 μm line at $z > 7$, and to multiple CO lines across virtually the entire redshift range (with bright transitions accessible out to $z \sim 4$–5). Coverage of the 4 $\deg^2$ fields will be achieved by scanning spatially at a specific FPI setting, then every few spatial scans, stepping the FPI, using 13 steps to cover the full redshift range in every spatial pixel every 2 to 3 minutes (see Cothard et al. 2020 for details). The E-COSMOS field will be visible at >40° elevation for 6 hr each day, while the E-CDFS field will be visible for 7.5 hr. The remaining local sidereal time range will be filled by either switching to another Prime-Cam survey or observing a field at 18^{h} in the HERA 21 cm strip, contingent on weather and instrument readiness. The highest-priority survey fields will be observed for a total of 4000 hr in 2023–28, with additional observations of the HERA 18^{h} backup *filler* field as time is available. This will result in a nominal sensitivity of 3500 Jy sr^{-1} per spectral resolution element (a 3000 km s^{-1} *bin*) in each 58″ beam of the (total) 8 $\deg^2$ field. This corresponds to a representative large-scale signal of 0.02 MJy sr^{-1} bin^{-1} at 220 GHz (i.e., [C II] at $z = 7.6$; see Table 1).

[49] Data near 325 and 375 GHz will likely be lost due to poor atmospheric transmission.

4.4. Methods to Derive Power Spectra and Cross Spectra from Raw Data

While serendipitous detection of individual [C II] sources may be possible, the central aim of intensity mapping is to statistically capture fluctuations in the integrated [C II] line intensity across the surveyed comoving volume (cf., Kovetz et al. 2017). Currently, both models and experiments are focused on a possible detection of these fluctuations not in map space but in Fourier space (in much the same way that cosmic background surveys and galaxy surveys measure and analyze angular or 3D power spectra). The main observable is the spherically averaged power spectrum $P(k)$ of the line-intensity field across the comoving volume as a function of comoving wavenumber k. Single-dish surveys like those for Prime-Cam are typically sensitive to $P(k)$ at lower values of k, corresponding to large-scale structure and clustering of line emitters.

The relative lack of information about high-redshift SF activity and its relationship to line emission both provides motivation for [C II] intensity mapping and leads to a wide range of signal forecasts (see Figure 3). All of these forecasts rely on the galaxy–halo connection (as reviewed in Wechsler & Tinker 2018)—relating SF activity per galaxy to host DM halo properties—and on a presumed conversion between star formation rates (SFR; or IR luminosities) and [C II] luminosities of galaxies. For instance, Serra et al. (2016) use a halo model for CIB anisotropies to connect halo mass to IR luminosity and a local calibration from Spinoglio et al. (2012) to relate IR luminosity to [C II] luminosity. More recently, Chung et al. (2020) combined the empirical model of Behroozi et al. (2019) with the high-redshift [C II] simulations of Lagache et al. (2018; as opposed to an observational but low-redshift result). Very recently, C. Karoumpis et al. (2021, in preparation) produced a set of alternative $P(k)$ predictions starting from a common DM cone built using the DM halo catalog from the Illustris TNG300-1 simulation (Springel et al. 2018). They applied different models of occupying the DM halos with mock galaxies as well as multiple SFR-to-$L_{[C\,II]}$ coupling relations, predicting a range of possible values of the $P(k)$ during the EoR.

The resulting forecasts for the [C II] power spectrum span at least an order of magnitude, with the Serra et al. (2016) forecasts on the more optimistic side, the Chung et al. (2020) forecasts on the more conservative side, and the C. Karoumpis et al. (2021, in preparation) forecasts spanning the range between them. However, even with these substantial uncertainties in the expected signal, we expect the fundamental sensitivity of the EoR-Spec survey (as shown in Figure 3; updated from Chung et al. 2020 based on current estimates for FYST-DSS from Table 1, as well as more recent estimates for CONCERTO based on The CONCERTO collaboration et al. 2020) to enable strong detections of [C II] emission anisotropies out to $z \sim 5$. Nondetections at $z \gtrsim 6$ are possible outcomes, but would nonetheless be valuable in constraining a model space that is currently wide open.

4.5. Foreground Rejection and Extraction of CO Signal

One of the most critical technical challenges for [C II] and [O III] intensity mapping studies is to extract the large-scale information in the presence of foreground line emission. There are two kinds of foregrounds: the continuum; and the line emission interlopers (e.g., Yue et al. 2015).

The continuum foregrounds, FIR radiation emitted from interstellar dust grains, are spectrally smooth and limited to the larger-scale Fourier modes. To avoid them, we will initially exclude this confused part of the Fourier space from our statistical analysis (e.g., Cheng et al. 2016).

The mitigation of the line emission foregrounds is more challenging. In the case of [C II] intensity mapping of the EoR, the more important interlopers are the CO transitions. Since the line foregrounds are not spectrally smooth like the continuum foregrounds, we need different approaches to remove them. Several of the proposed techniques focus only on the extraction of the two-point statistics (power spectrum or correlation function), whereas others attempt to reconstruct the individual line maps. Some examples of the proposed methods are as follows:

1. One approach is masking out the brightest velocity pixels (voxels) in the survey. The CO line emission comes from galaxies of lower redshift than the [C II] emission. These galaxies tend to be more massive and thus brighter. As a result, the brightest voxels have a higher probability of containing CO line emitters, and by simply masking them, we can decrease the foreground emission (e.g., Breysse et al. 2015).
2. Another way to mask the line emission foregrounds is with the help of ancillary data. Using galaxy catalogs with accurate redshift information and proxies for the CO line emission of the interloping galaxies, we can identify the voxels containing the more luminous CO lines emitters and mask them (e.g., Yue et al. 2015; Sun et al. 2018).
3. Cheng et al. (2020) use the fact that multiple CO lines that are emitted by a source are observable in an LIM survey. They demonstrate that the redshift of a source can be derived by fitting to a set of spectral templates that are unique at each redshift. In this way, individual line maps can be retrieved without using any external tracers or spectroscopic follow-up observations.
4. An alternative technique is based on projecting the LIM data cube from the intrinsic observing angular and spectral coordinates to the comoving coordinate frame of the targeted [C II] emission. Because in this projection, we assume a redshift for the target; the interloper emission fluctuations are mapped to the wrong spatial scales. This makes the interloper emission highly anisotropic. Cheng et al. (2016) show that this anisotropy can be used to fit out the interloper contamination.
5. Moriwaki et al. (2020) demonstrate that deep learning networks, after being appropriately trained with a large set of mock observations, can generate accurately the intensity distribution of the targeted line.
6. Finally, in the frequency range covered by the EoR surveys, there are sets of frequency channels that contain emission from two or more adjacent CO lines, originating from the same redshift. When cross-correlating these channels, since only the two lines emitted from the same redshift will be correlated, we just measure the CO foreground, which we can then remove (e.g., Sun et al. 2018).

As described in Section 4.3, our high-priority fields will have a broad frequency coverage. This includes both the spectroscopic redshift of the foreground galaxies and indirect tracers of their CO emission, making it possible to mask the voxels that contain them. Using these well-covered fields, we will be able to verify and improve the techniques that do not require external tracers, and adapt them for future use. The EoR-Spec DSS survey strategy thus is optimized for foreground removal to maximize recovery of the main survey signal.

5. Tracing Galaxy Evolution from the First Billion Years to Cosmic Noon

Much of SF is hidden from view in the optical bands due to dust in the molecular clouds that envelops the newly formed stars. This dust absorbs the starlight, heats up, and reradiates the power at FIR wavelengths. This dust-enshrouded SF is important over cosmic time— the cosmic optical background power and CIB energy density are roughly equal (e.g., Dole et al. 2006; Burgarella et al. 2013). Consequently, when considering the SF history of the universe, both optical and FIR wavelengths must be considered. A discrepancy in the expected infrared output, inferred from the dust masses in local galaxies, and the observed measurements of the CIB suggested first that IR sources must become more numerous at higher redshift and be a critical component of early mass buildup (e.g., Lagache et al. 2005), which was further supported by studies of the most luminous "submillimeter galaxies" (e.g., Casey et al. 2014). Subsequent Spitzer and Herschel surveys resolved ∼80% of the CIB at $\lambda < 160$ μm ($\nu > 1.9$ THz) into individual galaxies. This work provided robust constraints on the cosmic SF history at $z \lesssim 1.5$ and demonstrated that about 70% was dust-enshrouded at these epochs (Magnelli et al. 2013). However, the dust emission from higher-redshift galaxies is redshifted to a longer wavelength (>250 μm or $\nu < 1.2$ THz) where the inability of the 3.5 m Herschel telescope to separate emission from multiple galaxies within a single spatial beam (source confusion) becomes a serious problem. Therefore, at $z \gtrsim 1.5$, the fraction of CIB resolved into individual galaxies drops to only ∼10% (Béthermin et al. 2012). Such limitation is unfortunate and critical, as in this wavelength range, the CIB is dominated by $z \gtrsim 1.5$ galaxies (Béthermin et al. 2012) while providing the best dust-obscured SFR proxy for this galaxy population (Figure 5 lower right). Thus, to study the source of the CIB at $\lambda > 160$ μm in detail (understanding the physical properties of high-redshift galaxies contributing to the CIB), high-resolution IR surveys such as those done with Prime-Cam on FYST need to be conducted.

Prime-Cam on FYST provides the instrumentation and platform to enable studies of DSFGs at redshifts from 1 to 5 and beyond. With the 6 m aperture of FYST, Prime-Cam reaches about 3 times deeper into the source confusion than was possible with the Herschel 3.5 m telescope, resulting in a difference in luminosity limit of a factor of ≈2–3, depending on which Herschel-SPIRE bands are considered (see Figure 5). Using the model of Béthermin et al. (2017), we predict that confusion-limited Prime-Cam surveys (DSS and CIB-Mid) will

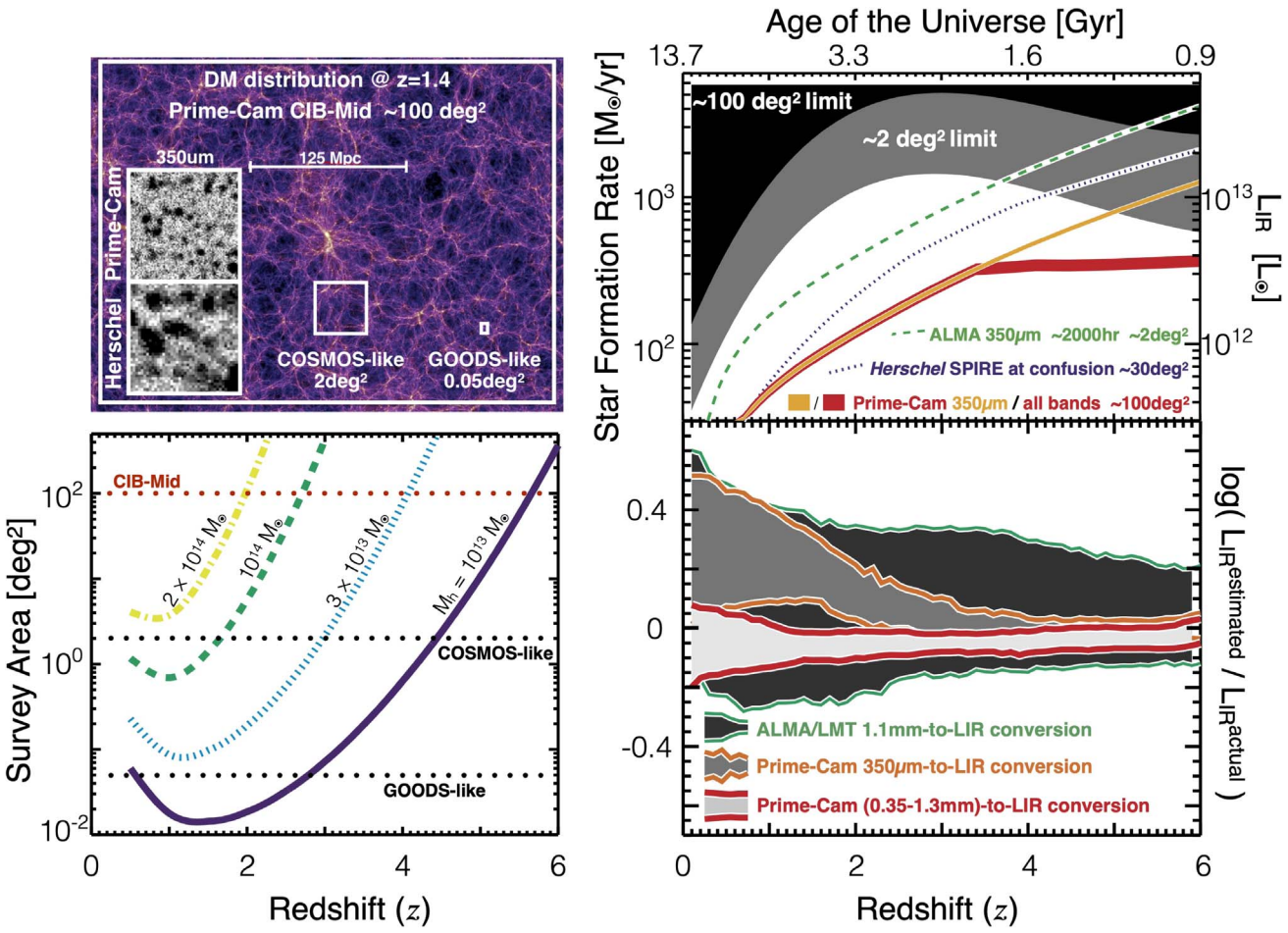

Figure 5. Contiguous wide-area multiwavelength Prime-Cam surveys will measure the dust-obscured star formation properties of hundreds of thousands of galaxies out to $z \sim 6$ with high precision. This will greatly enhance our picture of cosmic galaxy evolution, probing 2–3 times lower luminosities than Herschel-SPIRE at $z > 1$ (due to source confusion; see insets in upper left panel) while sampling large-scale environments (voids, average density regions, groups, and clusters) over 100 times larger areas than feasible to map with ALMA (the field of view of ALMA is a fraction of a single Prime-Cam pixel) and providing more accurate dust-obscured star formation measurements than current or future millimeter-only surveys. Upper left: sky coverage of the CIB-Mid survey (i.e., $\sim$100 deg^2) compared to the dark matter distribution at $z \sim 1.4$ from the Millennium simulation (Springel et al. 2018). Insets illustrate how the improved angular resolution of Prime-Cam helps going deeper into the source confusion than was possible with the Herschel 3.5 m telescope. Lower left: survey area needed to detect at least one halo of mass, $M_{\rm h}$, at a redshift, z, within a redshift bin, $\Delta z = 0.1 \times z$, as inferred using the halo mass function of Murray et al. (2013). Different lines correspond to different halo masses. This plot only includes structures that will likely be within our field of view, not which ones would be detectable, as that depends on the occupation of these structures by DSFGs. These structure will by identified by other means (e.g., X-ray, optical) and studied by Prime-Cam through either direct detection or stacking analysis. Upper right: simulated Prime-Cam survey luminosity limits, compared to surveys feasible with existing instrumentation covering the 250–500 μm wavelength range, which is critical to measure accurately the infrared luminosity of $1 \lesssim z \lesssim 6$ galaxies. Prime-Cam will probe up to 2–3 times deeper than Herschel-SPIRE, while sampling luminosities inaccessible to small (e.g., ALMA) surveys because of the rarity of luminous objects. These limits are illustrated by the gray and black areas, i.e., there will be less than 10 galaxies more luminous than these limits within a redshift bin, $\Delta z = \max(0.15 \times z, 0.5)$ in a survey of 2 or 100 deg^2, as inferred using the model of Béthermin et al. (2017). Lower right: predicted reliability (16th to 84th percentiles) of FIR luminosity measurements, highlighting the vast improvements with the short submillimeter-wavelength Prime-Cam 350 μm (850 GHz) band and wide spectral coverage. These reliabilities were inferred by fitting (or renormalizing) single modified blackbody function with $\beta = 1.5$ and $T_{\rm dust} \in$ [20–50 K] (e.g., Magnelli et al. 2012) to the variety of SEDs from the Draine & Li (2007) template library. See text for detailed description of this procedure. At all redshifts, we use the same set of SEDs—we assume no redshift evolution in $L_{\rm IR}$. Errors improve at higher redshift because we probe closer to the SED peak, and thus any dust temperature dependency becomes less problematic (see also Figure 9 of Schreiber et al. 2015).

securely detect hundreds of thousands of galaxies, with a small fraction of these (<0.5%) at redshifts potentially as high as 6 (Figure 5, upper right) and resolve into individual galaxies up to ~40% of the CIB at 850 GHz. Specifically we estimate 440,000 individual galaxies above a signal-to-noise ratio of 5 within each of our confusion-limited $\sim$ 100 deg^2 surveys (e.g., CIB-Mid), 1300 of which we expect to be at $z > 5$ and detected primarily by the lower-frequency Prime-Cam modules (220–410 GHz). Compared with Herschel at 350 μm ($\sim$850 GHz), this represents $\approx 10 \times$ the number of sources per square degree detected above the confusion limit.

5.1. Dusty Star-forming Galaxy Surveys

In its early pilot phases, our DSFG survey will cover the rich, multiwavelength GAMA fields ($\sim$100 deg^2 total) to the confusion limit at 850 GHz (Figure 5, upper left inset), making use of the best quartile in precipitable water vapor (PWV). Ultra-deep integrations covering 4–16 deg^2 over key galaxy evolution survey fields (COSMOS and E-CDFS) will also be obtained, in parallel alongside the EoR intensity mapping fields, and will reach far below the confusion limit, providing a precise measurement of the confusion noise on the scales most relevant to Prime-Cam. The full survey will also cover

the $\sim$100 deg^2 extended SDSS Stripe-82 area (previously covered only shallowly by Herschel-SPIRE) to comparable depths.

Its deep, yet wide-field (100 deg^2; e.g., CIB-mid) survey will sample environments on large scales that cannot be mapped with ALMA, and reach down to luminosities that remained inaccessible to Herschel (Figure 5, upper right). The 850 GHz band is critical to extract the infrared luminosities and subsequently the dust-obscured SFRs to far greater precision than possible with long-wavelength surveys (e.g., LMT; Figure 5, lower right) alone. For example, the first followup of 350 GHz-selected galaxies with Herschel-SPIRE at these high frequencies constrained the peak of their dust spectral energy distributions (SEDs) and allowed their dust temperatures and FIR luminosities to be measured for the first time, enabling accurate SFR constraints (Chapman et al. 2010; Magnelli et al. 2012). Today, measuring the peak of the dust SEDs is a prerequisite to precision constraints on dusty and highly star-forming galaxies at $1 \gtrsim z \gtrsim 6$, and puts them in context with the cosmic history of SF (Elbaz et al. 2018).

In summary, the large and comprehensive sample of DSFGs that will result from Prime-Cam galaxy evolution survey will (1) lead to robust constraints on the luminosities of bright submillimeter sources from $z = 1$ out to $z > 5$; (2) statistically constrain the cosmic SF history out to $z \sim 5$; (3) study the impact of environment on the population of high-luminosity DSFGs (SFR $\gtrsim 200\,M_\odot\,\mathrm{yr}^{-1}$) galaxies; (4) reveal their evolutionary link to today's ellipticals; and (5) allow for the study of *exotic* sources, such as protoclusters and strongly lensed sources, extending luminosity limits downwards by 2–3 times of those that were achieved by Herschel at high ($z > 3$) redshifts. We describe these predicted science results in more detail below.

5.2. Cosmic History of Star Formation

The science legacy of these Prime-Cam surveys will be rich with a better understanding of the cosmic history of SF. The cosmic history of SF, galaxy assembly, and matter content are encoded in the variation of the physical properties of galaxies with their spatial and redshift distributions (Madau & Dickinson 2014b). In order to properly trace and understand the formation and evolution of galaxies, large statistical studies are required over representative cosmic volumes that adequately sample the entire range of cosmic environments (>100 deg^2; Figure 5 upper and lower left), and map the (unknown) large-scale structure at redshifts 2 to 4. Over the next decade, short-wavelength surveys will be carried out to commensurate depths and areas at X-ray to near-infrared wavelengths (e.g., eROSITA, Rubin, Dark Energy Survey (DES), Euclid, and Roman) tracing unobscured SF. Combining our surveys with synergistic work in the O–NIR (DES, Rubin, Euclid, and Roman) Prime-Cam will help identify key parameters that regulate SF (such as environment, AGN, and matter content) in high-luminosity DSFGs (SFR $\gtrsim$ $200\,M_\odot\,\mathrm{yr}^{-1}$; Figure 5 upper right) over cosmic time. Such constraints are paramount to shed light on the formation of local massive ellipticals, likely produced from gas-rich mergers at high redshift that trigger violent and short-lived SF activities (Hopkins et al. 2006; Faber et al. 2007).

However, the dust-obscured half of SF is only robustly accessible at rest-frame FIR wavelengths, which are redshifted into the 250–500 μm wavelength range (1200–600 GHz) where no commensurate survey capabilities exist yet. Since the properties of dust in galaxies appear to evolve significantly with cosmic time (Casey et al. 2014), short-wavelength surveys (rest-frame UV and optical) have to rely on order-of-magnitude extinction corrections that are too large for measuring reliable SF properties. Without accurate measurements of FIR luminosities, the total (i.e., direct + obscured stellar light) SFRs and SF properties in galaxy evolution studies therefore remains out of reach. Herschel has certainly pushed our understanding considerably here. Thanks to its increased depth and wide coverage, Prime-Cam surveys will further our understanding of rest–UV-selected populations, statistically constrained through stacking the mean dust-obscured SFRs of galaxy populations not directly detected but selected from large O–NIR surveys. Using this approach, it will be possible to estimate the *total* SF activities of "normal" (i.e., L^*) galaxies out to $z \sim 5$ (galaxies that have $L_{\rm IR}^{L_*} \sim 0.1 \times L_{\rm IR}^{\text{Prime-Cam limit}}$ at $z \sim 1$–5; Gruppioni et al. 2013; Magnelli et al. 2013; Gruppioni et al. 2020), and provide improvements in a robust determination of the cosmic SF history.

We note that the $z > 5$ FIR luminosity function is still highly uncertain (Casey et al. 2018), and a factor of ≈ 2 uncertainty exists on the number of $z > 5$ sources that will be found in these surveys. Figure 5 illustrates these model surveys and luminosity limits. The model includes those galaxies detected at a given band, so indeed the highest-redshift galaxies constrained at 850 GHz alone need to be detected at this frequency and therefore have larger SFRs ($>1000\,M_\odot\mathrm{yr}^{-1}$) as shown in the upper left panel. Including all the Prime-Cam bands, there is a much larger number of galaxies extending to lower luminosities, and the majority of these anticipated $z > 5$ galaxies will be undetected dropouts at 850 GHz. At $1 < z < 6$, the 850 GHz band of Prime-Cam will probe the FIR emission of galaxies near the rest frame of the dust emission SED peak, thereby providing an excellent proxy for estimating FIR luminosities and dust-obscured SFRs in the high-redshift universe. This can be accomplished with typically 2–3 times more accuracy than is possible with, for example, LMT/ALMA millimeter-wave surveys alone, and 3–5 times more accurately for galaxies also detected by Prime-Cam lower-frequency (down to 220 GHz) bands (5%–8% according to the model of Béthermin et al. 2017; Figure 5, lower right). Our procedure for estimating these curves in Figure 5 is as follows. We take a subset of realistic Draine & Li (2007) SED templates, limiting to MW-type PAHs, fixing radiation fields U to $U_{\rm max} = 1 \times 10^6$, and $0.7 < U_{\rm min} < 25$ (see Magnelli et al. 2012), corresponding to 2700 templates. We renormalized all these templates to $L_{\rm IR} = 1\ L_\odot$, and then for each redshift, we calculate their observed flux densities. For the 270 GHz (1.1 mm)-to-$L_{\rm IR}$ conversion, we renormalized to the observed 270 GHz flux density of each template and look at the entire distribution in $L_{\rm IR}/(1\,L_\odot)$. We do the same for the 850 GHz-to-$L_{\rm IR}$ conversion. Finally, for the 860 to 230 GHz (0.35–1.3 mm)-to-$L_{\rm IR}$ conversion, we fitted the flux densities (850, 410, 350, 280, 220 GHz) of each template with single gray-bodies, and again look at the distribution in $L_{\rm IR}/(1\ L_\odot)$. While Prime-Cam does not provide a unique ability to make such measurements (for instance, LMT 270 GHz; 1.1 mm), detections could be followed up one by one with ALMA at 850 GHz; it does facilitate such measurements efficiently over an unprecedented large numbers of galaxies. Prime-Cam therefore fills a critical gap with its unique combination

of deep 850 GHz coverage, significantly improved spatial resolution ($\sim$15″ at 850 GHz) compared to previous facilities operating at these frequencies (in particular Herschel, Lutz 2014), and a very large field of view (0.78 deg^2; > 200,000 times larger than ALMA at 850 GHz). Through deep, large-area contiguous submillimeter-wave surveys (critically complementing ultra-deep "pencil beam" surveys with ALMA; Aravena et al. 2016; Walter et al. 2016; Dunlop et al. 2017; Franco et al. 2018; González-López et al. 2019), Prime-Cam surveys will in its lifetime securely detect millions of star-forming galaxies via many 100 deg^2, confusion-limited fields across a broad range of cosmic environments out to $z \sim 5$, probing typically about 3 times deeper than the most sensitive Herschel surveys (Lutz 2014).

From direct observations of the FIR spectral energy distribution peak, accurate dust-obscured SFRs, can be inferred for the vast majority of high-luminosity DSFGs (SFR $\sim$ hundreds of $M_\odot$ yr^{-1}) galaxies out to $z \sim 5$ within the wide-field O–NIR survey fields that will become available at first light for FYST. For about 5%–10% of these galaxies, detection in several Prime-Cam lower-frequency (down to 220 GHz) bands will be also available, which will yield accurate dust masses and temperatures. Additional physical parameters of these massive and intensely star-forming systems may be determined for a subset of the sample by combining Prime-Cam surveys with these synergistic O–NIR surveys to obtain their photometric redshifts, stellar masses, and unobscured fractions of the SFR, which is $\leqslant$50% globally (Burgarella et al. 2013; Pannella et al. 2015; Gruppioni et al. 2020). The ability to obtain photometric redshifts from O/IR surveys will however depend on redshift and obscuration (Chapman et al. 2003, 2005; Casey et al. 2012; Danielson et al. 2017). FIR-based photometric redshifts will need to be used for a substantial fraction of the sources, especially at higher redshifts, with the caveat made in these references that these methods have errors of $dz \sim 0.5$. In these cases, the $L_{\rm IR}$ and $M_{\rm dust}$ estimates can be made, but M^* and unobscured SFR fraction will not be accessible. We note that cross identification with O/IR-selected galaxies is not trivial or in some cases even unique. However, so-called *super-deblending* studies have made significant progress in this regard for Herschel observations (Jin et al. 2018; Liu et al. 2018), and Prime-Cam will help further these studies. We estimate the fraction of Prime-Cam detections that will have an O/IR counterpart using the model of Schreiber et al. (2017), which includes both O/IR and FIR. First, we used this model to predict the number of Prime-Cam detections (above confusion) in our 100 deg^2 field and found very consistent numbers with Béthermin et al. (2017). Then, we assumed that our 100 deg^2 field will be covered by the Euclid 15,000 deg^2 wide survey and thus will have a (g, r, i, z) coverage from the ground down to AB $\sim$ 24 and (Y, J, H)-coverage from Euclid down to AB $\sim$ 24. The final model predicts that about 68% of our Prime-Cam survey will have a counterpart in one of the (g, r, i, z) images and 36% in all (g, r, i, z) images; 96% will have a counterpart in one of the (Y, J, H) images and 85% in all (Y, J, H) images; 96% will have detection in one of the (g, r, i, z, Y, J, H) images and 36% in all (g, r, i, z, Y, J, H) images. Therefore, the rest-frame-UV images will be biased against highly obscured SFGs, but observed frame optical–NIR images will provide counterparts for most of the Prime-Cam sources.

From this, it is then possible to statistically identify the key parameters regulating matter assembly (cosmic epoch verses environment) in these extreme systems, which are likely the progenitors of local massive ellipticals. Prime-Cam wide-area surveys will be particularly advantageous in this context as they will allow for accurate measurement of the clustering properties of these extreme systems and thereby test their evolutionary link to today's massive ellipticals, which are known to reside in the central region of massive groups and clusters. Through stacking of hundreds of galaxies, Prime-Cam will also statistically constrain the mean dust-obscured SFRs of galaxy population not directly detected but selected from large O–NIR surveys ($S/N^{\rm stack} \propto S/N^{\rm ind.} \times \sqrt{N_{\rm stack}}$). From this, it is then possible to obtain a significantly improved determination of the cosmic SF history.

Because of the large survey areas, it will also be possible to discover large samples of strongly lensed dusty galaxies for detailed follow-up studies with ALMA and JWST (e.g., Cañameras et al. 2015; Hodge & da Cunha 2020) and IR-bright galaxy protoclusters at high redshift as signposts of early structure formation (Miller et al. 2018; Oteo et al. 2018; Gómez-Guijarro et al. 2019; Hill et al. 2020). Prime-Cam surveys will also be suitable to uncover very dusty sources (including the most intense starbursts in the universe) that are entirely missed by even the deepest O–NIR surveys, over a broad luminosity range; out to $z > 7$ (e.g., Riechers et al. 2013; Strandet et al. 2016; Brisbin et al. 2017; Riechers et al. 2017; Marrone et al. 2018; Wang et al. 2019; Reuter et al. 2020). These sources are very rare, and only very small numbers are currently known at $z > 5$, due to the limited sensitivity, wavelength coverage, and/or areas of past and current (sub) millimeter surveys (see Riechers et al. 2020, for a recent overview). While such sources are bright in millimeter-wave surveys, they can be discriminated from the dominant lower-redshift foreground with the inclusion of the shorter sub-millimeter-wave band of Prime-Cam (Riechers et al. 2017). As illustrated in Figure 5 (upper right), applying such a 850 GHz *dropout* technique will indeed be a powerful tool to select $z > 4$ candidates. While Herschel has made significant progress in studying submillimeter-wave dropouts and 500 μm (600 GHz) risers (e.g., Donevski et al. 2018; Lewis et al. 2018), the additional depth afforded by the smaller beam size of Prime-Cam will lead to both more stringent selection criteria and fainter sources being selected at these high redshifts.

By obtaining good statistics on this population of dusty, highly star-forming galaxies at higher redshifts than those probed by Herschel, one can address important issues of galaxy evolution. For example, when and how did local *red-and-dead* ellipticals form? Two leading theories that link the evolutionary tracks are through major mergers, which trigger intense, yet short-lived starbursts leaving behind a passively evolving elliptical, and massive star-forming galaxies that are starved of gas by a *too-hot* halo. Overall, in the Prime-Cam galaxy evolution survey, through the detection of large samples of dusty, highly star-forming galaxies over a broad range of redshifts, the mechanism of evolution into local ellipticals can be studied in more statistical detail.

6. Measuring CMB Foregrounds to Aid the Search for Primordial Gravitational Waves

In recent years, enormous progress has been made using CMB temperature and polarization measurements to constrain

cosmological parameters and characterize the large-scale structure of the universe (Komatsu et al. 2014; Keck Array & BICEP2 Collaborations 2018; Choi et al. 2020b; Adachi et al. 2020; Aiola et al. 2020; Planck Collaboration VI 2020; Dutcher et al. 2021). In addition to upcoming projects such as SO (Simons Observatory Collaboration 2019) and BICEP Array (Keck Array & BICEP2 Collaborations 2018), the CMB research community is developing plans for the next generation of ground-based CMB-S4 (Abazajian et al. 2019) and for the LiteBIRD space mission (Hazumi et al. 2019, 2020). These facilities promise to achieve dramatic improvements in constraints on the amplitude of the primordial gravitational waves (Grishchuk 1975; Starobinsky 1979), which are imprinted on the CMB "*B*-mode" polarization (Kamionkowski et al. 1997a; Seljak & Zaldarriaga 1997), and on the effective number of light relic species (Bashinsky & Seljak 2004; Hou et al. 2013).

FYST is a potential telescope platform for CMB-S4, and it also offers unique capabilities for important advances in high-frequency polarization science before CMB-S4. Prime-Cam on FYST will help address fundamental questions about the origins of the universe by testing theories of early conditions through improved constraints on primordial gravitational waves (or tensor perturbations). Scalar perturbations cause energy density fluctuations at the surface of last scattering that only generate the even-parity *E*-mode polarization (Kamionkowski et al. 1997b; Zaldarriaga & Seljak 1997), which has been well characterized (Komatsu et al. 2014; Keck Array & BICEP2 Collaborations 2018; Adachi et al. 2020; Aiola et al. 2020; Planck Collaboration VI 2020; Dutcher et al. 2021). Inflation models predict a period of rapid expansion in the early universe (Guth 1981; Sato 1981; Albrecht & Steinhardt 1982; Linde 1982), and the generation of both scalar (Mukhanov & Chibisov 1981; Guth & Pi 1982; Hawking 1982; Starobinsky 1982; Bardeen et al. 1983) and tensor perturbations (Grishchuk 1975; Starobinsky 1979), the latter of which would leave odd-parity *B*-mode imprints in the CMB polarization (Kamionkowski et al. 1997a; Seljak & Zaldarriaga 1997). Measuring the primordial *B*-mode polarization to constrain the amplitude of tensor perturbations and hence the tensor-to-scalar ratio r will test many inflationary and other early universe theories (see Kamionkowski & Kovetz 2016, for a review). In Section 6.1, we describe Prime-Cam measurements in the context of current and upcoming CMB experiments, and in Section 6.2, we present forecasts for improving constraints on r with the addition of Prime-Cam data.

6.1. Prime-Cam in the Context of Current and Upcoming CMB Experiments

The current best constraint on the primordial *B*-mode signal is $r < 0.07$ (95% confidence level, CL, from Keck Array & BICEP2 Collaborations 2018), which improves to $r < 0.044$ when using all the CMB temperature and polarization data (from Planck; Tristram et al. 2021). This is limited by the uncertainty on the polarized Galactic dust emission. Several experiments that are planned or under construction aim to better constrain r from more precise measurements of both the CMB and the Galactic dust through observations in multiple frequency channels (Abazajian et al. 2019; Simons Observatory Collaboration 2019; Hazumi et al. 2019; Schillaci et al. 2020). In particular, SO aims to achieve $\sigma(r) = 0.003$ with multiple small aperture telescopes (SATs) and a large aperture telescope (LAT) like FYST observing at six frequencies between 27 and 280 GHz.

Prime-Cam will make the most sensitive measurements at frequencies >300 GHz of polarized dust foregrounds yet, with the WFS improving on the current state-of-the-art Planck 353 GHz map by a factor of >2 over more than half the sky (also see Section 7). We illustrate here the value of Prime-Cam high-frequency observations for constraining the polarized dust emission and mitigating potential bias on r from SO. At the current sensitivities, the polarized dust emission is well described by a single-temperature modified blackbody model, $D_\nu(\beta_d, T_d) \propto \nu^{\beta_d - 2} B_\nu(T_d)$ (in Rayleigh–Jeans temperature units), where β_d is the dust spectral index, T_d is the dust temperature, and B_ν is the Planck function (Planck Collaboration XI 2020). Prime-Cam will play a major role in constraining of β_d and T_d, thereby improving the constraint on r achievable by SO (and other experiments with overlapping fields).

6.2. Methods: Improving Constraints on r and Galactic Dust

The possible improvement from Prime-Cam on the constraint on r beyond the SO-SATs is analyzed as follows.[50] We first simulate realistic foreground sky maps at Prime-Cam and SO frequencies using the `PySM` simulation package (Thorne et al. 2017). We then add Gaussian simulations of CMB (without the primordial *B*-mode but with the scalar *E*-mode and the lensing-induced *B*-mode) and noise (including white and $1/f$ components extrapolated from on-sky measurements; see Simons Observatory Collaboration 2019; Choi et al. 2020b) modulated by the realistic survey hit-count maps of SO-SAT and FYST, and compute the autofrequency and cross-frequency power spectra of all the simulated maps using the `NaMaster` package (Alonso et al. 2019)[51] with the "purify B" option and the "C2" apodization scheme (10°). We use the maximum likelihood method (Stompor et al. 2009) for finding the best-fitting values of β_d, T_d, and β_s (the spectral index for the synchrotron emission). In the fitting, we assume that these parameters are homogeneous over the sky patch observed by SO-SAT, although the simulation does contain spatially varying foreground parameters. We impose Gaussian priors of $\beta_d = 1.6 \pm 0.5$, $\beta_s = -3.0 \pm 0.5$, and $T_d = 19.6 \pm 5$ K. Finally, we deproject the best-fitting synchrotron and dust emission using the constrained internal linear combination (cILC) method (Remazeilles et al. 2011c, 2011; Hurier et al. 2013), estimate the foreground-cleaned *B*-mode polarization power spectrum, and calculate the tensor-to-scalar ratio r from the multipole range of $30 < \ell < 260$. Since the cILC is a blind method, we can further reduce the residual foreground contamination that is not modeled by the parametric method; thus, our approach is a hybrid of the parametric maximum likelihood method and the cILC. We repeat this procedure for 1500 realizations of CMB and noise and calculate the mean and standard deviation of r.

In Figure 6, we show the distributions of the dust parameters, β_d and T_d. The SO-SAT-only results show a strong degeneracy between the two parameters; thus, the constraints are dominated by the prior. This degeneracy is

[50] The Julia codes and documentation for this analysis are available at https://github.com/komatsu5147/CleanCMB.jl.
[51] https://github.com/LSSTDESC/NaMaster

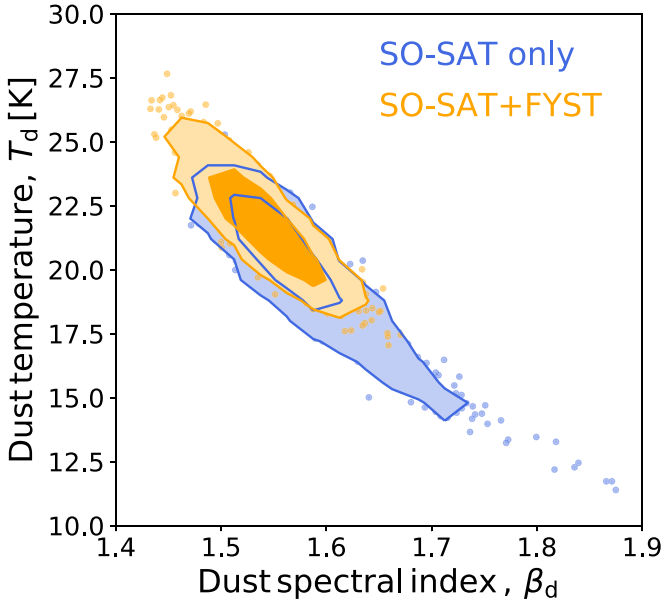

Figure 6. Distributions of the best-fitting values of the dust parameters, β_d and T_d, from 1500 realizations of the simulation with SO-SAT only (blue) and SO-SAT + FYST with Prime-Cam (orange). Shaded contours show the approximate 1σ and 2σ intervals, while the dots represent the simulation results outside of the 95% confidence range. This shows a significant reduction of the degeneracy when combining the two data sets.

reduced substantially by adding the data of FYST with Prime-Cam. We note that Prime-Cam's highest-frequency channel, 850 GHz, is crucial for reducing the degeneracy of the two parameters.

For r, SO finds a bias due to the residual dust foreground emission that is on the order of the statistical uncertainty (Simons Observatory Collaboration 2019). This bias can be reduced by marginalizing over the foreground model parameters; however, as mentioned in Simons Observatory Collaboration (2019), this reduction (1) comes at the expense of increased $\sigma(r)$ by about 70%; and more importantly, (2) is possible only with simulations where the actual foreground residual is known. By combining the Prime-Cam high-frequency data with SO, we find that $r = (0.2 \pm 2.7) \times 10^{-3}$ is achievable. Comparing this to $r = (1.3 \pm 2.8) \times 10^{-3}$, which we obtained for the SO-SAT-alone case with their "pess-1/f" noise in the baseline design (Simons Observatory Collaboration 2019) and without marginalization over the residual foreground, we find that the combination with Prime-Cam can reduce the foreground residual bias by a factor of more than 6 while maintaining a similar level of $\sigma(r)$ (Figure 7). The 95% CL upper limits thus improve from $r < 6.8 \times 10^{-3}$ to $r < 5.5 \times 10^{-3}$. Even if we remove the Prime-Cam data at low multipoles ($\ell < 60$), we still find a significant reduction in the bias, $r = (0.5 \pm 2.8) \times 10^{-3}$. In other words, Prime-Cam measurements have the potential to aid the search for primordial gravitational waves in a significant manner.

Our results do not rely on one specific frequency channel. We find that each of the 350, 410, and 850 GHz data contribute approximately equally to the reduction of bias in r. While the degeneracy between the dust parameters is reduced largely by the 850 GHz data, the other frequency channels help reduce the bias via the cILC step, which highlights the value of having measurements at multiple submillimeter frequencies. In summary, Prime-Cam measurements of Galactic dust combined with SO-SAT measurements are predicted to reduce bias and improve constraints on the primordial gravitational waves.

7. Galactic Polarization Science: Magnetic Fields and Dust Properties

Interstellar dust represents most of the solid material in our universe. Despite this importance, many questions remain about its composition and structure (Hensley & Draine 2021). Thermal dust emission is a multipurpose tool in the study of clouds and SF. It is commonly used as a density tracer to obtain the total mass and gravity of gas-dominated systems (e.g., Stutz & Kainulainen 2015; Sadavoy et al. 2016; Stutz & Gould 2016). Polarized dust emission is used to map magnetic fields in all phases of the ISM (Planck Collaboration Int. XIX 2015; Fissel et al. 2016; Tahani et al. 2018; Pattle & Fissel 2019; Sadavoy et al. 2019; Tahani et al. 2019). Nonspherical dust grains in the ISM align with the magnetic field (Andersson et al. 2015; Reissl et al. 2018, 2021). Hence, thermal dust emission is imprinted with a linear polarization signal. This polarization signal traces the plane-of-the-sky magnetic field geometry, while the degree of polarization depends on the properties of the dust grains (Hildebrand 1988; Draine & Fraisse 2009; Draine & Hensley 2020), as well as the 3D geometry of the magnetic field (Chen et al. 2019). Prime-Cam observations will measure polarized dust emission in resolved systems in both the Galaxy and the LMC over wide fields, accessing a broad range of scales. These data will enable tests of dust models, probe the properties of interstellar turbulence, and investigate the effects of the magnetic field on cloud, star, and cluster formation in both high- and low-mass star-forming regions.

In this section, we describe our survey design. The survey is driven by the requirement for Prime-Cam dust polarization observations of both diffuse regions and denser molecular clouds. Of the latter, it covers a relevant range of cloud masses. Our planned surveys have two main components: (1) the 4000 hr WFS, which is comparatively shallow but will cover more than half of the Galactic plane and will provide $< 1'$ resolution maps of higher-mass molecular clouds (see Figure 8); and (2) targeted deeper wide-field mapping observations of individual systems. Specifically, Prime-Cam will make deep dust polarization maps of seven nearby molecular clouds, the nearby translucent ($N_H \sim 10^{21}$ cm^{-2}) cloud Pyxis, and the LMC; Table 3 lists the polarization survey targets. With both high sensitivity and resolution that is $\gtrsim$20$\times$ that of the Planck satellite, Prime-Cam will be the first polarimeter able to continuously trace polarized dust emission with high fidelity from entire cloud scales down to the scales where individual stars and their planetary systems form.

Many of our target regions will also be observed by CHAI in the submillimeter [C I] fine-structure and the CO(4-3)/CO(7-6) CO rotational lines or will be covered by other Galactic spectral surveys, providing complementary surveys of turbulence and gas kinematics. With our Prime-Cam surveys and this ancillary data, we will study the magnetohydrodynamic (MHD) turbulent power spectrum, dust properties, and magnetic field properties across a range of ISM phases, cloud environments, clouds masses, and inferred evolutionary stages. Hence our survey design enables the evaluation of the role of various fundamental physical processes as a function of both mass and time (Stutz & Gould 2016). Prime-Cam will map dust emission

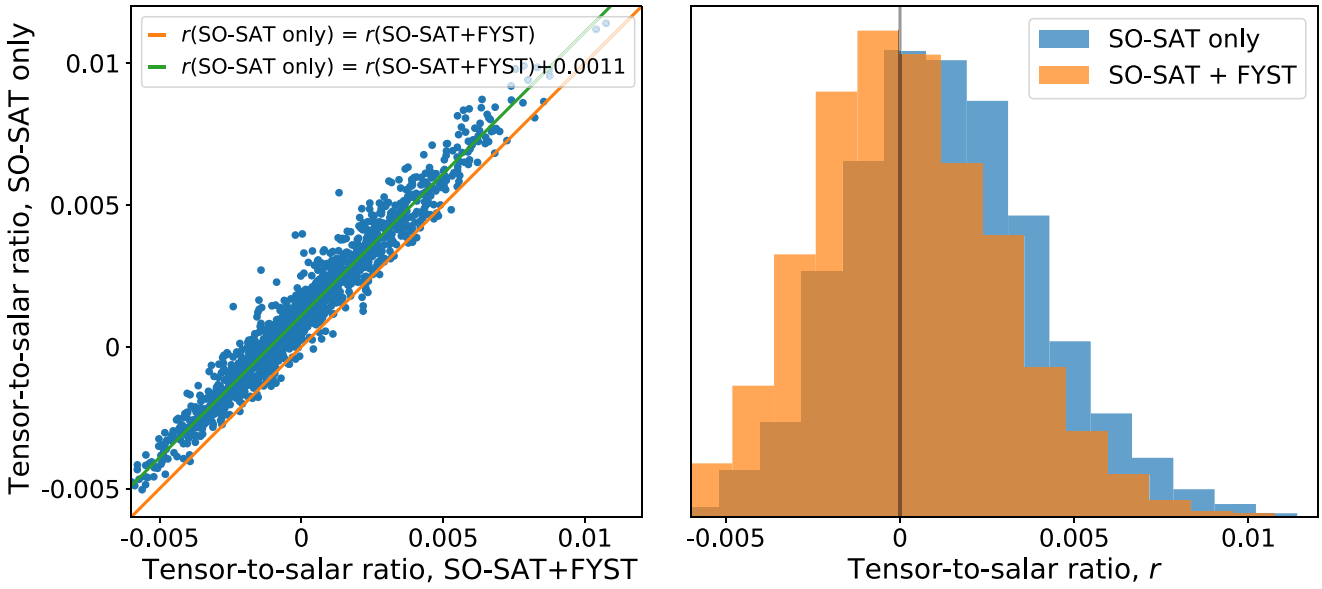

Figure 7. (Left) Scatter plot of the distributions of the best-fitting values of r, showing that the SO-SAT only results have a systematic bias at the level of $\delta r = 1.1 \times 10^{-3}$ (green line) compared to the SO-SAT + FYST results. The orange line shows the case with no bias. (Right) Histograms of r constraints from 1500 realizations of the simulation with SO-SAT only (blue) and SO-SAT + FYST with Prime-Cam (orange), showing a significant reduction of the bias on r when combining the two data sets. Note that the simulation does not have the primordial B-mode signal, i.e., $r_{\rm input} = 0$ (vertical line).

and polarization in hundreds of molecular clouds in both the MW and the LMC, forming a large basis set for launching new investigations into interstellar dust and the role of turbulence and magnetic fields in the formation of stars and clusters from the gas phase.

In the following, Section 7.1 describes how Prime-Cam polarization data constrains dust grain models, Section 7.2 describes how Prime-Cam polarization addresses the physics of the diffuse ISM, Section 7.3 describes a multiscale survey of magnetic fields in the LMC, and Section 7.4 describes the roles of magnetic fields in SF outcomes.

7.1. Testing Dust Grain Models with Prime-Cam Polarization Data

Dust emission at FIR and microwave frequencies arises from grains heated by UV–optical starlight that radiate thermal vibrational emission. Interactions with photons and gas atoms exert torques on the grains, inducing rapid rotation about their axis of the greatest moment of inertia, i.e., their short axis. A rotating grain can develop a magnetic moment antiparallel to its rotation axis through the Barnett effect if the grain material is paramagnetic (Dolginov & Mitrofanov 1976; Purcell 1979). Interaction between the grain's magnetic moment, radiative torques, and the local magnetic field dissipates the component of the rotational kinetic energy perpendicular to the magnetic field, aligning the rotation axis with the local magnetic field orientation. Since the rotation axis of each grain is also its short axis, the total emission from the ensemble of dust grains is linearly polarized perpendicular to the field direction (see Andersson et al. 2015, for a recent review of grain alignment).

The processes of extinction, emission, and alignment are all sensitive to the composition of grains. For instance, grains made predominantly of hydrocarbon materials attain higher temperatures than those made from silicate materials, even in identical radiation fields (Mathis et al. 1983; Li & Draine 2001). Furthermore, polarization has been robustly detected in interstellar extinction features at 9.7 and 18 μm that arise from silicates (Dyck et al. 1973; Aitken et al. 1989; Smith et al. 2000), whereas no polarization has been observed in the 3.4 μm hydrocarbon feature, even on the same sightlines where 9.7 μm polarization is observed (Chiar et al. 2006; Mason et al. 2007). Thus, dust polarization is not only a probe of Galactic magnetic fields but also the composition of interstellar grains. Different assumptions on dust composition can result in stark discrepancies between dust masses inferred from infrared emission, whether it be from high-redshift galaxies, molecular clouds, or protoplanetary disks.

Within the last decade, multifrequency FIR polarimetry has accessed for the first time diffuse regions of molecular clouds and the large-scale diffuse ISM. These observations have challenged long-held notions about the nature of interstellar grains. For instance, the Planck satellite uncovered regions of sky having 353 GHz polarization fractions $\gtrsim$20% (Planck Collaboration XII 2020), well in excess of the maxima predicted by pre-Planck dust models (Draine & Fraisse 2009). Also unexpected was the finding from both Planck at wavelengths $\nu \leqslant 353$ GHz and the BLASTPol balloon telescope between 353 and 1200 GHz that the polarization fraction is essentially frequency-independent (Planck Collaboration Int. XXII 2015; Ashton et al. 2018; Planck Collaboration XI 2020). Models employing separate populations of silicate and carbonaceous grains generically predict that the ratio of polarized to total intensity changes as the relative contribution of the more polarized silicate-bearing grains to the less polarized hydrocarbon-bearing grains increases toward long wavelengths (e.g., Draine & Fraisse 2009; Guillet et al. 2018; Draine & Hensley 2020). Although this is consistent with the dichotomy seen in the polarization properties of the respective extinction features, a frequency-dependent FIR polarization fraction is not observed on diffuse lines of sight.

New types of dust models have been created to explain these findings. Guillet et al. (2018) proposed a suite of models with

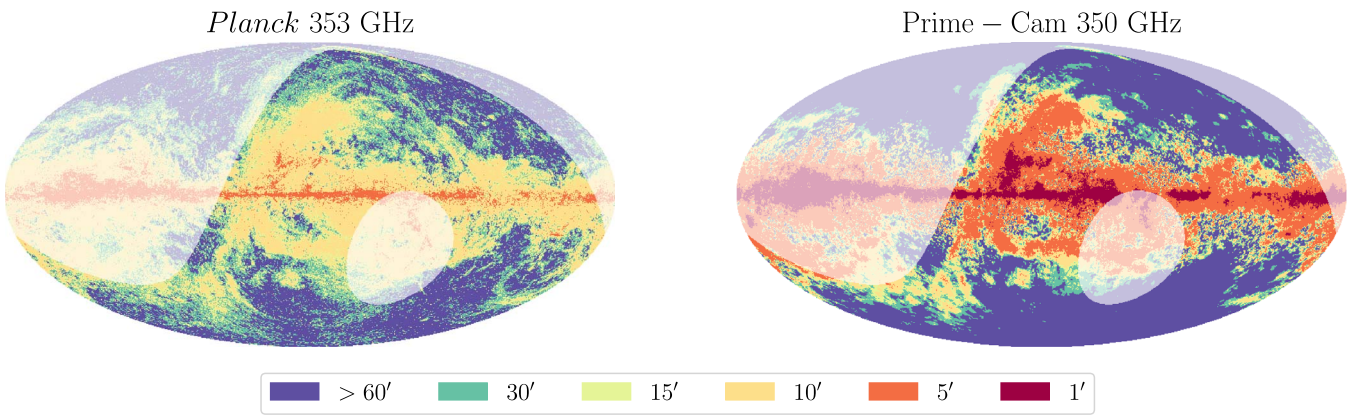

Figure 8. Effective resolution for signal-to-noise ratio >3 measurements of dust polarized intensity with Planck at 353 GHz (left) and FYST with Prime-Cam at 350 GHz (right), for the 4000 hr Wide Field Survey at different levels of spatial resolution. Translucent contours indicate the boundaries of the FYST observable region. Planck measured 3σ detections of the polarized intensity at 5′ resolution only in the inner Galactic plane. Prime-Cam will make comparable measurements over much more of the sky, and along bright sightlines will make high-fidelity measurements at higher angular resolution, as demonstrated here by the additional contour at 1′.

highly elongated grains coming in distinct silicate and carbonaceous varieties. However, these different dust species have sufficiently similar FIR emission properties to push the wavelength-dependence of the polarization fraction below current observational limits. In contrast, Draine & Hensley (2020) proposed that the long-held silicate–carbonaceous dichotomy is incorrect and that interstellar dust exists as a comparatively homogeneous composite. While both models are consistent with current FIR polarimetry, they have starkly different implications for the lifecycles of dust grains and the extent to which they are homogenized in the diffuse ISM. They also make different predictions for measurements of dust polarization at higher frequencies than those accessible by Planck.

Prime-Cam has the frequency coverage and sensitivity to discriminate among these models and thus elucidate the nature of interstellar dust. Tests of dust composition are best conducted on diffuse sightlines, where complicating factors like line-of-sight temperature gradients can be mitigated. We focus here on a nearby translucent cloud in Pyxis, inaccessible to previous experiments lacking the requisite sensitivity, but well matched to the capabilities of Prime-Cam. As demonstrated in Figure 9, Prime-Cam observations of Pyxis can discriminate among dust models at high frequencies where such comparisons have not yet been possible.

Frequency coverage is especially critical for tests of dust models. At long wavelengths, dust emission is in the Rayleigh–Jeans regime, and so different dust populations with different temperatures have similar spectra. The 850 GHz Prime-Cam band is sufficiently close to the peak of the dust spectrum that temperature effects are nonlinear, allowing the spectrum to be decomposed into distinct components. The power of Prime-Cam to discriminate among models in the Pyxis region, especially at 850 GHz, is illustrated in Figure 9. Uncertainties are quoted for a single 15′ region at the mean brightness of Pyxis. We compare these forecasted data to dust models from Guillet et al. (2018; models (A) and (B)), Draine & Hensley (2020; "astrodust"), and a parametric model from Meisner & Finkbeiner (2015) assuming relative polarization fractions of 1.6:1 for the two components ("MF15-like"). We include a comparison at 220 GHz for the SO-LAT survey (Simons Observatory Collaboration 2019), highlighting synergies with SO for whom constraining dust composition is also a principal Galactic science goal (Hensley et al. 2021). The sensitivity and frequency lever arm of the Prime-Cam observations will allow us to assess which of these models, if any, correctly predict the polarization spectrum up to 850 GHz.

The question of dust homogeneity is one of potential importance for CMB experiments. The existence of multiple dust species each with unique emission and polarization properties is a known challenge for parametric component-separation methods (e.g., Kogut & Fixsen 2016; Remazeilles et al. 2016; Hensley & Bull 2018). Also, multiple dust components, each having a unique spatial distribution and SED, lead to frequency decorrelation, a key challenge for widely used foreground mitigation algorithms (see discussion in, e.g., Keck Array & BICEP2 Collaborations 2018; The CMB-S4 Collaboration et al. 2020; Pelgrims et al. 2021). Using sensitive, high-frequency polarimetry of a diffuse region like Pyxis to constrain the presence of multiple dust components thus directly informs dust mitigation strategies, such as appropriate parameterizations of the dust SED.

A diffuse region like the nearby translucent cloud Pyxis is the ideal laboratory for establishing the composition of dust in atomic gas. Nevertheless, Prime-Cam will also target a number of star-forming molecular clouds (see Section 7.4), which are denser environments than Pyxis. In the densest regions of these molecular clouds, specifically toward filaments and dense cores, dust grains are expected to grow in size via coagulation and to form ice mantles, thereby changing their grain chemistry and emission properties. While molecular clouds are a more complex environment than diffuse clouds, they provide an important test of dust grain models under denser conditions that lead to star and planet formation. The scales over which these dust properties begin to substantially change are not well constrained. Thus, by comparing Prime-Cam observations of dust emission and polarization as a function of column density from the diffuse edges of molecular clouds to their denser interiors, we can chart the evolution of dust properties as grains are processed.

Another test of dust grain models in molecular clouds is the efficiency with which grains align with the local magnetic field. Dust grains in the cold dense cores are shielded from UV radiation from the interstellar radiation field and may therefore

Table 3
Prime-Cam Targeted Polarization Surveys

Target	R.A. (deg)	Decl. (deg)	Dist. (pc)	Band[a] (GHz)	θ[b] (pc)	$p_{353\mathrm{GHz}}$[c] (%)	Area (deg^2)	Depth (hr deg^{-1})
Low-mass molecular clouds ($M < 10^4\ M_\odot$)								
Lupus I	235.56	−33.92	160	350	0.029	3	4	10.0
Pipe Nebula	258.43	−27.33	180	350	0.032	3	4	10.0
Musca	187.73	−71.58	200	850[d]	0.015	12	5	12.5
Intermediate-mass molecular clouds ($10^4\ M_\odot < M < 10^5\ M_\odot$)								
Ophiuchus	247.93	−24.47	140	850	0.010	4	8	8.0
Aquila	277.78	−2.16	400	850	0.029	2	4	8.0
High-mass molecular clouds ($M > 10^5\ M_\odot$)								
Orion A	84.62	−6.99	400	850[d]	0.029	4	11	8.0
Vela C	135.10	−44.01	900	850	0.065	3	5	8.0
Translucent cloud								
Pyxis	134.52	−23.14	175	350[d]	0.013	5	20	3.0
Nearby galaxy								
LMC	80.00	−68.50	50,000	350[d]	9.0	3	30	3.3

Notes.
[a] Primary band for observations, possibly distinct from, e.g., early science observation band(s).
[b] Physical beam size at target distance.
[c] Planck 353 GHz polarization fraction.
[d] High-priority targets with coverage at both 850 and 350 GHz. The coverage depth will only be uniform for the primary band.

lack the suprathermal rotation necessary to keep the dust well aligned with the magnetic field. As a result, the dust grains at the centers of dense cores may have lower alignment efficiencies and thus collectively produce less polarized emission. Evidence for this phenomenon can be found in the tendency of the total emission to increase toward high column densities within clouds, without a corresponding increase in the polarized intensity (e.g., Andersson et al. 2015; Pattle & Fissel 2019). This effect complicates inference of the magnetic field geometry from the polarized emission, because the densest regions may contribute minimally to the polarization signal. Prime-Cam will resolve polarization across the molecular cloud from large-scale diffuse emission to emission from many high-density starless cores embedded deep within the molecular clouds (see Section 7.4). Thus, we can quantify the grain-alignment efficiency and test theories of dust grain-alignment mechanisms as the dust grains themselves evolve over different column densities and temperatures within star-forming regions.

7.2. Measuring Properties of Magnetic Turbulence in the Diffuse ISM with Prime-Cam

The structure of the ISM is influenced on many scales by MHD turbulence. Energy injected into the ISM by stellar winds, SNe, and large-scale Galactic processes cascades down a range of scales until it is dissipated. The properties of MHD turbulence affect a wide range of physics—including mediating phase transitions in interstellar gas—that shapes the formation of interstellar structures and the properties of star-forming clouds (Elmegreen & Scalo 2004). Despite its ubiquitous importance in ISM processes, the properties of interstellar turbulence are poorly understood. To understand turbulence, which correlates magnetic field and density structures across a range of scales, it is necessary to make high spatial dynamic range observations of the diffuse ISM. With Prime-Cam we will be able to make high-resolution observations of the polarized dust emission in intermediate- to high-column density regions of sky ($N_\mathrm{H} \gtrsim 10^{21}$ cm^{-2}).

Rich information on the structure of polarized dust emission at low- and mid-Galactic latitudes will be obtained as a component of the Prime-Cam WFS. Figure 8 shows the effective resolution of these dust polarization measurements at 350 GHz, compared to Planck 353 GHz measurements. We show contours of the resolution to which the WFS data must be degraded in order to achieve 3σ measurements of the polarized dust intensity. The Planck effective resolution is computed directly from the publicly available R3.01 Stokes parameters and noise covariance information (Planck Collaboration XI 2020). We forecast the sensitivity of the Prime-Cam system to Galactic dust by comparing a PySM simulation of polarized dust emission at 350 GHz (Thorne et al. 2017) to the rms noise at each resolution using the (Choi et al. 2020a) noise model for a nominal 4000 hr survey over 60% of the sky. At its highest resolution (5′), Planck made 3σ measurements of the 353 GHz polarized intensity over only a small strip of the inner Galactic plane. At equivalent sensitivity, Prime-Cam will map nearly one-third of the sky, with even higher effective resolution measurements in the inner Galactic plane and in targeted observations of selected regions, as described in Table 3. These data can be compared to maps of neutral hydrogen and other high-resolution gas tracers (e.g., Peek et al. 2018), to determine the small-scale structure of the dust polarization (Clark et al. 2015; Clark & Hensley 2019).

The Prime-Cam map of Pyxis will provide excellent data for studying power spectra of polarized dust emission. The distance to Pyxis is approximately 175 pc, based on 3D dust reddening measurements (Capitanio et al. 2017). The sensitivity and angular resolution of Prime-Cam polarization measurements at 350 GHz will allow us to make high-fidelity measurements of the polarized dust power spectra toward Pyxis. An open question in interstellar turbulence is how

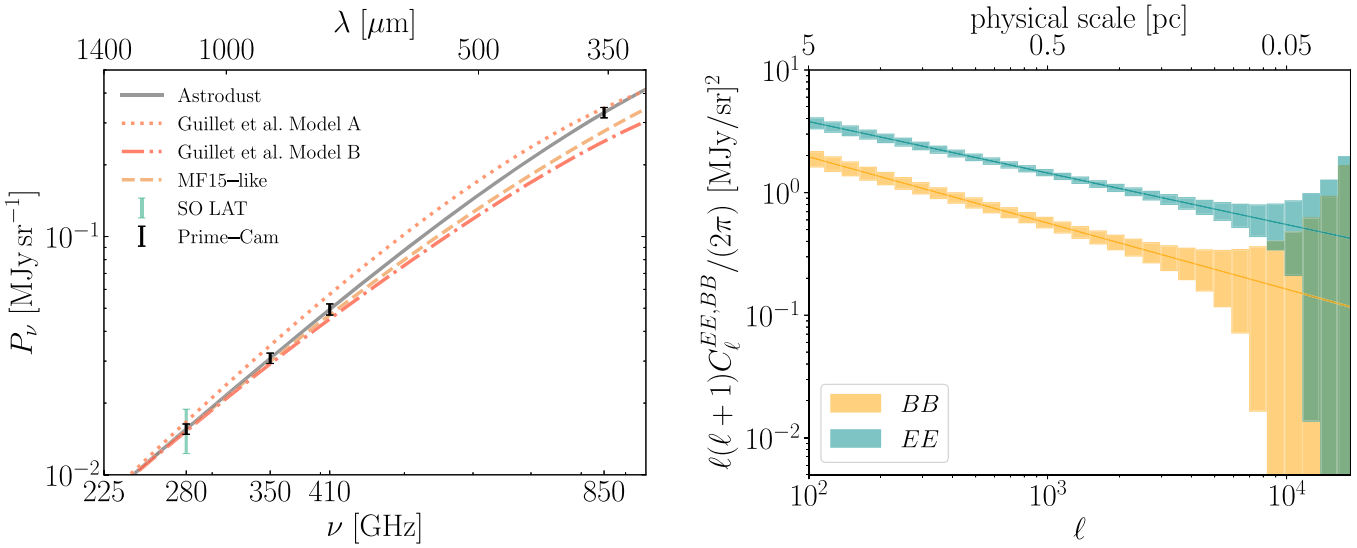

Figure 9. Forecasted dust polarization spectrum (left) and power spectrum (right) of dedicated observations of the Pyxis Cloud. In the left panel, the forecasted observations of a single 15′ (0.8 pc) region are compared with several dust models, all consistent with Planck data, but able to be differentiated among with Prime-Cam observations. A forecast for the SO LAT survey at 220 GHz is presented for comparison. Even more stringent constraints can be obtained by averaging over independent regions within the cloud. The right panel shows the forecasted *EE* and *BB* power spectra of a 350 GHz map of Pyxis. The spectral indices match the Planck fits to 353 GHz power spectra computed over 70% of the high-Galactic-latitude sky. Error bars are computed from the Prime-Cam noise model from Choi et al. (2020a) for logarithmically spaced multipole bins.

(and at what scale) energy from the turbulent cascade is dissipated into the ISM (e.g., Elmegreen & Scalo 2004). The dissipation scale should be associated with a break in the power spectrum on small scales. This break is expected to occur at 0.01–0.5 pc, depending on the properties of the medium, if energy dissipation is driven by turbulent ambipolar diffusion (e.g., Momferratos et al. 2014; Miville-Deschênes et al. 2016). The known distance to Pyxis will allow the power spectra to be associated with a physical scale (see the right panel of Figure 9), and critically, the proximity of Pyxis will enable a search for this break in the power spectrum. Figure 10 is a corner plot (Foreman-Mackey 2016) showing the posterior distributions of broken power-law parameters for forecasted measurements of the *EE* power spectrum.

7.3. The Large Magellanic Cloud: A Multiscale View of Magnetic Fields

The role of magnetic fields in SF and the lifecycle of galaxies is a complex outstanding problem, made difficult by the paucity of high-resolution polarimetric observations. With Prime-Cam we will make a dedicated, high-resolution map of the polarized dust emission in the LMC. Observing the LMC with Prime-Cam affords a unique opportunity to study magnetic fields across different SF environments. On large scales, our dedicated high-resolution polarization survey of the LMC will allow us to study magnetic fields on the scales associated with turbulent energy injection. Maps of the magnetic field structure in the dust can be compared with magnetic field tracers of other ISM phases, such as Faraday RMs with the POSSUM survey (Gaensler et al. 2010), and used in conjunction with atomic and molecular line observations of the LMC at comparable angular resolution, e.g., with the Galactic Australian SKA Pathfinder (Dickey et al. 2013), the SKA (McClure-Griffiths et al. 2015), and CHAI surveys of the LMC.

At a distance of (50 ± 1) kpc, full-resolution Prime-Cam observations of the LMC at 350 GHz will correspond to a physical resolution of 9 pc. The left panel of Figure 11 shows a map of the predicted 350 GHz total intensity of the LMC based on the Herschel SPIRE 500 μm intensity scaled assuming a dust spectral index $\beta = 1.8$, and using the publicly available dust temperature maps from the Herschel HERITAGE project archive (Meixner et al. 2013). Contours indicate where we estimate that Prime-Cam will detect polarized intensity with $\geqslant 3\sigma$ significance (corresponding to polarization angle uncertainty of $< \pm 10°$) at the full 9 pc resolution (cyan) and also when smoothed to 50 pc resolution (blue). For this estimate, we have assumed a constant polarization level of 3%, which is the median Planck 353 GHz polarization level toward the LMC (see Table 3). Based on these predictions, we expect to detect polarization in at least 96 out of the 272 molecular clouds identified in Fukui et al. (2008).

With this unprecedented resolution, we will study the origins of magnetic fields, testing whether their magnetic field direction is consistent with the ordered component of the galactic magnetic field, or alternatively whether there are indications that feedback and galactic turbulence have decoupled the cloud fields from the large-scale fields. Previous studies have had to rely on observations of the molecular clouds in the Galactic disk, which are complicated by line-of-sight confusion and viewing geometry (Stephens et al. 2011), or with CO polarization observations of a small number of clouds in a nearby galaxy (Li & Henning 2011). Our detailed survey will also complement ongoing FIR polarization surveys of nearby bright galaxies with >100 pc resolution, such as the SOFIA Legacy program Magnetic Fields in Galaxies (Borlaff et al. 2021), which is targeting 17 galaxies but will not resolve individual molecular clouds. With deep Prime-Cam maps covering almost the entire LMC, we will map magnetic fields in hundreds of individual molecular clouds and connect the cloud fields to detailed large-scale magnetic field maps.

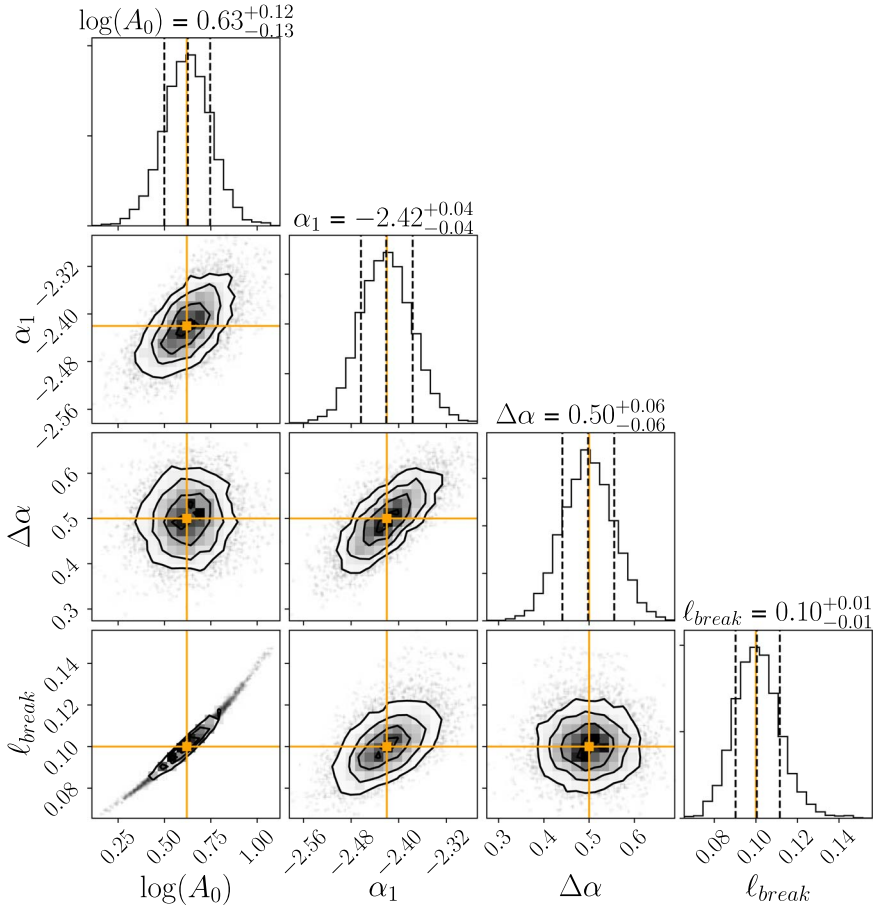

Figure 10. Distributions of broken power-law parameters for forecasted measurements of a dust polarization *EE* power-law spectrum toward the Pyxis Cloud (see Figure 9). We fit four parameters: the power spectrum amplitude A_0, the slope of the power spectrum before the break α_1, the change in the power spectrum slope $\Delta\alpha$, and the power spectrum break scale $\ell_{\rm break}$. The parameters shown correspond to a break in the *EE* power spectrum at 0.1 pc, which we will constrain to within 0.01 pc.

7.4. Measuring the Connection between Cloud Magnetic Field Properties and SF Outcome

Within clumps and filaments of dense gas, strong magnetic fields are proposed to inhibit movement of material across field lines (while the motion parallel to the field lines does not face any resistance), possibly delaying the onset of SF (Inutsuka et al. 2015; Walch et al. 2015). Stutz & Gould (2016) proposed that magnetic fields, if they become concentrated enough, could lead to pinch instabilities that may aid in cluster formation and may be an important component in driving the dynamical state of high line-mass filaments. Regardless of the proposed model, the degree to which magnetic fields affect the SF efficiency within molecular clouds is poorly constrained (Krumholz & Federrath 2019), primarily due to the difficulty in observationally tracing the magnetic fields that thread star-forming clouds (Pattle & Fissel 2019). To address these central issues in our understanding of SF, we require (1) observations tracing cloud-to-core magnetic field properties and (2) maps of magnetic fields in a large sample of clouds over the relevant range in cloud masses and evolutionary stages.

Figure 8 shows that the WFS Prime-Cam 350 GHz survey is expected to achieve high signal-to-noise detections of most of the Galactic plane at better than 1′ resolution. Most MW molecular clouds are observed to be located near the Galactic plane. Dust emission is typically optically thin; therefore we would like to initially study clouds that have minimal line-of-sight confusion, where the magnetic field inferred from Prime-Cam polarization maps can be unambiguously attributed to one cloud. To investigate, we examined the molecular cloud catalog presented in Miville-Deschênes et al. (2017), which uses all-sky 8′.5 resolution observations of $b \pm 5°$ from the Dame et al. (1987) all-galaxy ^{12}CO J = 1−0 survey. Using the cloud data made available on Harvard Dataverse (Miville-Deschênes 2021), we find that 354 clouds in the Galactic longitude range covered by the WFS have less than half their sightlines with more than one cloud at different distances, and also better than 1 pc resolution (assuming a 1 arcmin FWHM beam). Future investigations with higher-resolution cloud catalogs, such as the Herschel Hi-GAL survey (Molinari et al. 2016), may reveal that a larger fraction of nearby clouds have little line-of-sight confusion and can be used in our analysis of cloud magnetic fields.

With this sample, we will investigate the ratio of turbulent and gravitational potential energy to magnetic energy for each cloud, using standard polarization analysis techniques, such as comparing the relative orientation of magnetic fields and cloud column density structures (Soler et al. 2013; Planck Collaboration Int. XXXV 2016; Soler et al. 2017) and by analyzing the joint probability distribution functions of polarization level and disorder in the magnetic field (King et al. 2018). We will also apply the Davis–Chandrasekhar–Fermi method, which uses the disorder in the inferred magnetic field orientation angle to estimate the balance between turbulent and magnetic energy

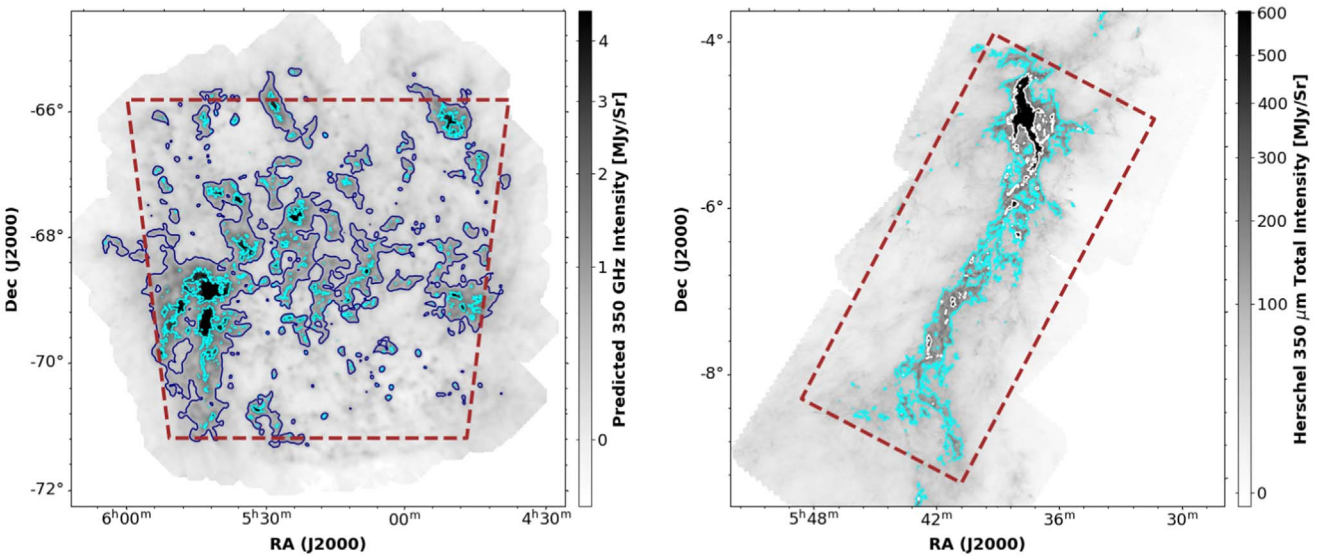

Figure 11. Left panel: predicted regions of the Large Magellanic Cloud where Prime-Cam's 100 hr survey of a 5°.5 × 5°.5 region would be expected to obtain $\geqslant 3\sigma$ 350 GHz polarization detections at full 9 pc resolution (cyan contours) and smoothed to 50 pc resolution (blue contours), assuming the dust in the LMC is 3% polarized. The background image shows a predicted 350 GHz total intensity map based on the Herschel HERITAGE Survey of the LMC. Right panel: Herschel 350 μm (850 GHz) intensity map of the Orion A molecular cloud, with contours showing the regions where our planned 88 hr, 850 GHz Prime-Cam survey will make $\geqslant 3\sigma$ polarization detections assuming 3% (cyan) or 1% (white) polarization levels. In both panels, dashed brown polygons show the area that we plan to survey with Prime-Cam.

(Davis 1951; Chandrasekhar & Fermi 1953; Hildebrand et al. 2009; Houde et al. 2009). We will apply these statistical measurements to clouds observed as part of the WFS survey, our targeted high-resolution Prime-Cam maps of nearby clouds (see Table 3), and also to synthetic polarization observations of numerical simulations (e.g., King et al. 2018; Seifried et al. 2019; Reissl et al. 2021) in order to determine which simulations best reproduce the properties of our observations.

Dust polarization maps are only sensitive to the component of the magnetic field parallel to the plane of the sky. Our analysis of the magnetic field properties would be greatly enhanced by constraining the 3D structure of the magnetic field in each cloud. For clouds with lower levels of confusion (i.e., at least 5° away from the Galactic plane), we plan to use a new technique developed by Tahani et al. (2018) based on Faraday RMs to probe the line-of-sight magnetic field ($B_{\rm LOS}$).

Combining the Prime-Cam dust polarization maps with $B_{\rm LOS}$ maps will enable us to model the 3D magnetic field morphology of dozens of molecular clouds. For example, Tahani et al. (2019) combined the obtained $B_{\rm LOS}$ observations from Tahani et al. (2018), with the available Planck plane-of-sky magnetic fields ($B_{\rm POS}$) to map the 3D morphology of magnetic fields in the Orion A cloud. They concluded that a bow-shaped magnetic field morphology around Orion A is the most probable candidate among the other possible 3D magnetic field morphologies in this region. This bow-shaped magnetic morphology is consistent with the elongated molecular cloud formation scenario of Inutsuka et al. (2015) and MHD simulations of Inoue et al. (2018). We will compare our 3D observations, which will include a range of physical properties and observations in different environments, with the predictions of cloud-formation models. We can further test the accuracy of the determined 3D morphologies by analyzing the level of polarization in dust polarization observations (Chen et al. 2019).

High-resolution, large-area dust polarization maps from Prime-Cam, combined with existing and future $B_{\rm LOS}$ observations will constrain the 3D magnetic field morphology of star-forming clouds, across a range of cloud masses and evolutionary states. The higher resolution of Prime-Cam will allow for a more accurate comparison between $B_{\rm LOS}$ and $B_{\rm POS}$ than is possible using Planck data, particularly for more nearby clouds (distances < 1 kpc), where the $B_{\rm LOS}$ resolution at each point is typically $1'$ or less. We note that future RM catalogs obtained by the new and next generation radio surveys, such as the new Very Large Array All Sky Survey, the POSSUM[52] survey (Gaensler et al. 2010), and future SKA[53] observations (Heald et al. 2020), will allow for more detailed $B_{\rm LOS}$ maps of molecular clouds, with at least 10 times more $B_{\rm LOS}$ detections per cloud. This increased source density in $B_{\rm LOS}$ maps and the improved resolution in $B_{\rm POS}$ observations (by Prime-Cam) will enable more accurate and detailed 3D magnetic field observations of molecular clouds. We also plan to use expected SKA Zeeman measurements (Robishaw et al. 2015) to better constrain our 3D magnetic field models of molecular clouds.

On smaller scales, molecular clouds host a rich range of substructure, including filaments, the densest of which are the preferred locations for most SF, and dense cores, which are the precursors to individual stellar systems (André et al. 2014; Dunham et al. 2014; Stutz & Gould 2016). With $15''$ resolution at 850 GHz (350 μm), Prime-Cam will be the first polarimeter able to directly observe the connection between magnetic fields within cores (at $\lesssim$0.05 pc scales), through filament scales, and up to cloud scales (at $\gtrsim$10 pc), directly tracing the polarization signal over a factor of more than 200 in size. That is, the Prime-Cam observations bridge the present-day and critical observational gap between the low-resolution (but all-sky) Planck maps and the maps of magnetic fields in protostars and disks on the much smaller scales observable with ALMA. Prime-Cam will make an unbiased survey of seven nearby molecular clouds, spanning a wide range of masses and evolutionary

[52] http://www.dunlap.utoronto.ca/~askap.org/possum/
[53] https://www.skatelescope.org/

states (see Table 3 for the planned targets), spending 30–90 hr per cloud for a total of 352 hr. As an example, the contours in the right panel of Figure 11 shows the areas where we expect to make $\geqslant 3\sigma$ detections of polarized intensity, assuming 3% or 1% polarization levels (cyan and white contours respectively) in our planned 850 GHz survey of the Orion A molecular cloud. These estimates are based on the survey depth from Table 3, sensitivity estimates from Table 1, and a Level-3 Herschel SPIRE 350 μm map downloaded from the Herschel Science Archive that was first published in Polychroni et al. (2013). If the dust is at least 3% polarized, then we predict >100,000 independent polarization detections for our Orion A survey. These surveys will allow us to probe the role of the magnetic field in regulating SF relative to that of turbulence, gravity, and feedback from previous generations of SF. Furthermore, our surveys target a range of cloud masses, densities, and levels of SF activity, enabling Prime-Cam to explore how magnetic fields impact SF as a function of cloud properties.

Prime-Cam will also investigate whether or not magnetic fields regulate SF on the scales of filaments and dense star-forming cores. In strong-field models, the magnetic field plays a fundamental role in the formation of dense cores and their subsequent collapse to form stars, disks, and planets (Mouschovias 1991; Price & Bate 2007; Basu et al. 2009). In weak magnetic field models, turbulence determines how cores and stars are able to form (e.g., Mac Low & Klessen 2004; Offner et al. 2010; Li et al. 2014). Connecting clouds to core scales, recent observational studies proposed that the magnetic field in massive clouds has an effect on the cloud and filament gas dynamics (e.g., Stutz & Gould 2016; Soler et al. 2017; Fissel et al. 2019; González Lobos and Stutz 2019; Álvarez-Gutiérrez et al. 2021). Prime-Cam provides a unique tool set with which one can test theoretical models through its large, unbiased, and sensitive dust polarization surveys of filaments and dense cores within molecular clouds.

The combination of observing at 850 GHz, where the cold dust emission peaks, and the high instrument sensitivity, will enable Prime-Cam to conduct large surveys of entire core and filament populations in nearby clouds that cannot be achieved with existing or upcoming polarimeters (e.g., see Pattle & Fissel 2019 for a review). In our seven targeted clouds, we expect to resolve over 1000 cores and hundreds of filaments. As an example, the Mairs et al. (2016) JCMT/SCUBA-2 study of the Orion A cloud found 431 cores, which are all within our 11 deg^2 survey region shown in the right panel of Figure 11. Even if the core polarization level is only 1%, 201 of these cores should be detected in polarization at greater than a 3σ level, which corresponds to a measurement uncertainty in the inferred magnetic field orientation of $\leqslant 10°$. With this large sample, we will investigate the connection between magnetic fields and molecular gas kinematics. For example, the orientations of protostellar outflows are commonly used as an indicator of the angular momentum axis of accretion within dense cores. In a magnetically regulated collapse, magnetic braking is expected to align the core angular momentum axis with the field orientation (e.g., Allen et al. 2003; Hull & Zhang 2019). To date studies of dozens of protostellar cores have found no statistical preference for an alignment of outflow directions and magnetic field orientations (e.g., Hull & Zhang 2019; Yen et al. 2021). However, searching for a 3D dimensional alignment trend is complicated by the fact that both the magnetic field and outflow direction are observed in projection on the plane-of-the-sky. Prime-Cam's polarization surveys will cover hundreds of protostellar cores, including both isolated cores as well as cores clustered within dense environments. We will also use our observations to probe how magnetic fields affect the accretion onto dense cores and dense filaments by searching for correlations between line-of-sight velocity gradients and magnetic field orientation (Gómez et al. 2018; Hu et al. 2020).

Theoretical models also suggest that gravitational contraction could drag magnetic fields inward thus altering their orientation with respect to the larger-scale magnetic field. For example, some strong-field models predict a pinched "hour-glass" shape in dense cores (Galli & Shu 1993; Myers et al. 2018). However, such profiles have only been seen for a handful of cores (Girart et al. 2006; Monsch et al. 2018). Prime-Cam will enhance these statistics by both resolving the magnetic field structure of over 1000 dense cores, and also by quantifying any change in orientation between the core, filament, and cloud-scale magnetic fields in these cores. Such observations will probe the interplay between magnetic fields and gravity, and how they might affect the initial mass of stars and their ability to form disks that eventually produce planets. Finally, Prime-Cam uniquely offers the opportunity to resolve the magnetic field structure toward both starless cores and prestellar cores, i.e., cores that have not yet formed stars.

In summary, FYST/Prime-Cam has both the sensitivity and resolution to map dust linear polarization across cloud scales, while sampling the conditions within clouds, filaments, and cores. These observations will enable the direct evaluation of the plane-of-the-sky magnetic field directions in the cradles of star cluster formation and its connection to the diffuse ISM. Combined with modeling and independent information on the gas radial velocity field and density structure, the FYST/Prime-Cam data will be a keystone in the testing of theoretical frameworks addressing the role of the magnetic field in star-forming systems, as a function of fundamental cloud parameters, such as mass, mass per unit length, gravitational potential, and evolutionary stage.

8. Probing Galaxy and Galaxy-cluster Evolution with Sunyaev–Zel'dovich Effects

CMB photons encounter two effects on their way from the last scattering surface to our telescopes: they are deflected by the gravitational potentials of the large-scale structures, and scattered by free electrons and neutral–partially ionized atoms. The phenomenon of scattering of CMB photons by unbound and highly energetic electrons is called the SZ effect (Sunyaev & Zeldovich 1970, 1972), which is the main scientific focus of this section. The SZ effect comes in multiple flavors, carrying the imprint of various contributing factors of the electron velocity distribution, and disentangling these effects promises new breakthroughs in astrophysics and cosmology. With its high-frequency leverage, FYST will pioneer some of these studies and, in so doing, will also probe the distribution and time-evolution of dust grains within galaxy-cluster environments.

In Section 8.1, the main themes of the SZ science are discussed, along with the impact that FYST will have on improving the galaxy-cluster number counts, determining cluster temperatures via relativistic SZ (rSZ) spectral distortions, and measuring the cosmic growth of structures via the

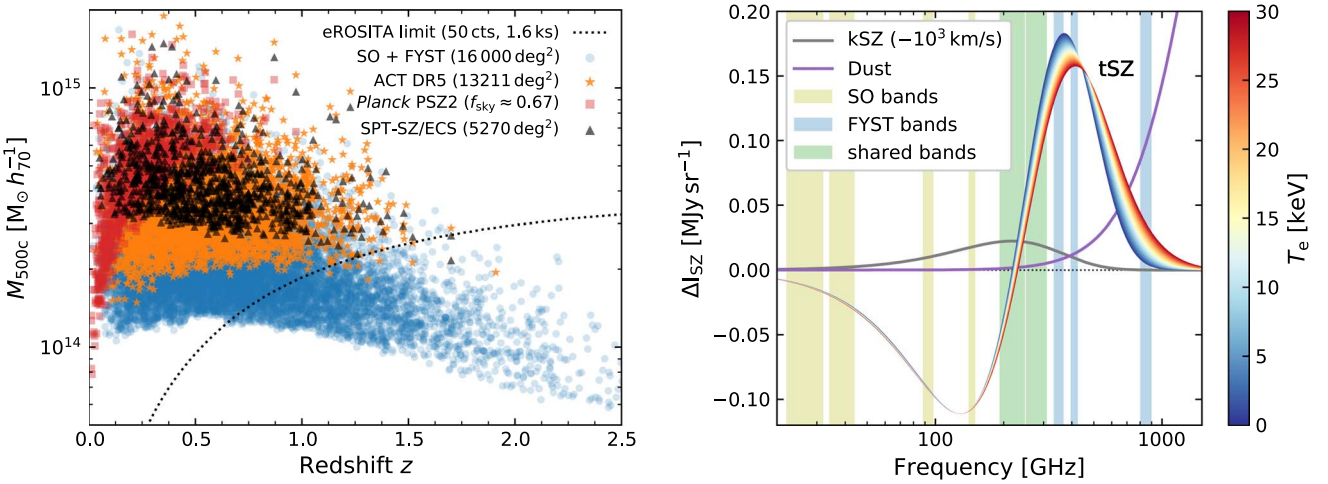

Figure 12. FYST is planned to perform a submillimeter follow-up survey of the sky area surveyed by AdvACT and SO, providing submillimeter observations of around 16,000 galaxy clusters (left). Compared to current SZ-selected cluster samples like those offered by Planck (Planck Collaboration XXIX 2014; Planck Collaboration XXVII 2016), SPT (Bleem et al. 2015, 2020; Huang et al. 2020) and ACT (Hasselfield et al. 2013; Hilton et al. 2021), the predicted SO+FYST cluster sample includes galaxy clusters down to lower masses of approximately $10^{14}\, M_\odot$ and out to higher redshifts of up to ∼3, which is attributed to the lower noise and spectral coverage of SO+FYST. We note that the addition of FYST measurements to SO measurements will not yield significantly more clusters than SO measurements alone. The combination of AdvACT/SO data with data from FYST allows for complete coverage of the spectra of the thermal and kinematic SZ effects (right) at vastly improved sensitivity and spatial resolution compared to Planck. Observations with FYST above the tSZ null at around 220 GHz are especially valuable for temperature measurements of the ICM via the rSZ (color-coded spectra as function of electron temperature T_e) and for characterizing the FIR emission from galaxy clusters that is attributed to warm dust grains in cluster galaxies or the ICM.

kinematic effect. All these science targets will be accomplished in synergy with lower-frequency data from the current and upcoming CMB experiments. Section 8.2 discusses the specific contribution of FYST in constraining the thermal SZ (tSZ) angular power spectrum and the leverage from cross-correlation studies; in Section 8.3, it is outlined how our understanding of the distribution and composition of dust grains in galaxy-cluster environments will be improved; and lastly, in Section 8.4, an example of a new method for detecting the nonthermal SZ (ntSZ) effect for galaxy clusters is described.

8.1. SZ Science with Prime-Cam

Galaxy clusters stand at the nexus between astrophysics and cosmology. Large, statistical samples of clusters have been produced by several observational techniques across multiple wavelength regimes, from X-ray to optical to millimeter wave. Among these various methods to find and characterize galaxy clusters, probably the most rapidly developing is the SZ effect (Sunyaev & Zeldovich 1970, 1972; Birkinshaw 1999; Carlstrom et al. 2002; Kitayama 2014; Mroczkowski et al. 2019). The SZ effect has two main variants, the tSZ effect and the kinematic SZ (kSZ) effect. The tSZ effect arises from inverse Compton scattering of the CMB photons by hot free electrons, has a unique spectral signature, and its amplitude connects to the total cluster thermal energy. The kSZ effect comes from the Doppler shift of CMB photons that have scattered off free electrons that have a nonzero line-of-sight peculiar velocity. To first order the kSZ effect has a blackbody spectrum like the CMB, and its amplitude is proportional to the line-of-sight momenta of these electrons. There is also the full, relativistic spectrum of the tSZ effect (referred to also as the rSZ effect) that potentially carries information about the mean temperature of the scattering electrons (e.g., Wright 1979; Itoh et al. 1998; Nozawa et al. 2009; Chluba et al. 2012), as well as higher-order polarized effects that are probably too weak to detect.

Several thousand galaxy clusters have been identified from observations of the tSZ (e.g., Hasselfield et al. 2013; Planck Collaboration XXIX 2014; Bleem et al. 2015; Planck Collaboration XXVII 2016; Bleem et al. 2020; Hilton et al. 2021), enabling cosmological studies of structure growth based on their number counts and angular correlations; however, current cosmological constraints are limited by systematic uncertainties in cluster properties. Further characterization and understanding the cluster gas properties such as the pressure, temperature, density profiles from tSZ, kSZ, and rSZ measurements aid in reducing the systematic uncertainties in cluster properties and provide valuable information on the detailed astrophysical properties within clusters, like the role that AGN plays in heating of the intracluster gas. A current-generation CMB experiment, Advanced ACTPol (AdvACT; Henderson et al. 2016), and next-generation SO (Galitzki et al. 2018; Simons Observatory Collaboration 2019) provide complete sky overlap with Prime-Cam's large-area survey and are expected to find 16,000 clusters through their tSZ signal (see left panel of Figure 12). Prime-Cam's 220–850 GHz measurements, combined with 30–270 GHz data from AdvACT and SO, are forecasted to enable the detection of all three SZ components (cluster optical depth, bulk velocity, and temperature; Mittal et al. 2018) and thermal dust emission from individual clusters (Erler et al. 2018), for a large, statistically significant cluster sample. The significance of such a detection will depend on the achieved sensitivities of Prime-Cam. Among planned experiments, only FYST will provide observations with sufficiently broad coverage of the SZ increment (see right panel of Figure 12), and will do so with 5 to 20 times better resolution (depending on frequency) than Planck, the current standard for panchromatic SZ science (Planck Collaboration XXII 2016). In addition, spectral imaging of the brightest clusters with EoR-Spec will be possible and could enable SZ component separation. This would represent an evolution of this field toward using spectroscopic SZ science to understand clusters and cosmology. One example of such higher-order spectral distortions that could be unlocked with SZ spectral imaging is the thermal–kinetic SZ effect (which is the relativistic correction of the kSZ effect),

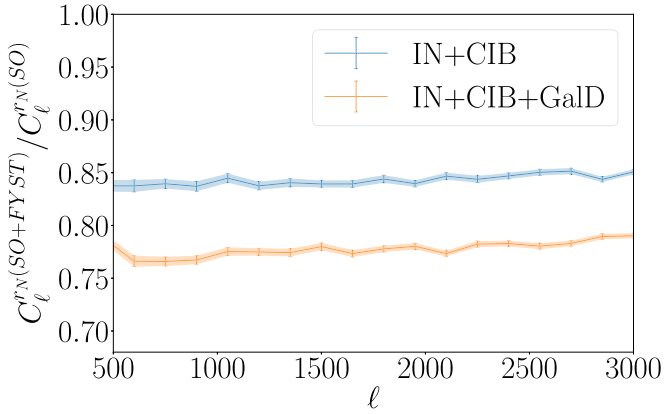

Figure 13. Ratio between the tSZ power spectrum of the cumulative ILC residual(noise $C_\ell^{r_N}$) for SO+FYST combined and SO alone. The ILC residual noise is the noise leftover by contaminants in the reconstructed map, the difference between the recovered signal and the expected signal. The blue trace is the case where the cumulative residual noise is composed of instrumental noise (IN) and CIB. The orange trace is the case where the cumulative residual noise is composed of IN, CIB, and Galactic dust (GalD). We see that the ratio of SO+FYST vs. SO is around 0.84 for IN+CIB and 0.78 for IN+CIB+GalD. The error bars represent the standard error of the binned power spectra over a window $\Delta\ell = 150$.

whose detection possibility is discussed in a recent paper by Coulton et al. (2020).

Advances have been made recently in our theoretical and numerical modeling of how galaxies form and evolve over cosmic time. These theoretical constructs are challenged and verified through observations of the physical and thermodynamical properties of the baryons in galaxies and clusters. High signal-to-noise cross-correlation measurements of the tSZ and kSZ effects provide independent windows into the thermodynamic profiles of ensemble-averaged groups and galaxies (Battaglia et al. 2017; Amodeo et al. 2021; Schaan et al. 2021). These measurements will quantify and constrain the processes that make SF globally inefficient, such as energetic feedback and nonthermal pressure support. Thus, cross-correlations between FYST observations and galaxy, group, cluster, or quasar samples will probe the baryonic processes important for galaxy formation, such as energetic feedback and nonthermal pressure support.

8.2. Prime-Cam Leveraging Ongoing Experiments

A major hurdle for these SZ measurements will be their clean separation from the intrinsic thermal dust emission from galaxies and clusters, which we will refer to as *CIB leakage*. This separation requires the multiwavelength coverage from millimeter to submillimeter wavelengths that FYST provides to avoid biased SZ measurements (Basu et al. 2019). For example, in cluster cosmology, an uncontaminated tSZ map will allow for a more accurate cluster selection function (e.g., Melin et al. 2018). Quantifying the improvement that FYST high-frequency coverage brings to better separate tSZ, and CIB is therefore crucial. Simulations of a mock sky, using templates maps from the WebSky simulations (Stein et al. 2019, 2020), containing tSZ, CIB, and instrumental noise at the frequencies, sensitivities, and resolution of SO alone or SO and FYST combined (SO+FYST) show that, when using a simple map-based internal linear combination (ILC) to retrieve the tSZ, the power spectrum of the cumulative residual noise ($C_\ell^{r_N}$), i.e., the total noise left by the contaminants in the reconstructed ILC map, is 16% less important for SO+FYST than it is for SO alone. Moreover, when adding Galactic dust to the mock sky, the gain in combining SO with FYST is even more pronounced: the power spectrum of the cumulative residual noise in tSZ is 22% less than when SO alone is used (see Figure 13). This gain is due to the high-frequency coverage of FYST that better probes and constrains the Galactic dust that is the dominant contaminant (for more information on the method, modeling, and some complementary results, see M. Charmetant et al. 2022, in preparation). A harmonic-space, constrained ILC procedure, which nulls the CIB contribution, leads to a further 10% improvement (that is ∼25% overall) for SO and FYST combined compared to SO alone when including $1/f$ noise and all extragalactic foregrounds. The tSZ power spectrum is a highly sensitive nonlinear probe of cosmology and astrophysics. For example, its amplitude scales like σ_8 to the eighth power so that a 20% improvement in signal-to-noise ratio results in about a factor of 5 improvement in measuring σ_8. Improvements on tSZ power spectrum signal-to-noise can be roughly converted to real space measurements, for example a cross-correlation analysis, by taking their square root of the power spectrum, assuming a fixed sample size. FYST therefore opens a new unbiased observational window into the thermodynamic properties of galaxies and clusters.

A limitation of the tSZ and kSZ measurements is the lack of redshift information. This can be overcome easily by cross-correlating the FYST-derived SZ maps with the distribution of galaxies with known spectroscopic (as well as good photometric) redshifts. This SZ *tomography* is a powerful technique, enabling the study of the thermodynamical properties of groups and clusters as a function of cosmic time (Vikram et al. 2017; Makiya et al. 2018; Pandey et al. 2019; Chiang et al. 2020; Koukoufilippas et al. 2020; Yan et al. 2021) as well as its connection to the theory of the structure formation (Chiang et al. 2021). The current cross-correlation measurements show a clear sign of the CIB contamination at $z > 1$ (Chiang et al. 2020), which FYST can help mitigate.

8.3. Measuring the Dust Mass and Spatial Distribution of Dust Grains in Galaxy Clusters

Clusters are formed hierarchically through mergers and the accretion of unbound intercluster gas. Infalling galaxies experience tidal distortions and ram pressure, leading to increased rates of SF and the stripping of enriched gas and dust (Sarazin 1988). This process can potentially enrich the intracluster medium (ICM) with warm dust grains, which are stochastically heated by collisions with hot electrons and reemit the absorbed energy in the FIR (Ostriker & Silk 1973; Dwek et al. 1990). However, the lifetime of dust grains in the ICM is highly uncertain. In the cores of galaxy clusters, dust grains can be destroyed efficiently by thermal sputtering (Draine & Salpeter 1979) while estimated grain lifetimes in the outskirts of clusters reach several billion years (Dwek & Arendt 1992; Vogelsberger et al. 2019). Dust in the ICM has been observed statistically by stacking FIR images of large cluster samples (e.g., Montier & Giard 2005; Giard et al. 2008; Planck Collaboration Int. XI 2013; Planck Collaboration Int. XLIII 2016). These observations point to a low dust-to-gas mass ratio of around 10^{-4} and an SED similar to those of local star-forming galaxies (Planck Collaboration Int. XLIII 2016; Erler et al. 2018). However, there is no conclusive evidence for the presence of dust in the ICM of local galaxy clusters. Recent

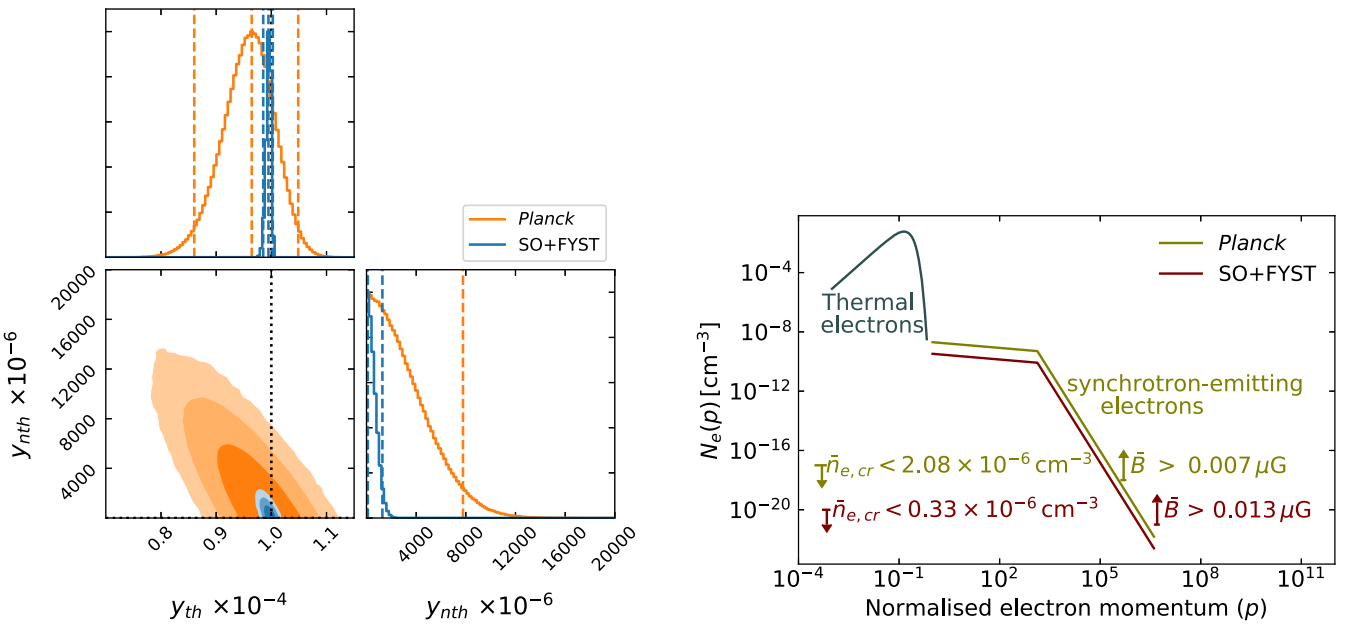

Figure 14. Left: 2D posterior and the 1D marginalized posteriors of the thermal and nonthermal Compton-y parameters (y_{th} and y_{nth}, respectively) are computed using simulated spectra of the SZ effect considering the combined sensitivities of SO+FYST, in comparison with the posteriors computed using Planck sensitivities from data. The contours in the 2D distribution correspond to the 68.3%, 95.4%, and 99.7% credible intervals. Right: constraints on the volume-averaged number densities of cosmic-ray electrons, and the corresponding magnetic field strengths, for a broken power-law electron distribution with $p_{\rm break} = 1000$. The Planck limits are obtained from stacking the spectra of 62 known radio-halo clusters, and the SO+FYST limits are a forecast for 200 clusters with similar radio halo properties. For comparison, the average magnetic field, using the assumed density profile and spectral index of electrons and a central value of 1 μG, will be 0.09 μG.

theoretical work suggests that the majority of dust grains in clusters at low and intermediate redshifts is instead bound in star-forming cluster galaxies (Gjergo et al. 2020).

Understanding the nature and properties of FIR emission from galaxy clusters is a major challenge for precise measurements of the SZ effects at submillimeter wavelengths. Recent spectral studies of the SZ effect highlight the importance of including a dedicated spectral component for the cluster FIR emission and constraining it with high-frequency observations above 220 GHz (Erler et al. 2018; Schaan et al. 2021). Other works suggest that up to 9% of clusters between redshift 0.5 and 0.8 have been missed in the creation of the Planck cluster catalog due to FIR contamination (Melin et al. 2018). Insights into the properties of dust in clusters will be especially important for the analysis of proto-clusters at redshift $z > 2$ (Casey 2016; Cheng et al. 2019; Smith et al. 2019). Clusters at these redshifts are not fully virialized yet, so their ICM has not reached the temperature necessary for efficient sputtering of dust grains (Gjergo et al. 2020). With its access to submillimeter frequencies combined with having more than 5 times better angular resolution than Planck, FYST will help to measure the spatial distribution of diffuse intergalactic dust in the dense cluster environments, and will inform the simulations regarding the origin and lifetime of such dust grains.

8.4. Observations of the Nonthermal SZ Effect

The ntSZ effect provides information about the highly relativistic cosmic-ray electron populations in the ICM (Enßlin & Kaiser 2000; Colafrancesco et al. 2003, 2013). The spectral signature of the ntSZ effect is similar to that of the rSZ effect but is shallower and smaller in amplitude than the rSZ spectrum. Since the ntSZ null is different from the rSZ null, one can exploit this difference in the spectral distortions to distinguish between the thermal and cosmic-ray electron populations. Typically, the overall contribution to the energy budget in clusters from these nonthermal electrons is only about 1% (e.g., Zandanel et al. 2014). This makes a direct detection of the ntSZ effect incredibly difficult, even with the sensitivities of FYST. However, one can place meaningful upper limits on the mean number densities of relativistic electrons by stacking the spectra of a large number of clusters. When this exercise is carried out for clusters hosting radio halos (RHs), the known average synchrotron flux then provides a lower limit on the volume-averaged magnetic field. The limits are obtained under the assumption that the nonthermal electrons causing the ntSZ effect are the same population of electrons that emits synchrotron radiation in RHs. In V. Muralidhara et al. (2022, in preparation), this analysis was performed for a sample of known RH clusters using the multifrequency data from the Planck satellite, and then a forecast was made for 200 RH clusters using simulated sky maps for SO and FYST. The posterior probability distributions of the amplitudes of the tSZ and ntSZ effects, and the resulting limits on the cluster-averaged nonthermal electron densities (as well as B-field values) are shown in Figure 14. The SO+FYST data can provide highly competitive constraints on the average magnetic field within clusters and, when combined with results from Faraday RMs (e.g., Bonafede et al. 2011), can rule out certain simplistic power-law models for cosmic-ray electrons. The value of adding FYST data in this regard is to gain better control over foregrounds, especially dust emission, which will in turn enable a better success with the matched filtering and spectral fitting techniques to get constraints on the ntSZ signal.

9. Rayleigh Scattering: A New, Blue Surface of Last Scattering

Just after recombination, Rayleigh scattering of neutral species can generate a secondary CMB signal. Unlike the primary signal, generated by Thomson scattering, this signal is frequency dependent. The unique frequency coverage of Prime-Cam could potentially help us detect this signal, which eventually will benefit cosmological parameter inference. This section explores the feasibility of a first detection of the Rayleigh signal using Prime-Cam on FYST.

In Section 9.1, we briefly review the physics of CMB Rayleigh scattering and cosmological constraining power enabled by its measurement. In Section 9.2, we discuss the detectability of the Rayleigh signal. We will comment on the role of the atmosphere and show how this affects detectability prospects with Prime-Cam. Finally, we will show the impact of foregrounds in Section 9.3.

9.1. Rayleigh Scattering of the CMB

Prior to recombination around redshift 1100, the universe was optically thick due to frequent Thomson scatterings of CMB photons by free electrons. As electrons became bound into neutral hydrogen, the rate of Thomson scattering dropped, and the universe became nearly transparent. However, the neutral species formed during recombination (primarily hydrogen and helium) also scattered CMB photons through Rayleigh scattering, the classical scattering process of long wavelength photons by the induced dipole of polarizable particles (Rayleigh 1881; Takahara & Sasaki 1991; Yu et al. 2001; Lewis 2013; Alipour et al. 2015). Rayleigh scattering exhibits a strongly frequency-dependent cross section ($\propto \nu^4$) (Rayleigh 1881). This additional scattering produces a frequency-dependent shift of the visibility function toward later time (smaller redshifts). At the power spectrum level, this results in the following effects:

1. There is a suppression of small-scale anisotropies both in temperature and *E*-mode polarization, caused by an increase of diffusion damping.
2. On large angular scales, Rayleigh scattering primarily affects the *E*-mode polarization signal. By shifting the last-scattering surface toward lower redshifts, where the local temperature quadrupole is larger, Rayleigh scattering boosts the large-scale *E*-mode signal.
3. Rayleigh scattering introduces frequency dependence in the size of the sound horizon, leading to a shift in the location of the acoustic peaks, both in temperature and *E*-mode polarization spectra.

Rayleigh scattering of the CMB is a definite prediction of standard cosmology. However, a first detection has yet to be achieved and is further made challenging by the small amplitude of the signal. With sufficient sensitivity and frequency coverage, the additional cosmological information carried by the Rayleigh-scattering signal can improve constraints on cosmological parameters. For example, the forecasts show that an experiment like PICO (Hanany et al. 2019) would be able to use Rayleigh scattering to improve the constraints on the sum of the neutrino masses $\sum m_\nu$ by up to 50%. Similarly, the constraint on the number of relativistic species $N_{\rm eff}$ would be improved by ∼10% (Beringue et al. 2021). The fact that the Rayleigh signal is effectively a second last-scattering surface could potentially also benefit the search for primordial non-Gaussianities (Coulton et al. 2021), which could lead to an improvement greater than a factor of 2 compared to an analysis using only primary CMB modes.

The broad frequency coverage (270–850 GHz) and wide survey area (Figure 2) of Prime-Cam could potentially contribute to a first detection of CMB Rayleigh scattering, especially in combination with surveys covering lower frequencies. Furthermore, with the location of FYST at an elevation at more than 5600 m above sea level, the assumptions made in the forecasts presented here are likely to be somewhat conservative with respect to the impact of the atmosphere on the observation of large-scale anisotropies.

9.2. Detectability of the Rayleigh-scattering Signal with CCAT-prime

The first detection of the Rayleigh signal will be in cross-correlation with the primary CMB. Despite several experiments measuring CMB anisotropies on large scales from space (e.g., Planck; Planck Collaboration XI 2020), as well as on smaller scales from the ground (e.g., ACT, Thornton et al. 2016; SPT, Austermann et al. 2012), there has not been any reported detection of Rayleigh scattering of CMB photons. As highlighted in Figure 15, Planck observed the CMB with sufficient depth that in principle a statistical detection of the CMB-Rayleigh cross-correlation could have been possible. The presence of astrophysical foregrounds, as well as limited sensitivity of Planck in polarization, is likely to have prevented a first detection.

Similarly, Figure 15 shows that the raw sensitivity of Prime-Cam would be sufficient for a detection of the Rayleigh-scattering signal. Because Prime-Cam will produce polarization maps with unprecedented resolution and sensitivity and it will measure foreground contamination on small scales at very high frequencies (see Section 9.3), theoretically this would benefit detectability prospects. However, FYST is a ground-based observatory, and the atmosphere will hinder the extraction of the cosmological information from large-scale anisotropies. This is especially true in temperature, as highlighted in Figure 15. Atmospheric effects should have less of an impact on the observation of polarization fluctuations, and Prime-Cam will provide complimentary information in currently unobserved regimes (high frequencies and small angular scale polarization anisotropies).

Finally, we stress that the CCAT-prime noise model is currently calibrated on available ACT measurements. Its knee frequency, $\ell_{\rm knee}$, must be less than 200 in order for Prime-Cam to obtain a detection. Based on the expected scaling of the ACT-measured atmospheric noise rms with PWV (and thus altitude) and its power law spectrum PSD $\sim k^{-11/3}$, we expect $\ell_{\rm knee} \sim 800$ compared to the $\ell_{\rm knee} \sim 1000$ at the ACT site and used in these forecasts. It seems therefore optimistic to expect such a low knee frequency.

9.3. Mitigation of the Impact of Foregrounds

Besides the impact of the atmosphere, and similar to observations of primary CMB anisotropies, the Rayleigh-scattering signal will be affected by astrophysical foregrounds. Fortunately, several unique properties of the Rayleigh-scattering signal can be leveraged to mitigate the impact of foreground contamination. In this analysis, we include CIB, SZ, radio point sources, dust, and synchrotron foregrounds. We

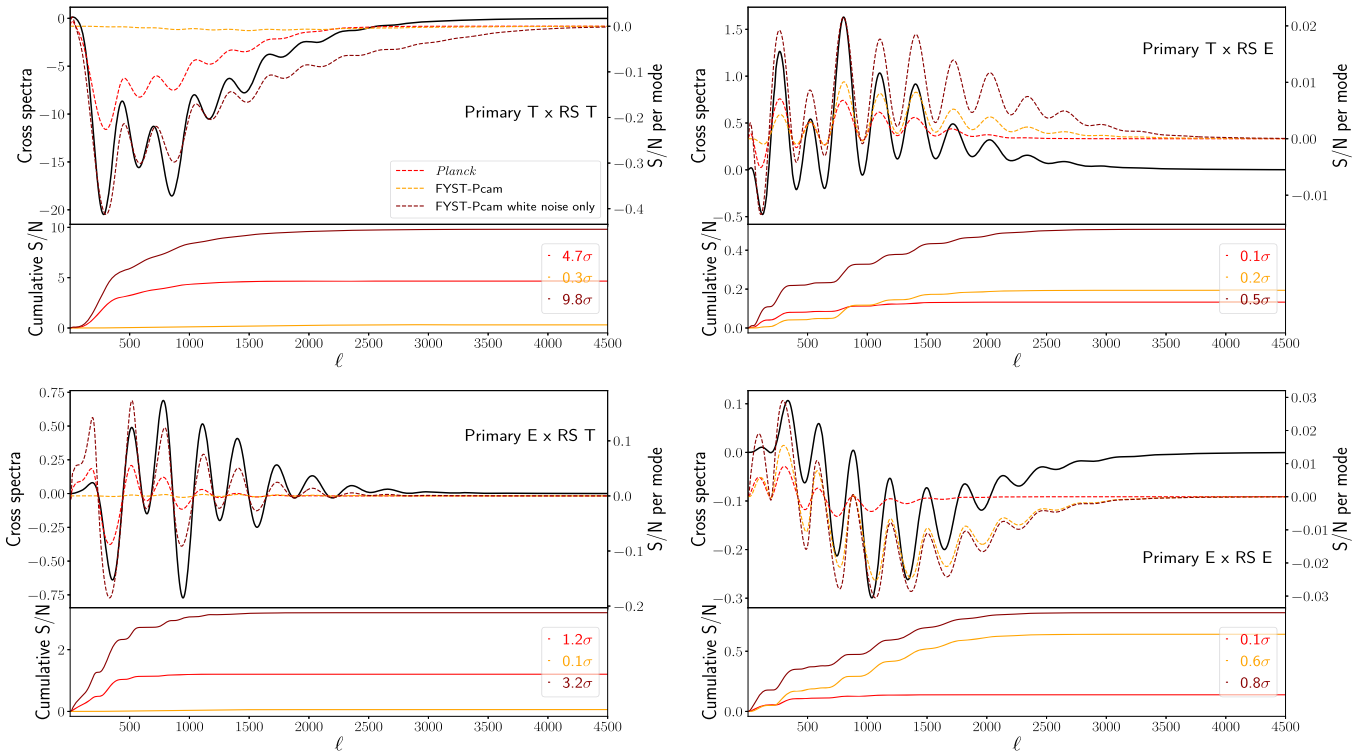

Figure 15. Detectability of the four primary×Rayleigh cross-power spectra for three experiments: Planck (red); Prime-Cam (orange); and Prime-Cam white noise only (dark red). Black lines show the cross-spectra while colored dashed lines show the signal to noise per ℓ-mode. The bottom panels display the cumulative signal to noise. Note that these forecasts do not include any foreground contamination.

find that the CIB and dust and radio point sources dominate in foreground mitigation.

First, the frequency scaling of Rayleigh scattering ($\propto \nu^4$ at lowest order) is unique, since no foregrounds exhibit such a scaling. This makes Rayleigh scattering suitable to use with *blind* component separation methods such as ILC approaches. Second, Rayleigh scattering is a robust prediction of standard physics so that, once the cosmological parameters are fixed, the Rayleigh-scattering signal can easily be modeled, and included in *parametric* foreground-cleaning techniques.

Measuring the cross-correlation between the primary CMB and the Rayleigh signal will require the removal of foreground contamination from two maps: a map of the primary CMB; and a map of the Rayleigh-scattering signal (at a reference frequency). In order to avoid biasing the detection, one has to be careful to avoid residual primary CMB in the Rayleigh-scattering map (and vice versa). This demands the use of a constrained-ILC method (Remazeilles et al. 2011).

Figure 16 shows the impact of the foregrounds on the detection of the Rayleigh-scattering cross-correlation using a constrained-ILC. As expected, a larger penalty has to be paid in temperature where foregrounds are brighter than in polarization. However, we should note that resorting to a constrained-ILC increases the noise in the reconstructed maps. Using more advanced component-separation techniques such as SMICA (Planck Collaboration IV 2020) could further improve the signal-to-noise ratio of the cross-correlations, while also making use of the known ℓ-shape of the Rayleigh-scattering signal.

In conclusion, atmospheric noise and foregrounds will make it unlikely that Prime-Cam alone will be able to make a detection of the Rayleigh signal. Future work will be undertaken to determine if combining Prime-Cam with other

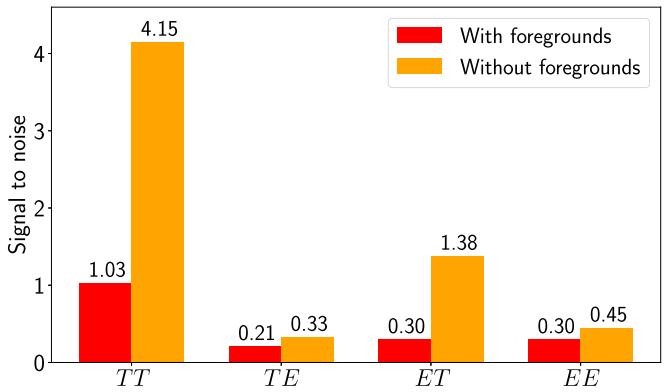

Figure 16. Effect of foregrounds on the forecasted signal to noise of the detection of the Rayleigh-scattering cross spectrum using Prime-Cam combined with Planck. As expected, foregrounds have a larger effect on temperature, making a detection of Rayleigh scattering challenging. These forecasts have been carried out using a constrained-ILC (Remazeilles et al. 2011) algorithm in order to avoid residual bias.

experiments, such as SO and Planck, as well as resorting to more advanced foreground mitigation techniques, and will make a first detection with currently planned experiments realistic. Within the collaboration, current efforts are focused on improving the forecasts by injecting more realism while also exploring new methods to clean foregrounds.

10. A New Submillimeter Window into Time-domain Astrophysics

Compared to other parts of the electromagnetic spectrum, relatively few submillimeter studies have focused on the time

domain. Nevertheless, systematic submillimeter observations in the time domain open up a wide open discovery space for variable and transient phenomena, and the opportunity to quantify the physical properties of variable sources captured in this regime. These phenomena stretch across timescales from seconds to years, arising from young stellar objects (YSOs) through supermassive black holes and with both thermal and nonthermal origins.

We begin in Section 10.1 with examples of the types of transient events expected in the submillimeter and the typical timescales associated with their variation. Next, in Section 10.2, we describe the opportunities for commensal time-domain investigations during the WFS and DSS large surveys. Finally, in Section 10.3, we present the focused time-domain observations for protostars, explosive sources, tidal-disruption events, and fast transients.

10.1. Submillimeter Time-domain Overview

We already know that FYST will be able to monitor the variability of thousands of known AGN, as well as tracking the motion of hundreds of asteroids. However, there will also be new classes of submillimeter sources probed with a cadence of minutes to months. As a specific example, deeply embedded YSOs exhibit submillimeter time-variable behavior, typically due to changes in the mass accretion rates adjusting the equilibrium temperature of the enshrouding envelope (e.g., Contreras Peña et al. 2020; Lee et al. 2020), with observed timescales from weeks to many years. Magnetic reconnection events in stellar flares have been detected at millimeter and submillimeter wavelengths from low-mass stars (MacGregor et al. 2020; Guns et al. 2021; Naess et al. 2021) and T Tauri stars (Bower et al. 2003; Mairs et al. 2019) with timescales as short as 15 minutes through a few hours and with multiple detections over 6 days (e.g., a chromospherically active binary whose dwarf star may be about to arrive, or recently has arrived, on the main sequence; Naess et al. 2021). Cycles of dust formation and destruction can lead to periodic variability in asymptotic giant branch stars, while free–free emission with origins in the radio photosphere may also contribute (Dharmawardena et al. 2019, periods and optical-to-submillimeter lags on a few year timescales).

As a second example, although relativistic jets are often probed at lower frequencies, submillimeter observations have revealed the synchrotron emission from relativistic jets in black hole X-ray binaries on timescales significantly less than an hour (Tetarenko et al. 2017), quiescent supermassive black holes like Sgr A* (Subroweit et al. 2017), and gamma-ray-bright blazars (Fuhrmann et al. 2014), probing the jet physics at scales close to where electrons are first accelerated. Energetic (and often explosive) transients like SNe, GRBs, merging neutron stars, and TDEs produce shocks in the surrounding circumstellar medium and ISM on hour-to-day timescales (Ho et al. 2019). At the extreme mass end, recently, Event Horizon Telescope measurements of the wobbling shadow of the black hole in M87 have been analyzed on timescales of days to years (Wielgus et al. 2020).

While limited time-domain studies utilizing the submillimeter have been ongoing for years (e.g., the transient sources illustrated in Figure 17), the lack of sensitive facilities has kept these studies in a state of infancy compared to the radio, UVOIR, and X-ray regimes. Moreover, most submillimeter studies to date have arisen from small, directed observational campaigns, as opposed to larger, more general surveys (see Whitehorn et al. 2016; Herczeg et al. 2017; Guns et al. 2021; Naess et al. 2021, for recent examples of the latter). As time-domain surveys in the optical take center stage in the upcoming decade, time-domain measurements at other wavelengths will be increasingly important for determining the physical processes behind the wide variety of transient and variable events uncovered in our universe. In this regard, the submillimeter is particularly important because of its ability to unveil the dust-enshrouded and nonthermal regimes.

FYST has the capacity to dramatically improve our knowledge of the submillimeter time domain universe through a combination of broad, general-survey approaches and specially crafted, targeted campaigns. With these approaches, FYST will lead the systematic study of submillimeter variability, on timescales from seconds to many years, particularly at the highest submillimeter frequencies.

10.2. Capturing the Time Domain through Commensal Observations

As a predominantly survey-oriented camera simultaneously observing continuum emission at five frequencies between 220 and 850 GHz (1.3 mm and 350 μm), Prime-Cam offers an exceptional platform for commensal submillimeter transient studies. The two large survey programs, WFS and DSS, described earlier in this paper, will monitor an extremely broad range of areal coverage and observing depths over hundreds of nightly epochs.

The primary science drivers for the WFS and DSS are described in Section 3.2 above. We will utilize data obtained during these 4000 hr surveys for relatively shallow but extremely wide-field monitoring of transients in the WFS, and very deep but narrow-field monitoring during the DSS. Table 4 lists the cadence and depths that we will obtain at each of the five continuum frequencies.

The WFS aims to uniformly cover 20,000 deg^2 over 4000 hr (see Table 2) by scanning at fixed azimuth and allowing sky rotation to fill in the observable field during approximately 8 hr of observations per night. The survey provides an unprecedented opportunity to uncover extremely rare but strongly brightening events in the submillimeter regime (see Table 4) between individual epochs. Coadding observations over multiple epochs will allow for deeper searches of longer duration events (e.g., on daily, weekly, and monthly timescales). Given the proposed scanning strategy, Prime-Cam will provide close to simultaneous (separated by $\sim$10 minutes) brightness measurements at all five frequencies covered by the continuum cameras.

The DSS dedicates 2000 hr each to two 4 deg^2 fields observed with the EoR-Spec modules. As the DSS survey unfolds, the other Prime-Cam instrument modules will scan neighboring swaths of sky (see Section 3.3). Each camera band will observe approximately the same patch of sky from night to night, but the overlap of coverage between frequency bands will be minimal, resulting in deep coverage maps at up to five frequencies that have little overlap on the sky. For each of the continuum cameras, these smeared out patches of the sky (compared to the DSS), each covering $\sim$12 deg^2, will provide an unprecedented opportunity to uncover brightening events at submillimeter frequencies over a wide range of flux densities (see Table 4) between individual nightly epochs.

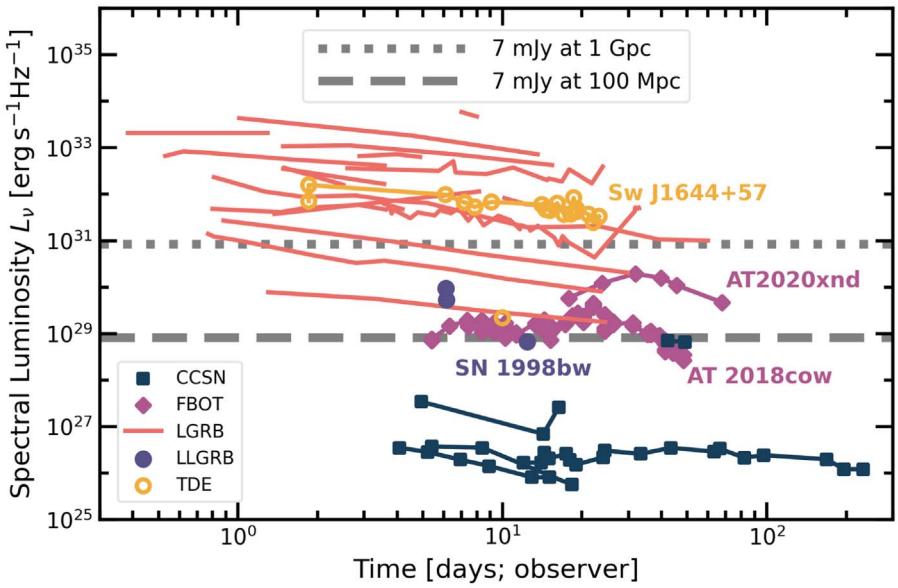

Figure 17. Sample lightcurves of extragalactic transients detected at (sub)millimeter wavelength. Five class types are displayed: core-collapse supernovae; faint blue optical transients (FBOTs); long-duration gamma-ray bursts; low-luminosity gamma-ray bursts (LLGRBs); and tidal disruption events (TDEs). In 1 hr in the top 50% driest conditions, FYST observations at 350 GHz will be able to detect: the brightest (long) gamma-ray bursts with $z \lesssim 0.2$ (1 Gpc), with sensitivity to LLGRBs within 100–300 Mpc; TDEs like Swift J1644+57 with $z \lesssim 0.2$; and FBOTs like AT2018cow and AT2020xnd within 100–300 Mpc. These detection limits, indicated by horizontal lines, assume a 5σ detection, a 1.4 mJy beam^{-1} sensitivity, and a flat spectral index for the (typically longer) wavelengths where these sources were detected. At 220 GHz and 280 GHz, FYST will be sensitive to objects ∼50% more distant. This image was adapted from lightcurves collated in Ho et al. (2022), with additional information from de Ugarte Postigo et al. (2012), Urata et al. (2015).

Together the WFS and DSS will enable a wide range of commensal transient science, from Galactic stellar flares through distant blazars. For example, stellar flares are an important tracer of stellar activity, particularly in young stars and chromospherically active binaries. These flares may play a role in limiting the habitability of planets around young stars, making them an important target. The stellar flares are thought to arise from magnetic reconnection, leading to either synchrotron or gyrosychrotron emission (Bower et al. 2003; Massi et al. 2006). Approximately 23 stellar flares have been detected in the submillimeter regime (see Figure 4 in Guns et al. 2021), with 17 of these coming from dedicated general submillimeter transient surveys (Mairs et al. 2019; Guns et al. 2021; Naess et al. 2021) where the stars were not specifically targeted. In some of the brighter stellar flares, where spectral information was available, the flares roughly followed $S_\nu \propto \nu^0$ to $S_\nu \propto \nu^1$ behavior; however, the faint stellar flares from M dwarfs showed a variable spectral index $S_\nu \propto \nu^{-2}$ to $S_\nu \propto \nu^2$ on timescales under 1 minute. This raises the question as to whether most stellar flares will have a rising or falling flux density with increasing submillimeter frequencies—an issue that FYST's large surveys at a variety of flux-density levels can address. We predict of order 1000 stellar flares will be detected commensally during FYST's two primary surveys, increasing the known numbers by 2 orders of magnitude. If the spectral shape of $S_\nu \propto \nu^{-1}$ is more representative, we will likely detect at least a factor of 3 fewer sources at 220 GHz, and even fewer at 280 GHz. The combination of the WFS and DSS makes FYST an excellent tool for disentangling the submillimeter properties of stellar flares.

Compared to stars, the number densities of blazars are significantly lower. However, in blazars, we aim to characterize day-to-week timescale variability around a relatively bright flux density as opposed to just searching for transient phenomena. There are approximately 600 blazars with measured 143 GHz flux densities over the whole sky (Massaro et al. 2015). Since these sources have a (nonsimultaneous) 1.4–143 GHz spectral index of $0.06^{+0.18}_{-0.43}$ (90% confidence interval), the blazars are best observed at 220 GHz with the WFS. Assuming a median flat spectral index, and extrapolating the 143 GHz flux densities of blazars from Massaro et al. (2015) and the 1.4 GHz flux densities from the blazar samples of D'Abrusco et al. (2019), the WFS should detect 300–600 blazars above 400 mJy in each nightly epoch. This flux density is sufficient to measure (3σ) excess variance at the roughly 10% level. This would generate a rich data set to explore AGN science. For instance, neutrino experiments like the IceCube Neutrino Observatory are now routinely detecting new astrophysical neutrinos above 0.1 TeV and localizing them to a few square degrees (e.g., the neutrino identified with the blazar TXS 0506+056; IceCube Collaboration 2018). The FYST variable blazar sample will provide a powerful real-time resource for identifying flaring blazars that might be generating these neutrinos.

10.3. Focused Time-domain Observations

While the commensal time-domain observations discussed previously will present an opportunity to analyze the variability rate and amplitude of rare brightening events across roughly half the sky, there are several situations where dedicated monitoring for submillimeter variability is preferred. This is especially true for cases where the sources to be monitored are known to reside in discrete, clustered locations, such as Galactic YSOs located within star-forming molecular clouds. Furthermore, there will be time-limited opportunities where either FYST or other telescopes identify a varying source, and dedicated submillimeter follow-up monitoring will provide important and unique information. Below we focus on three specific examples.

Table 4
Primary Survey Areal Coverage and Sensitivity Per Epoch

Survey	Coverage (per epoch) (deg^2)	Frequency (GHz)	Integration ($beam^{-1}$) (s)	Detection Q1 (5σ) (mJy $beam^{-1}$)	Detection Q2 (5σ) (mJy $beam^{-1}$)	Detection Q3 (5σ) (mJy $beam^{-1}$)
WFS[a]	10000	850	0.6	1500	3500	10,000
		410	2.7	300	450	850
		350	3.7	150	200	350
		280	2.8	70	85	100
		220	3.4	55	65	85
DSS[b]	12	850	360	65	150	500
		410	1600	12	20	35
		350	2100	5.5	8.0	15
		280	1600	3.0	3.5	5.0
		220	2000	2.0	2.5	3.5

Notes.
[a] The WFS will observe for roughly 8 hr each epoch, covering half its full extent. Each location within the final map will be observed over 250 epochs.
[b] The DSS will observe for roughly 6 hr each epoch per field, during which time the continuum cameras will scan over a fixed arc covering roughly 12 deg^2. Each region will be observed over 360 epochs.

10.3.1. Scheduled Monitoring of Variable Protostars

For 5 yr, the JCMT Transient Survey has monitored eight nearby low-mass star-forming regions at submillimeter frequencies, with a monthly cadence (Herczeg et al. 2017). The JCMT survey remains the only long-term dedicated time-domain study of deeply embedded protostars, significantly increasing our understanding of accretion variability by carefully constructing the data reduction and analysis procedures to achieve ∼2% relative flux calibration across epochs (Mairs et al. 2017). The Transient Survey has revealed that on timescales of years the dominant submillimeter variability is secular—approximated by either linear or sinusoidal brightness curves—with scant evidence of stochastic, epoch-to-epoch variability above the measurement noise (Johnstone et al. 2018). After 4 yr, the number of confirmed protostellar variables is 17 out of 51 sources brighter than 350 mJy $beam^{-1}$ at 350 GHz (33%; Lee et al., submitted). From this sample, EC 53 in Serpens Main (also known as V371 Serpentis) shows a quasi-periodic lightcurve, allowing for a detailed quantitative investigation into the location and source of the underlying accretion instability (Lee et al. 2020).

Many JCMT Transient Survey sources show significant time-localized structure within the brightness curves. Small number statistics and the short time duration of the JCMT survey, however, limit a statistical analysis coupling these observations directly to theoretical models. A comparison with multiepoch observations of the same sources taken at mid-IR frequencies (Contreras Peña et al. 2020), and utilizing radiative transfer models (MacFarlane et al. 2019a, 2019b; Baek et al. 2020), confirms that the observed submillimeter brightness scales with the time-varying temperature of the enshrouding envelope, itself responding to the changing accretion luminosity. Thus, the relative submillimeter response is *weaker* than the mass accretion response (the temperature variation in the envelope scales approximately as $T \propto L_{\rm acc}^{5}$; Contreras Peña et al. 2020). Thus, the typical 10% submillimeter brightness variation detected over a few year timescales relates to an order of unity variation in the mass accretion—these observed events are not insignificant perturbations.

Such variability of deeply embedded protostars is expected. Within dense molecular clouds, initial overdensities of gas become gravitationally unstable to collapse and seed the formation of stars (Shu 1977; Shu et al. 1987; Masunaga & Inutsuka 2000). As this material accretes onto each protostar, a fraction of the released gravitational potential energy is converted into radiation, which in turn heats the optically thick surrounding envelope. Thus, throughout the earliest stages of mass assembly, the YSO is observable only indirectly through the warmth of its enshrouding material, referred to as the "protostellar core" (e.g., Johnstone et al. 2013). The accretion history is expected to be time variable, both on million year stellar-mass assembly timescales and over short times associated with the many potential dynamical instabilities within the system (Armitage 2015).

In detail, the core's initial angular momentum leads to infalling material forming a disk rather than plummeting directly onto the YSO. Without appropriate viscous dissipation within the disk, the infalling material will accumulate until the disk triggers gravitational instabilities, either within the disk itself (disk fragmentation) or between the disk and the YSO (spiral torques). Timescales for triggering these outer-disk gravitational instabilities are typically thousands of years (Vorobyov & Elbakyan 2018). Once the instability takes over, the disk material is flushed onto the YSO on Keplerian timescales, tens to hundreds of years, and the cycle may repeat multiple times. Alternatively, viscous dissipation within the disk should lead to ongoing disk accretion flow, although there is no a priori expectation that this dissipation rate should match the accretion rate onto the disk from the core or that the disk dissipation should vary smoothly throughout the disk (Zhu et al. 2010; Nayakshin & Lodato 2012; Bae et al. 2014). Mismatched processes will manifest as accretion variability with timescales related to either the viscous dissipation timescale at the discontinuity or the local Keplerian timescale, the latter of which becomes days near the inner edge of the disk (Lee et al. 2020).

There are few empirical studies detailing the time dependence of mass accretion, despite the theoretical expectation. Most observational evidence for protostellar variability comes from rare but extreme brightening events—FU Ori and EX Ori sources—and a handful of multiepoch experiments (Hartmann & Kenyon 1996; Audard et al. 2014; Contreras Peña et al. 2017), many of which target the most evolved YSOs.

Table 5
Per Epoch Observing Time Required to Reach Targeted Depth

Survey	Coverage (per epoch) (deg^2)	Frequency (GHz)	Detection (5σ) (mJy $beam^{-1}$)	Time Q1 (s)	Time Q2 (s)	Time Q3 (s)
PS Monitor[a]	4	850	300	320	1500	⋯
		350	25	340	710	2000
Localized ToO[b]	⋯	850	55	610	2900	⋯
		410	15	980	2400	8600
		350	7	1400	2900	8000
		280	3	1500	2300	4600
		220	3	1100	1600	2800

Notes.
[a] The Protostar Monitoring Survey will observe each region every 2 weeks.
[b] The localized target-of-opportunity (ToO) calculations are appropriate for sources known to within a quarter of the field of view of the camera module. These numbers assume that a portion of the camera remains on the source for the entire observation, increasing the observing efficiency significantly compared with mapping and allowing for rapid subscan analysis.

Table 6
Protostellar Variability Monitoring Fields and Source Counts

Target Field	R.A. (J2000) [hh:mm]	Decl. (J2000) [dd:mm]	Class 0/I[a] (Total)	Class II[a] (Total)	Submm Peaks[b] (>0.1 Jy $beam^{-1}$)	Class 0/I Targets[c] (Submm Bright)
Perseus	03:29	+31:06	69	92	62	35
Orion A (OMC)	05:36	−05:42	190	1600	287	47
Orion B (South)	05:42	−01:54	46	287	28	10
Orion B (North)	05:46	−00:06	60	238	71	22
Ophiuchus	16:27	−24:24	52	152	52	11
Serpens (North)	18:29	+00:30	52	180	33	15
Serpens (South)	18:29	−02:02	115	589	122	21
Carina	10:44	−60:04	...	...	...	...
Galactic Center	17:46	−28:56	...	...	>1000	...
M17	18:19	−16:30	...	...	181	...

Notes.
[a] Young stellar object source counts for Gould Belt Regions based on catalogs by Dunham et al. (2015), Megeath et al. (2016).
[b] Submillimeter (submillimeter) peak source counts based on partial observations of region by JCMT SCUBA-2 at 850 μm.
[c] Class 0/I target counts determined by coincidence of known Class O/I sources and bright (>0.1 Jy $beam^{-1}$ at 850 μm) submillimeter peak emission.

Monitoring the youngest, deeply embedded protostellar YSOs (protostars) is complicated since the accretion itself is not directly observed but must be inferred through its heating effect on the enshrouding protostellar core (Johnstone et al. 2013). Determining the underlying timescales and amplitudes related to the accretion process is fundamental to understanding protostellar assembly, as they constrain the physical conditions within the inner envelope and disk.

Aside from the JCMT survey, limited YSO variability studies have also utilized Spitzer and Herschel (e.g., Billot et al. 2012; Rebull et al. 2015), confirming that young stars and YSOs vary across a wide range of timescales. At these higher frequencies, however, one must untangle source variability from changing optical depth conditions (MacFarlane et al. 2019a, 2019b; Baek et al. 2020). More recently, the mid-IR Wide-field Infrared Survey Explorer satellite has monitored YSOs (as part of its all-sky survey) with a 6 month cadence, yielding exceptional leverage for submillimeter monitoring surveys by linking directly the submillimeter and mid-IR variations and by providing access to less-embedded, older YSOs (Contreras Peña et al. 2020; Park et al. 2021). Combined, the submillimeter and mid-IR time domain surveys will recover the history of variability across the main accretion stage of stellar assembly.

FYST offers the best opportunity for achieving sufficient statistical samples of YSOs across epochs. With FYST, each star-forming field will be 4 deg^2 (Table 5), an order of magnitude larger area than those with the JCMT, while the map depth will be 5 mJy at 350 GHz (850 μm), 2.5 times deeper than that of the JCMT Transient Survey. Combined, FYST will monitor an order of magnitude more sources (Table 6). The FYST survey benefits from the uniqueness of its highest frequency, 850 GHz (350 μm), observations that probe closer to the peak of the protostellar envelope spectral energy distribution (SED) where the response to variability is stronger (Johnstone et al. 2013; Contreras Peña et al. 2020). The 850 GHz sensitivity per epoch, 60 mJy $beam^{-1}$, provides a fixed signal-to-noise ratio between 350 and 850 GHz for source spectral indices as shallow as $S_\nu \propto \nu^{2.5}$. Finally, FYST is designed for surveys and can effectively schedule epochs at a 2 week cadence, twice the cadence of the JCMT, to better match the heating timescale in the envelope (Johnstone et al. 2013).

The FYST monitoring plan requires 10 hr $year^{-1}$ per field. Thus, with 500 hr, we will monitor 10 fields for 5 yr each. Table 5 presents the observing times required to reach the depth requested while Table 6 lists the 10 target fields. These fields include seven low-mass star-forming regions presently observed by the JCMT, extending the 850 μm (350 GHz) time

line beyond a decade of monthly, or better, cadence. Broadening the range of SF conditions being explored, we add two relatively nearby (within 2 kpc) high-mass star-forming regions, where the individual sources will be more tightly packed, but the opportunity to observe rare events, such as FU Ori bursts, will be significantly enhanced. Lastly, the Galactic center, at a much greater distance (8 kpc), will provide an extreme Galactic environment that has not yet been monitored in the submillimeter.

10.3.2. Target-of-opportunity Potential for Explosive Transients and Tidal Disruption Events

Explosive transients (i.e., transient events that can only occur one time per source, such as SNe and GRBs) and TDEs have both been detected at (sub)millimeter frequencies (see Figure 17). The majority of the explosive transients arise due to shock waves generated as a relativistic shell expands into a medium. This shell is thought to be driven by a collimated jet, as opposed to a truly spherical shell. In the sense of having a relativistic jet drive shock waves into an external medium, TDEs can act similarly to GRBs.

Most (sub)millimeter detections in this field have arisen from variations in the synchrotron emission as the forward shock wave intersects the circumstellar medium or ISM. However, a reverse shock wave may propagate into expanding ejecta in the shell that fuels the GRB afterglow. Both shocks can be roughly modeled as broken power-law SEDs, with the SED peak of each component expected to move toward lower frequencies with time after the explosion. Although the reverse shock is typically thought to be much brighter than the forward shock (the latter of which is often the focus for near-IR and higher frequencies), the reverse shock must be caught soon after the jet is launched because the peak of the reverse shock SED at a given time is at a much lower frequency than that of the forward shock. If detected, reverse shocks can play an important role in constraining the magnetization and bulk Lorentz factor of the jets driving this emission. To the first order, at FYST frequencies the reverse shock of GRB afterglows with higher magnetic field densities will be brighter, while having their reverse shock peaks at slightly earlier times; similarly, GRB afterglows with lower initial Lorentz factors will have their reverse shocks peak at later times, while being a little less bright (see Figure 6 in Urata et al. 2015). While radio emission can also play a role in detecting reverse shocks, the best constraints come from systems that can be observed at submillimeter-to-radio frequencies.

In Figure 17, we summarize the millimeter–submillimeter detections of core-collapse SNe, faint blue optical transients (FBOTs), long-duration GRBs (LGRBs), low-luminosity GRBs (LLGRBs), and TDEs. While most CCSNe will be too faint for FYST, 7 mJy detection limit 350 GHz observations would track the rest of the source classes' submillimeter evolution on timescales from $\lesssim$10 days (GRBs) to 100 days at reasonable distances (100–300 Mpc for FBOTs and some LLGRBs, 1 Gpc for brighter LGRBs and TDEs). Fainter 3 mJy detection limits (and the sensitivity to $\sim$50% farther sources) are more suitable for 220 and 280 GHz (see Table 5). Although the displayed CCSNe (SN 1993J, SN 2008D, SN 2011df, and SN 2020oi) are relatively faint millimeter–submillimeter sources, radio lightcurves of other SNe (SNe 2009bb, 2003L, 2003bg, and 2007bg) suggest that there exists a larger sample of SNe that may be similarly luminous (sub)millimeter transients as compared to the FBOTs AT2018cow and AT2020xnd (Ho et al. 2019, 2022). In addition, the radio luminosities of other FBOTs have peak radio spectral luminosities that are as bright or brighter than those of AT2018cow and AT2020xnd. FYST is well suited for early detection and characterization of the reverse shock (or detection limits on the reverse shock strength), provided that scheduling allows FYST to get on the source within a few hours. Compared to GRBs, the longer delay of the rise from the initial detection makes FBOTs easier targets to schedule for FYST observations. We note, however, that the underlying rates of sufficiently bright sources for FYST are poorly known at this time, and are expected to amount to no more than a few sources per year.

The deep survey (DSS) is sensitive to transient events like those listed above; however, the DSS has a limited angular extent. Therefore, it is unlikely to catch many (and possibly any) such transients. We may instead consider that target-of-opportunity (ToO) observations triggered by other observatories would enable FYST to help answer significant questions in this regime. While there may only be a handful of such sources over a few years, FYST could target southern sources that cannot easily be observed multiple times at 220–850 GHz by other facilities (for instance due to telescope pressure on ALMA) or target bright sources where FYST's uniquely sensitive 850 GHz window could provide needed high-frequency detections.

Finally, FYST could play a significant role in identifying potential submillimeter counterparts of multimessenger astrophysical sources. Although short GRBs tend to be less luminous than long GRBs, the association of short GRBs with gravitational-wave events from neutron star mergers (Abbott et al. 2017) makes targeted FYST follow-up of gravitational-wave (GW) events another priority. When FYST comes online, the typical uncertainty region of a gravitational-wave event will be well matched to the smaller areas considered in surveys like the transient YSO survey. Similarly, astrophysical neutrinos (which may be connected to blazar activity or other transient events; IceCube Collaboration 2018) also have an uncertain localization that is well matched to the capacities of FYST. Thus, FYST can efficiently cover wide patches of the sky for gravitational-wave and neutrino triggers to potentially localize their electromagnetic counterparts. Targeting southern GW events from merging neutron stars within 200 Mpc provides a relatively well-constrained program that could detect such sources down to one-tenth the brightness of GRBs 030329, 100418A, or 120326A (both for gravitational-wave events with no prompt electromagnetic counterpart and those where the electromagnetic counterpart has been identified at another frequency). Similarly, targeting a subset of the tens of neutrino triggers per year provides a second relatively well-constrained program.

The details of ToO implementation within FYST have not yet been determined. The time-constrained nature of ToOs will naturally use relatively limited telescope resources (e.g., 1 hr per nonlocalized trigger, 5–20 $\times$ 1 hr epochs per localized FBOT, GRB, TDE, or multimessenger counterpart). ToOs can play a role in optimizing telescope use through observing at 220 and 280 GHz during poor weather conditions. Observing at higher frequencies in better weather conditions for high-impact targets will need to be balanced with other FYST scientific programs (see Table 5 for example sensitivities). Dependent on

the final implementation of a ToO program, there is potential for FYST to make major advancements in explosive transients, TDEs, and especially multimessenger astronomy.

10.3.3. The Fast and the Furious

Magnetic reconnection events in stellar flares have been detected at millimeter and submillimeter wavelengths from young objects such as M dwarf and T Tauri stars, as well as chromospherically active binaries whose dwarf star may be about to arrive, or recently has arrived, on the main sequence (Bower et al. 2003; Mairs et al. 2019; MacGregor et al. 2020; Guns et al. 2021; Naess et al. 2021). While commensal observations (see Section 10.2) will capture a significant number of stellar flares, some nearby sources that undergo multiple flares per day reaching 100 mJy (e.g., Proxima Cen; MacGregor et al. 2020) in 30 s could be targeted by FYST. Other stellar flaring sources have flares that reach 900 mJy and decay over 15 minute timescales; these may be captured commensally in the protostellar survey (e.g., the T Tauri Binary System JW 566; Mairs et al. 2019). These interesting, bright events have usually gone undetected, as few data sets have been analyzed at the necessarily rapid timescales. Nevertheless, they are already revealing the presence of high-energy electrons during the flares, while constraining the density and magnetic field (MacGregor et al. 2020).

During transient outbursts of stellar-mass black holes accreting from nearby stars (i.e., black hole X-ray binaries), a relativistic jet may be launched. This is an important outflow event that is connected to accretion inflow through poorly understood physics. While astronomers have largely used radio observations to probe the jet properties of this connection, the submillimeter regime provides a much-needed tracer of the jet properties closer to the black hole. Radio and submillimeter observations of black hole X-ray binaries have demonstrated that the jets from X-ray binaries can vary significantly on day-to-day timescales (e.g., Russell et al. 2013). By measuring the evolution of an approximately broken power-law SED whose break frequency travels through the submillimeter to the radio, sophisticated models can constrain the evolving power injected into the jet base, the radius of the jet base, the location where particle acceleration in the jets starts, and the slope of the injected nonthermal particle distribution (Lucchini et al. 2021). These properties can, in turn, be connected to the accretion inflow properties measured by the X-ray emission. Moreover, recent observations have shown that the most extreme sources (e.g., V404 Cyg and MAXI J1820+070) demonstrate submillimeter variability on timescales as fast as tens of seconds (Tetarenko et al. 2017, 2021). Combined with simultaneous multiwavelength observations, this rapid variability can reveal poorly understood jet properties, like how the jet shape changes with distance from where particles are first accelerated.

FYST can provide the critical submillimeter data through short campaigns where an object is observed nightly for a short period of time over multiple frequencies (a handful of X-ray binaries per year reach $\sim$5 mJy flux-density levels, where FYST sensitivity in a 6 hr multiple camera observation is sufficient for detecting the sources in the submillimeter at 220–410 GHz; see Table 5). FYST could also observe for long periods during a single night to detect the most rapid variability (e.g., 30 s) in a single camera for sources with bright rapid flares (e.g., brighter flares from young stars at 100–800 mJy or X-ray binaries at 100–8000 mJy). As with the case for GRBs, TDEs, and multimessenger sources, even a small number of campaigns can make a large impact to the burgeoning field of rapid submillimeter variability.

11. Summary

The CCAT-prime Consortium is building the 6 m aperture FYST to be sited at more than 5600 m elevation on Cerro Chajnantor in northern Chile. Our science cases center on large-scale mapping at very high sensitivity in the submillimeter-to-millimeter-wave telluric windows and are enabled by the wide-field of view and excellent surface accuracy of FYST, together with the excellent site and dedicated instrumentation. Our primary science instruments are the CHAI and the Prime-Cam direct-detection instrument. Prime-Cam consists of seven instrument modules, two EoR-Spec imaging spectrometer modules, and five imaging polarimeters, one each at 220, 280, 350, 410, and 850 GHz. The focal planes of each module are KID arrays filling the available 1°.3 diameter image plane with diffraction-limited pixels. The Prime-Cam instrument on the FYST telescope sited on Cerro Chajnantor is a combination that promises unsurpassed mapping speeds, enabling our science goals.

Our science programs are survey-centered. The primary surveys are the WFS and the DSS, which enable much of our science program. Each of these will take 4000 hr of the top three weather quartiles each to complete. In addition, we have narrower or shallower programs to address first-light or demonstration science.

We have discussed at length our planned science program in Sections 4 through 10 above. Here we summarize our main goals and expectations.

1. *Reionization and galaxy evolution traced through LIM.* We will use EoR-Spec to map the large-scale spatial distribution of the 158 μm [C II] and the 88 μm [O III] lines to outline large-scale structures from the EoR to cosmic noon. This LIM thereby yields constraints on structure formation and growth, the reionization process, and the formation and growth of galaxies.
2. *Dusty galaxy evolution traced in far-infrared surveys.* The multiband, wide-area, and deep continuum surveys enabled by Prime-Cam will constrain FIR luminosities and therefore cosmic SF histories of galaxies from $z \sim 1$ to 5; advance studies of the evolution of high-luminosity DSFGs at high z into present-day elliptical galaxies; and reveal *exotic* sources such as extreme luminosity protoclusters or the rare, very strongly lensed galaxies at high z.
3. *Improving constraints on primordial gravitational waves through removal of galactic foregrounds.* By combining submillimeter Prime-Cam measurements with longer wavelength data from SO, we will improve our understanding of polarized dust foregrounds to help searches for primordial gravitational waves. In particular, Prime-Cam measurements have the potential to reduce bias in constraints on the tensor-to-scalar ratio, r, from SO and thereby aid in constraining models of the early universe such as cosmic inflation.
4. *Constraints on the role of magnetic fields in star formation, MHD turbulence, and dust grain composition as revealed through polarimetric imaging.* Prime-Cam will map hundreds of molecular clouds in polarized dust emission at high fidelity on scales ranging from entire

clouds down to the scales where individual stellar systems form. This will enable detailed studies of the role of magnetic fields in the formation of molecular clouds and support of dense substructures against gravitational collapse. These observations will also allow the investigation of magnetized turbulence in the ISM, while the high-frequency coverage will enable tests of models of dust grain composition as a function of density and environment.

5. *Galaxy and cluster evolution revealed through SZ effects.* Prime-Cam will provide broad coverage of the tSZ increment at 5 – 20 times better resolution than currently available. Combining this spectral coverage with SO observations, Prime-Cam will enable the clean separation of SZ signals from correlated thermal dust emission. This separation provides unbiased observational windows into the thermodynamic properties of galaxies and clusters, the dust-to-gas mass ratio of the ICM, cosmic-ray populations, and magnetic field strengths in the ICM.
6. *The recombination epoch traced through Rayleigh scattering.* Prime-Cam observations, together with data from other observatories such as SO and Planck, will place limits on CMB Rayleigh scattering. Atmospheric sky noise and foreground contamination are serious challenges to signal detection, but data from the multifrequency large-scale surveys with Prime-Cam on FYST promise to help significantly in both regards. The additional cosmological information provided by Rayleigh scattering motivates continued efforts in this direction.
7. *Astrophysical phenomena tracked in the time domain*. Prime-Cam will dramatically improve our understanding of the submillimeter time-domain universe. This will be achieved through both commensal monitoring of the primary WFS and DSS survey regions and specially crafted targeted campaigns. Together, these approaches will allow for the systematic study of submillimeter variability, on timescales from seconds to many years, monitoring sources with both thermal and nonthermal origins, from YSOs through supermassive black holes.

The FYST telescope is under construction by Vertex Antennentechnik-GMBH in Germany and will begin to be assembled at the Cerro Chajnantor site in the fall of 2022. Five of the seven instrument modules (the 280, 350, and 850 GHz polarization-sensitive camera modules and the two EoR-Spec modules) are funded and under construction at Cornell and partner institutions. First light is anticipated in late 2023.

We thank an anonymous referee for the very complete comments, criticisms, and requests for clarifications of earlier drafts of this manuscript.

The CCAT-prime project, FYST telescope, and Prime-Cam instrument have been supported by generous contributions from Fred Young, Cornell University, and the Canada Foundation for Innovation and the Provinces of Ontario, Alberta, and British Columbia. The construction of the FYST telescope was supported by the Großgeräte-Programm of the German Science Foundation (Deutsche Forschungsgemeinschaft, DFG) under grant INST 216/733-1 FUGG. The construction of the EoR-Spec instrument module for Prime-Cam is supported by NSF grant AST-2009767. The construction of the 350 GHz instrument module for Prime-Cam is supported by NSF grant AST-2117631.

M.A. acknowledges partial support from Fondecyt through grant 1211951. M.A. has been supported by the grant "CONICYT + PCI + INSTITUTO MAX PLANCK DE ASTRONOMIA MPG190030" and "CONICYT+PCI+REDES 190194." S.K.C. acknowledges support from NSF award AST-2001866. S.E.C. acknowledges support by the Friends of the Institute for Advanced Study Membership, and by the National Science Foundation under grant No. 2106607. F.B. acknowledges funding from the European Research Council (ERC) under the European Union's Horizon 2020 research and innovation program (grant agreement No.726384/Empire). L. M.F. acknowledges support from an NSERC Discovery grant (RGPIN-2020-06266). S.F. is supported in part by the Government of Canada through the Department of Innovation, Science and Industry Canada and by the Province of Ontario through the Ministry of Colleges and Universities. P.G. is sponsored (in part) by the Chinese Academy of Sciences (CAS), through a grant to the CAS South America Center for Astronomy (CASSACA) in Santiago, Chile, by the "Comisión Nacional de Ciencia y Tecnología (CONICYT)" via Project FONDECYT de Iniciación 11170551. D.J. is supported by the National Research Council of Canada and by an NSERC Discovery grant. E.K. is supported in part by the Excellence Cluster ORIGINS, which is funded by the Deutsche Forschungsgemeinschaft (DFG, German Research Foundation) under Germany's Excellence Strategy −EXC-2094 −390783311. P.D.M. acknowledges support from the Netherlands organization for scientific research (NWO) VIDI grant (dossier 639.042.730). J.M. is supported by the US Department of Energy under grant no. DE-SC0010129. D.R. acknowledges support from the National Science Foundation under grant numbers AST-1614213 and AST-1910107. M.D. N. acknowledges support from NSF grant AST-2117631. D.R. also acknowledges support from the Alexander von Humboldt Foundation through a Humboldt Research Fellowship for Experienced Researchers. E.R. acknowledges the support of the Natural Sciences and Engineering Research Council of Canada (NSERC), funding reference number RGPIN-2017-03987. University of Cologne and University Bonn CCAT-prime members acknowledge support by the Collaborative Research Centre 956 funded by the Deutsche Forschungsgemeinschaft (DFG) project ID 184018867. G.R.S. acknowledges support from NSERC Discovery grants (RGPIN-2016-06569 and RGPIN-2021-04001). G.J.S. acknowledges support from the National Science Foundation under grant numbers AST-1716229 and AST-2009767, and NASA grant NNX16AC72G. A.S. gratefully acknowledges funding support through Fondecyt Regular (project code 1180350) and from the Chilean Centro de Excelencia en Astrofísica y Tecnologías Afines (CATA) BASAL grant AFB-170002. D.T. C. is supported by a CITA/Dunlap Institute postdoctoral fellowship. The Dunlap Institute is funded through an endowment established by the David Dunlap family and the University of Toronto.[54]

ORCID iDs

Manuel Aravena https://orcid.org/0000-0002-6290-3198
Jason E. Austermann https://orcid.org/0000-0002-6338-0069
Kaustuv Basu https://orcid.org/0000-0001-5276-8730

[54] https://www.overleaf.com/project/60f8597c20bff1785f12c72e

Nicholas Battaglia https://orcid.org/0000-0001-5846-0411
Frank Bertoldi https://orcid.org/0000-0002-1707-1775
Frank Bigiel https://orcid.org/0000-0003-0166-9745
J. Richard Bond https://orcid.org/0000-0003-2358-9949
Patrick C. Breysse https://orcid.org/0000-0001-8382-5275
Ricardo Bustos https://orcid.org/0000-0001-8468-9391
Scott C. Chapman https://orcid.org/0000-0002-8487-3153
Steve K. Choi https://orcid.org/0000-0002-9113-7058
Dongwoo T. Chung https://orcid.org/0000-0003-2618-6504
Susan E. Clark https://orcid.org/0000-0002-7633-3376
Jens Erler https://orcid.org/0000-0002-5486-6745
Michel Fich https://orcid.org/0000-0002-5903-1886
Laura M. Fissel https://orcid.org/0000-0002-4666-609X
Simon Foreman https://orcid.org/0000-0002-0190-2271
Pablo García https://orcid.org/0000-0002-8586-6721
Martha P. Haynes https://orcid.org/0000-0001-5334-5166
Brandon Hensley https://orcid.org/0000-0001-7449-4638
Terry Herter https://orcid.org/0000-0002-3856-8385
Ronan Higgins https://orcid.org/0000-0001-8195-3900
Douglas Johnstone https://orcid.org/0000-0002-6773-459X
Christos Karoumpis https://orcid.org/0000-0003-3259-7457
Laura C. Keating https://orcid.org/0000-0001-5211-1958
Eiichiro Komatsu https://orcid.org/0000-0002-0136-2404
Benjamin Magnelli https://orcid.org/0000-0002-6777-6490
Brenda C. Matthews https://orcid.org/0000-0003-3017-9577
Joel Meyers https://orcid.org/0000-0001-8510-2812
Michael D. Niemack https://orcid.org/0000-0001-7125-3580
Yoko Okada https://orcid.org/0000-0002-6838-6435
Dominik A. Riechers https://orcid.org/0000-0001-9585-1462
Erik Rosolowsky https://orcid.org/0000-0002-5204-2259
Anirban Roy https://orcid.org/0000-0001-5729-0246
Sarah I. Sadavoy https://orcid.org/0000-0001-7474-6874
Reinhold Schaaf https://orcid.org/0000-0003-4850-5609
Peter Schilke https://orcid.org/0000-0003-2141-5689
Douglas Scott https://orcid.org/0000-0002-6878-9840
Robert Simon https://orcid.org/0000-0003-2555-4408
Adrian K. Sinclair https://orcid.org/0000-0003-0064-6867
Gregory R. Sivakoff https://orcid.org/0000-0001-6682-916X
Gordon J. Stacey https://orcid.org/0000-0003-1260-5448
Amelia M. Stutz https://orcid.org/0000-0003-2300-8200
Juergen Stutzki https://orcid.org/0000-0001-7658-4397
Mehrnoosh Tahani https://orcid.org/0000-0001-8749-1436
Karun Thanjavur https://orcid.org/0000-0003-1187-2544
Michael R. Vissers https://orcid.org/0000-0003-2467-7801
Simon D. M. White https://orcid.org/0000-0002-1061-6154

References

Abazajian, K., Addison, G., Adshead, P., et al. 2019, arXiv:1907.04473
Abbott, B. P., Abbott, R., Abbott, T. D., et al. 2017, ApJL, 848, L12
Adachi, S., Aguilar Faúndez, M. A. O., Arnold, K., et al. 2020, ApJ, 904, 65
Ade, P. A. R., Anderson, C. J., Barrentine, E. M., et al. 2020, JLTP, 199, 1027
Aihara, H., Armstrong, R., Bickerton, S., et al. 2018, PASJ, 70, S8
Aiola, S., Calabrese, E., Maurin, L., et al. 2020, JCAP, 2020, 047
Aitken, D. K., Smith, C. H., & Roche, P. F. 1989, MNRAS, 236, 919
Albrecht, A., & Steinhardt, P. J. 1982, PhRvL, 48, 1220
Alipour, E., Sigurdson, K., & Hirata, C. M. 2015, PhRvD, 91, 083520
Allen, A., Li, Z.-Y., & Shu, F. H. 2003, ApJ, 599, 363
Alonso, D., Sanchez, J., Slosar, A. & LSST Dark Energy Science Collaboration 2019, MNRAS, 484, 4127
Álvarez-Gutiérrez, R. H., Stutz, A. M., Law, C. Y., et al. 2021, ApJ, 908, 86
Amodeo, S., Battaglia, N., Schaan, E., et al. 2021, PhRvD, 103, 063514
Andersson, B.-G., Lazarian, A., & Vaillancourt, J. E. 2015, ARA&A, 53, 501
André, P., Di Francesco, J., Ward-Thompson, D., et al. 2014, Protostars and Planets VI (Tucson, AZ: Univ. Arizona Press), 27
Aravena, M., Decarli, R., Walter, F., et al. 2016, ApJ, 833, 68
Armitage, P. J. 2015, arXiv:1509.06382
Ashton, P. C., Ade, P. A. R., Angilè, F. E., et al. 2018, ApJ, 857, 10
Audard, M., Ábrahám, P., Dunham, M. M., et al. 2014, in Protostars and Planets VI, ed. H. Beuther et al. (Tucson, AZ : Univ. Arizona Press), 387
Austermann, J., Aird, K. A., Beall, J. A., et al. 2012, Proc. SPIE, 8452, 84521E
Austermann, J. E., Beall, J. A., Bryan, S. A., et al. 2018, JLTP, 193, 120
Bae, J., Hartmann, L., Zhu, Z., & Nelson, R. P. 2014, ApJ, 795, 61
Baek, G., MacFarlane, B. A., Lee, J.-E., et al. 2020, ApJ, 895, 27
Bardeen, J. M., Steinhardt, P. J., & Turner, M. S. 1983, PhRvD, 28, 679
Bashinsky, S., & Seljak, U. 2004, PhRvD, 69, 083002
Basu, K., Erler, J., Chluba, J., et al. 2019, BAAS, 51, 302
Basu, S., Ciolek, G. E., Dapp, W. B., & Wurster, J. 2009, NewA, 14, 483
Battaglia, N., Ferraro, S., Schaan, E., & Spergel, D. N. 2017, JCAP, 2017, 040
Beckwith, S. V. W., Stiavelli, M., Koekemoer, A. M., et al. 2006, AJ, 132, 1729
Behroozi, P., Wechsler, R. H., Hearin, A. P., & Conroy, C. 2019, MNRAS, 488, 3143
Beringue, B., Meerburg, P. D., Meyers, J., & Battaglia, N. 2021, JCAP, 2021, 060
Béthermin, M., Le Floc'h, E., Ilbert, O., et al. 2012, A&A, 542, A58
Béthermin, M., Wu, H.-Y., Lagache, G., et al. 2017, A&A, 607, A89
Billot, N., Morales-Calderón, M., Stauffer, J. R., Megeath, S. T., & Whitney, B. 2012, ApJL, 753, L35
Birkinshaw, M. 1999, PhR, 310, 97
Bleem, L. E., Bocquet, S., Stalder, B., et al. 2020, ApJS, 247, 25
Bleem, L. E., et al. 2015, ApJS, 216, 27
Bolatto, A. D., Wolfire, M., & Leroy, A. K. 2013, ARA&A, 51, 207
Bonafede, A., Govoni, F., Feretti, L., et al. 2011, A&A, 530, A24
Borlaff, A. S., Lopez-Rodriguez, E., Beck, R., et al. 2021, ApJ, 921, 128
Bower, G. C., Plambeck, R. L., Bolatto, A., et al. 2003, ApJ, 598, 1140
Bowman, J. D., Rogers, A. E. E., Monsalve, R. A., Mozdzen, T. J., & Mahesh, N. 2018, Natur, 555, 67
Breysse, P. C., & Alexandroff, R. M. 2019, arXiv:1904.03197
Breysse, P. C., Kovetz, E. D., & Kamionkowski, M. 2015, MNRAS, 452, 3408
Breysse, P. C., & Rahman, M. 2017, MNRAS, 468, 741
Brisbin, D., Miettinen, O., Aravena, M., et al. 2017, A&A, 608, A15
Burgarella, D., Buat, V., Gruppioni, C., et al. 2013, A&A, 554, A70
Cañameras, R., Nesvadba, N. P. H., Guery, D., et al. 2015, A&A, 581, A105
Calvo, M., Benoît, A., Catalano, A., et al. 2016, JLTP, 184, 816
Capitanio, L., Lallement, R., Vergely, J. L., Elyajouri, M., & Monreal-Ibero, A. 2017, A&A, 606, A65
Carilli, C. L., & Walter, F. 2013, ARA&A, 51, 105
Carlstrom, J. E., Holder, G. P., & Reese, E. D. 2002, ARA&A, 40, 643
Casey, C. M. 2016, ApJ, 824, 36
Casey, C. M., Berta, S., Béthermin, M., et al. 2012, ApJ, 761, 140
Casey, C. M., Narayanan, D., & Cooray, A. 2014, PhR, 541, 45
Casey, C. M., Hodge, J., Zavala, J. A., et al. 2018, ApJ, 862, 77
Chandrasekhar, S., & Fermi, E. 1953, ApJ, 118, 113
Chapman, S. C., Blain, A. W., Ivison, R. J., & Smail, I. R. 2003, Natur, 422, 695
Chapman, S. C., Blain, A. W., Smail, I., & Ivison, R. J. 2005, ApJ, 622, 772
Chapman, S. C., Ivison, R. J., Roseboom, I. G., et al. 2010, MNRAS, 409, L13
Chen, C.-Y., King, P. K., Li, Z.-Y., Fissel, L. M., & Mazzei, R. R. 2019, MNRAS, 485, 3499
Cheng, T., Clements, D., Greenslade, J., et al. 2019, MNRAS, 490, 3840
Cheng, Y.-T., Chang, T.-C., Bock, J., Bradford, C. M., & Cooray, A. 2016, ApJ, 832, 165
Cheng, Y.-T., Chang, T.-C., & Bock, J. J. 2020, ApJ, 901, 142
Chiang, Y.-K., Makiya, R., Komatsu, E., & Ménard, B. 2021, ApJ, 910, 32
Chiang, Y.-K., Makiya, R., Ménard, B., & Komatsu, E. 2020, ApJ, 902, 56
Chiar, J. E., Adamson, A. J, Whittet, D. C. B., et al. 2006, ApJ, 651, 268
Chluba, J., Nagai, D., Sazonov, S., & Nelson, K. 2012, MNRAS, 426, 510
Choi, S. K., Austermann, J., Basu, K., et al. 2020a, JLTP, 199, 1089
Choi, S. K., Hasselfield, M., Ho, S.-P. P., et al. 2020b, JCAP, 2020, 045
Chung, D. T., Viero, M. P., Church, S. E., & Wechsler, R. H. 2020, ApJ, 892, 51
Clark, S. E., & Hensley, B. S. 2019, ApJ, 887, 136
Clark, S. E., Hill, J. C., Peek, J. E. G., Putman, M. E., & Babler, B. L. 2015, PhRvL, 115, 241302
Colafrancesco, S., Marchegiani, P., de Bernardis, P., & Masi, S. 2013, A&A, 550, A92

Colafrancesco, S., Marchegiani, P., & Palladino, E. 2003, A&A, 397, 27
Concerto Collaboration, Ade, P., & Aravena, M. 2020, A&A, 642, A60
Contreras Peña, C., Johnstone, D., Baek, G., et al. 2020, MNRAS, 495, 3614
Contreras Peña, C., Lucas, P. W., Kurtev, R., et al. 2017, MNRAS, 465, 3039
Cormier, D., Madden, S. C, Lebouteiller, V., et al. 2015, A&A, 578, A53
Cortés, F., Cortés, K., Reeves, R., Bustos, R., & Radford, S. 2020, A&A, 640, A126
Cothard, N. F., Abe, M., Nikola, T., et al. 2018, Proc. SPIE, 10706, 107065B
Cothard, N. F., Choi, S. K., Duell, C. J., et al. 2020, JLTP, 199, 898
Coulton, W., Ota, A., & van Engelen, A. 2020, PhRvL, 125, 111301
Coulton, W. R., Beringue, B., & Meerburg, P. D. 2021, PhRvD, 103, 043501
Crites, A. T., Bock, J. J., Bradford, C. M., et al. 2014, Proc. SPIE, 9153, 91531W
D'Abrusco, R., Álvarez Crespo, N., Massaro, F., et al. 2019, ApJS, 242, 4
Dame, T. M., Ungerechts, H., Cohen, R. S., et al. 1987, ApJ, 322, 706
Danielson, A. L. R., Swinbank, A. M., Smail, I., et al. 2017, ApJ, 840, 78
Datta, R., Munson, C. D., Niemack, M. D., et al. 2013, ApOpt, 52, 8747
Davis, L. 1951, PhRv, 81, 890
De Bernardis, F., Stevens, J. R., Hasselfield, M., et al. 2016, Proc. SPIE, 9910, 991014
de Ugarte Postigo, A., Lundgren, A., Martin, S., et al. 2012, A&A, 538, A44
DeBoer, D. R., Parsons, A. R., Aguirre, J. E., et al. 2017, PASP, 129, 045001
Dharmawardena, T. E., Kemper, F., Wouterloot, J. G. A., et al. 2019, MNRAS, 489, 3492
Dicker, S. R., Gallardo, P. A, Gudmundsson, J. E., et al. 2018, Proc. SPIE, 10700, 107003E
Dickey, J. M., McClure-Griffiths, N., Gibson, S. J., et al. 2013, PASA, 30, e003
Dole, H., Lagache, G., Puget, J.-L., et al. 2006, A&A, 451, 417
Dolginov, A. Z., & Mitrofanov, I. G. 1976, Ap&SS, 43, 291
Donevski, D., Buat, V., Boone, F., et al. 2018, A&A, 614, 33
Draine, B. T., & Fraisse, A. A. 2009, ApJ, 696, 1
Draine, B. T., & Hensley, B. S. 2020, ApJ, 909, 94
Draine, B. T., & Li, A. 2007, ApJ, 657, 810
Draine, B. T., & Salpeter, E. E. 1979, ApJ, 231, 77
Duell, C. J., Vavagiakis, E. M., Austermann, J., et al. 2020, Proc. SPIE, 11453, 114531F
Dumitru, S., Kulkarni, G., Lagache, G., & Haehnelt, M. G. 2019, MNRAS, 485, 3486
Dunham, M. M., Allen, L. E., Evans, N. J., II, et al. 2015, ApJS, 220, 11
Dunham, M. M., Stutz, A. M., et al. 2014, in Protostars and Planets VI, ed. H. Beuther et al. (Tucson, AZ: Univ. Arizona Press), 195
Dunlop, J. S., McLure, R. J., Biggs, A. D., et al. 2017, MNRAS, 466, 861
Dutcher, D., Balkenhol, L, Ade, P. A. R., et al. 2021, PhRvD, 104, 022003
Dwek, E., & Arendt, R. G. 1992, ARA&A, 30, 11
Dwek, E., Rephaeli, Y., & Mather, J. C. 1990, ApJ, 350, 104
Dyck, H. M., Capps, R. W., Forrest, W. J., & Gillett, F. C. 1973, ApJL, 183, L99
Elbaz, D., Leiton, R., Nagar, N., et al. 2018, A&A, 616, A110
Elmegreen, B. G., & Scalo, J. 2004, ARA&A, 42, 211
Enßlin, T. A., & Kaiser, C. R. 2000, A&A, 360, 417
Erler, J., Basu, K., Chluba, J., & Bertoldi, F. 2018, MNRAS, 476, 3360
Faber, S. M., Wilmer, C. N. A., Wolf, C., et al. 2007, ApJ, 665, 265
Fan, X., Carilli, C. L., & Keating, B. 2006, ARA&A, 44, 415
Finlator, K., Özel, F., Davé, R., & Oppenheimer, B. D. 2009, MNRAS, 400, 1049
Fissel, L. M., Ade, P. A. R., Angilè, F. E., et al. 2016, ApJ, 824, 134
Fissel, L. M., Ade, P. A. R., Angilè, F. E., et al. 2019, ApJ, 878, 110
Foreman-Mackey, D. 2016, JOSS, 1, 24
Franco, M., Elbaz, D., Béthermin, M., et al. 2018, A&A, 620, A152
Fuhrmann, L., Larsson, S., Chiang, J., et al. 2014, MNRAS, 441, 1899
Fukui, Y., Kawamura, A., Minamidani, T., et al. 2008, ApJS, 178, 56
Gaensler, B. M., Landecker, T. L., Taylor, A. R. & POSSUM Collaboration 2010, BAAS, 42, 515
Galitzki, N., Ali, A., Arnold, K. S., et al. 2018, Proc. SPIE, 10708, 1070804
Galli, D., & Shu, F. H. 1993, ApJ, 417, 243
Giard, M., Montier, L., Pointecouteau, E., & Simmat, E. 2008, A&A, 490, 547
Girart, J. M., Rao, R., & Marrone, D. P. 2006, Sci, 313, 812
Gjergo, E., Palla, M., Matteucci, F., et al. 2020, MNRAS, 493, 2782
Gómez, G. C., Vázquez-Semadeni, E., & Zamora-Avilés, M. 2018, MNRAS, 480, 2939
Gómez-Guijarro, C., Riechers, D. A., Paveski, R., et al. 2019, ApJ, 872, 117
González Lobos, V., & Stutz, A. M. 2019, MNRAS, 489, 4771
González-López, J., Decarli, R., Pavesi, R., et al. 2019, ApJ, 882, 139
Graf, U. U., Honingh, N., Barrueto, I., et al. 2019, in Proc. of the 30th Int. Symp. on Space Terrahertz Technology (Red Hook, NY: Curran Associates), 77
Grishchuk, L. P. 1975, JETP, 40, 409
Gruppioni, C., Béthermin, M., Loiacono, F., et al. 2020, A&A, 643, A8
Gruppioni, C., Pozzi, F., Rodighiero, G., et al. 2013, MNRAS, 432, 23
Guillet, V., Fanciullo, L., Verstraete, L., et al. 2018, A&A, 610, A16
Guns, S., Forster, A., Daley, C., et al. 2021, ApJ, 916, 98
Guth, A. H. 1981, PhRvD, 23, 347
Guth, A. H., & S. Y., Pi 1982, PhRvL, 49, 1110
Hanany, S., Alvarez, M., Artis, E., et al. 2019, arXiv:1902.10541
Hartmann, L., & Kenyon, S. J. 1996, ARA&A, 34, 207
Hashimoto, T., Laporte, N., Mawatari, K., et al. 2018, Natur, 557, 392
Hasselfield, M., Hilton, M., Marriage, T. A., et al. 2013, JCAP, 2013, 008
Hawking, S. W. 1982, PhLB, 115, 295
Hazumi, M., Ade, P. A. R., Adler, A., et al. 2020, Proc. SPIE, 11443, 114432F
Hazumi, M., Ade, P. A. R., Akiba, Y., et al. 2019, JLTP, 194, 443
Heald, G., Mao, S., Vacca, V., et al. 2020, Galax, 8, 53
Henderson, S. W., Allison, R., Austermann, J., et al. 2016, JLTP, 184, 772
Hensley, B. S., & Bull, P. 2018, ApJ, 853, 127
Hensley, B. S., Clark, S. E., Fanfani, V., et al. 2021, ApJ, 929, 166
Hensley, B. S., & Draine, B. T. 2021, ApJ, 906, 73
Herczeg, G. J., Johnstone, D., Mairs, S., et al. 2017, ApJ, 849, 43
Heyer, M., & Dame, T. M. 2015, ARA&A, 53, 583
Hildebrand, R. H. 1988, QJRAS, 29, 327
Hildebrand, R. H., Kirby, L., Dotson, J. L., Houde, M., & Vaillancourt, J. E. 2009, ApJ, 696, 567
Hill, R., Chapman, S., Scott, D., et al. 2020, MNRAS, 495, 3124
Hilton, M., Sifón, C., Naess, S., et al. 2021, ApJS, 253, 3
Ho, A. Y. Q., Margalit, B., Bremer, M., et al. 2022, ApJ, 932, 116
Ho, A. Y. Q., Phinney, E. S., Ravi, V., et al. 2019, ApJ, 871, 73
Hodge, J. A., & da Cunha, E. 2020, RSOS, 7, 200556
Holland, W. S., Bintley, D., Chapin, E. L., et al. 2013, MNRAS, 430, 2513
Hopkins, P. F., Somerville, R. S., Hernquist, L., et al. 2006, ApJ, 652, 864
Hou, Z., Keisler, R., Knox, L., Millea, M., & Reichardt, C. 2013, PhRvD, 87, 083008
Houde, M., Vaillancourt, J. E., Hildebrand, R. H., Chitsazzadeh, S., & Kirby, L. 2009, ApJ, 706, 1504
Hu, Y., Lazarian, A., & Yuen, K. H. 2020, ApJ, 897, 123
Huang, N., Bleem, L. E., Stalder, B., et al. 2020, AJ, 159, 110
Hubmayr, J., Beall, J., Becker, D., et al. 2015, ApPhL, 106, 073505
Hull, C. L. H., & Zhang, Q. 2019, FrASS, 6, 3
Hurier, G., Macías-Pérez, J. F., & Hildebrandt, S. 2013, A&A, 558, A118
IceCube Collaboration, Aartsen, M. G., & Ackermann, M. 2018, Sci, 361, eaat1378
Inoue, T., Hennebelle, P., Fukui, Y., et al. 2018, PASJ, 70, S53
Inutsuka, S.-i., Inoue, T., Iwasaki, K., & Hosokawa, T. 2015, A&A, 580, A49
Itoh, N., Kohyama, Y., & Nozawa, S. 1998, ApJ, 502, 7
Jin, S., Daddi, E., Liu, D., et al. 2018, ApJ, 864, 56
Johnstone, D., Hendricks, B., Herczeg, G. J., & Bruderer, S. 2013, ApJ, 765, 133
Johnstone, D., Herczeg, G. J., Mairs, S., et al. 2018, ApJ, 854, 31
Kamenetzky, J., Privon, G. C., & Narayanan, D. 2018, ApJ, 859, 9
Kamionkowski, M., Kosowsky, A., & Stebbins, A. 1997a, PhRvL, 78, 2058
Kamionkowski, M., Kosowsky, A., & Stebbins, A. 1997b, PhRvD, 55, 7368
Kamionkowski, M., & Kovetz, E. D. 2016, ARA&A, 54, 227
Keating, G. K., Marrone, D. P., Bower, G. C., et al. 2016, ApJ, 830, 34
Keck Array & BICEP2 Collaborations 2018, PhRvL, 121, 221301
Kennicutt, R. C., & Evans, N. J. 2012, ARA&A, 50, 531
King, P. K., Fissel, L. M., Chen, C.-Y., & Li, Z.-Y. 2018, MNRAS, 474, 5122
Kitayama, T. 2014, PTEP, 2014, 06B111
Kogut, A., & Fixsen, D. J. 2016, ApJ, 826, 101
Komatsu, E., Bennett, C. L., Barnes, C., et al. 2014, PTEP, 2014, 06B102
Koukoufilippas, N., Alonso, D., Bilicki, M., & Peacock, J. A. 2020, MNRAS, 491, 5464
Kovetz, E. D., Viero, M. P., Lidz, A., et al. 2017, arXiv:1709.09066
Krumholz, M. R., & Federrath, C. 2019, FrASS, 6, 7
Lagache, G., Cousin, M., & Chatzikos, M. 2018, A&A, 609, A130
Lagache, G., Puget, J.-L., & Dole, H. 2005, ARA&A, 43, 727
Lee, Y.-H., Johnstone, D., Lee, J.-E., et al. 2020, ApJ, 903, 5
Lehmer, B. D., Brandt, W. N., Alexander, D. M., et al. 2005, ApJS, 161, 21
Lewis, A. 2013, JCAP, 2013, 053
Lewis, A. J. R., Ivison, R. J., Best, P. N., et al. 2018, ApJ, 862, 96
Li, A., & Draine, B. T. 2001, ApJ, 554, 778
Li, H.-B., & Henning, T. 2011, Natur, 479, 499
Li, T. Y., Wechsler, R. H., Devaraj, K., & Church, S. E. 2016, ApJ, 817, 169

Li, Z.-Y., Krasnopolsky, R., Shang, H., & Zhao, B. 2014, ApJ, 793, 130
Linde, A. D. 1982, PhLB, 108, 389
Liu, D., Daddi, E., Dickinson, M., et al. 2018, ApJ, 853, 172
Lucchini, M., Russell, T. D., Markoff, S. B., et al. 2021, MNRAS, 501, 5910
Lutz, D. 2014, ARA&A, 52, 373
Mac Low, M.-M., & Klessen, R. S. 2004, RvMP, 76, 125
MacFarlane, B., Stamatellos, D., Johnstone, D., et al. 2019a, MNRAS, 487, 5106
MacFarlane, B., Stamatellos, D., Johnstone, D., et al. 2019b, MNRAS, 487, 4465
MacGregor, A. M., Osten, R. A., & Hughes, A. M. 2020, ApJ, 891, 80
Madau, P., & Dickinson, M. 2014a, ARA&A, 52, 415
Madau, P., & Dickinson, M. 2014b, ARA&A, 52, 415
Magnelli, B., Lutz, D., Santini, P., et al. 2012, A&A, 539, A155
Magnelli, B., Popesso, P., Berta, S., et al. 2013, A&A, 553, 132
Mairs, S., Johnstone, D., Kirk, H., et al. 2016, MNRAS, 461, 4022
Mairs, S., Lalchand, B., Bower, G. C., et al. 2019, ApJ, 871, 72
Mairs, S., Lane, J., Johnstone, D., et al. 2017, ApJ, 843, 55
Makiya, R., Ando, S., & Komatsu, E. 2018, MNRAS, 480, 3928
Marrone, D. P., Spilker, J. S., Hayward, C. C., et al. 2018, Natur, 553, 51
Mason, R. E., Wright, G. S., Adamson, A., & Pendleton, Y. 2007, ApJ, 656, 798
Massaro, E., Maselli, A., Leto, C., et al. 2015, Ap&SS, 357, 75
Massi, M., Forbrich, J., Menten, K. M., et al. 2006, A&A, 453, 959
Masunaga, H., & Inutsuka, S.-i 2000, ApJ, 531, 350
Mathis, J. S., Mezger, P. G., & Panagia, N. 1983, A&A, 500, 259
McClure-Griffiths, N. M., Stanimirovic, S., Murray, C., et al. 2015, in Proc. of Science 215, Advancing Astrophysics with the Square Kilometre Array (AASKA14) (Trieste: SISSA), 130
Megeath, S. T., Gutermuth, R., Muzerolle, J., et al. 2016, AJ, 151, 5
Meisner, A. M., & Finkbeiner, D. P. 2015, ApJ, 798, 88
Meixner, M., Panuzzo, P., Roman-Duval, J., et al. 2013, AJ, 146, 62
Melin, J. B., Bartlett, J. G., Cai, Z. Y., et al. 2018, A&A, 617, A75
Miller, T. B., Chapman, S. C., Arevena, M., et al. 2018, Natur, 556, 469
Mittal, A., de Bernardis, F., & Niemack, M. D. 2018, JCAP, 2018, 032
Miville-Deschênes, M.-A. 2021, Miville-Deschenes et al. 2017 - Molecular Cloud Catalog, v1, Harvard Dataverse, doi:10.7910/DVN/QR9CFW
Miville-Deschênes, M. A., Duc, P. A., Marleau, F., et al. 2016, A&A, 593, A4
Miville-Deschênes, M.-A., Murray, N., & Lee, E. J. 2017, ApJ, 834, 57
Molinari, S., et al. 2016, A&A, 591, A149
Momferratos, G., Lesaffre, P., Falgarone, E., & Pineau des Forêts, G. 2014, MNRAS, 443, 86
Monsch, K., Pineda, J. E., Liu, H. B., et al. 2018, ApJ, 861, 77
Montier, L. A., & Giard, M. 2005, A&A, 439, 35
Moriwaki, K., Filippova, N., Shirasaki, M., & Yoshida, N. 2020, MNRAS, 496, 54
Mouschovias, T. C. 1991, ApJ, 373, 169
Mroczkowski, T., Nagai, D., Basu, K., et al. 2019, SSRv, 215, 17
Mukhanov, V. F., & Chibisov, G. V. 1981, JETPL, 33, 532
Murray, S. G., Power, C., & Robotham, A. S. G. 2013, A&C, 3, 23
Myers, P. C., Basu, S., & Auddy, S. 2018, ApJ, 868, 51
Naess, S., Battaglia, N., Bond, J. R., et al. 2021, ApJ, 915, 14
Nayakshin, S., & Lodato, G. 2012, MNRAS, 426, 70
Niemack, M. D. 2016, ApOpt, 55, 1686
Nozawa, S., Kohyama, Y., & Itoh, N. 2009, PhRvD, 79, 123007
Offner, S. S. R., Kratter, K. M., Matzner, C. D., Krumholz, M. R., & Klein, R. I. 2010, ApJ, 725, 1485
Ostriker, J., & Silk, J. 1973, ApJL, 184, L113
Oteo, I., Ivison, R. J., Dunne, L., et al. 2018, ApJ, 856, 72
Padmanabhan, H. 2019, MNRAS, 488, 3014
Padmanabhan, H., Breysse, P., Lidz, A., & Switzer, E. R. 2022, MNRAS, 515, 5813
Pandey, S., Baxter, E. J., Xu, Z., et al. 2019, PhRvD, 100, 063519
Pannella, M., Elbaz, D., Daddi, E., et al. 2015, ApJ, 807, 141
Park, W., Lee, J.-E., Contreras Peña, C., et al. 2021, ApJ, 920, 132
Parshley, S. C., Kronshage, J., Blair, J., et al. 2018a, Proc. SPIE, 10700, 107005X
Parshley, S. C., Niemack, M., Hills, R., et al. 2018b, Proc. SPIE, 10700, 1070041
Pattle, K., & Fissel, L. 2019, FrASS, 6, 15
Peek, J. E. G., Babler, B. L., Zheng, Y., et al. 2018, ApJS, 234, 2
Pelgrims, V., Clark, S. E., Hensley, B. S., et al. 2021, A&A, 647, A16
Planck Collaboration Int. XI, Ade, P. A. R., Aghanim, N., et al. 2013, A&A, 557, A52
Planck Collaboration Int. XIX, Ade, P. A. R., Aghanim, N., et al. 2015, A&A, 576, A104
Planck Collaboration Int. XLIII, Adam, R., Ade, P. A. R., et al. 2016, A&A, 596, A104
Planck Collaboration Int. XXII, Ade, P. A. R., Alves, M. I. R., et al. 2015, A&A, 576, A107
Planck Collaboration Int. XXXV, Ade, P. A. R., Aghanim, N., et al. 2016, A&A, 586, A138
Planck Collaboration IV, Akrami, Y., Ashdown, M., et al. 2020, A&A, 641, A4
Planck Collaboration VI, Aghanim, N., Akrami, Y., et al. 2020, A&A, 641, A6
Planck Collaboration XI, Akrami, Y., Ashdown, M., et al. 2020, A&A, 641, A11
Planck Collaboration XII, Aghanim, N., Akrami, Y., et al. 2020, A&A, 641, A12
Planck Collaboration XXII, Aghanim, N., Arnuad, M., et al. 2016, A&A, 594, A22
Planck Collaboration XXIX, Ade, P. A. R., Aghanim, N., et al. 2014, A&A, 571, A29
Planck Collaboration XXVII, Ade, P. A. R, Aghanim, N., et al. 2016, A&A, 594, A27
Polychroni, D., Schisano, E., Elia, D., et al. 2013, ApJL, 777, L33
Price, D. J., & Bate, M. R. 2007, Ap&SS, 311, 75
Purcell, E. M. 1979, ApJ, 231, 404
Radford, S. J. E., & Peterson, J. B. 2016, PASP, 128, 075001
Rayleigh, L. 1881, Lond. Edinb. Dublin Phil. Mag. J. Sci., 12, 81
Rebull, L. M., Stauffer, J. R., Cody, A. M., et al. 2015, AJ, 150, 175
Reissl, S., Stutz, A. M., Brauer, R., et al. 2018, MNRAS, 481, 2507
Reissl, S., Stutz, A. M., Klessen, R. S., Seifried, D., & Walch, S. 2021, MNRAS, 500, 153
Remazeilles, M., Delabrouille, J., & Cardoso, J.-F. 2011, MNRAS, 410, 2481
Remazeilles, M., Delabrouille, J., & Cardoso, J.-F. 2011c, MNRAS, 418, 467
Remazeilles, M., Dickinson, C., Eriksen, H. K. K., & Wehus, I. K. 2016, MNRAS, 458, 2032
Reuter, C., Vieira, J. D., Spilker, J. S., et al. 2020, ApJ, 902, 78
Riechers, D. A., Bradford, C. M., Clements, D. L., et al. 2013, Natur, 496, 329
Riechers, D. A., Carilli, C. L., Capak, P. L., et al. 2014, ApJ, 796, 84
Riechers, D. A., Hodge, J. A., Pavesi, R., et al. 2020, ApJ, 895, 81
Riechers, D. A., Leung, T. K. D., Ivison, R. J., et al. 2017, ApJ, 850, 1
Robertson, B. E., Ellis, R. S., Furlanetto, S. R., & Dunlop, J. S. 2015, ApJL, 802, L19
Robertson, B. E., Furlanetto, S. R., Schneider, E., et al. 2013, ApJ, 768, 71
Robishaw, T., Green, J., Surcis, G., et al. 2015, in Proc. of Science 215, Advancing Astrophysics with the Square Kilometre Array (AASKA14) (Trieste: SISSA), 110
Russell, D. M., Russell, T. D., Miller-Jones, J. C. A., et al. 2013, ApJL, 768, L35
Sadavoy, S. I., Stephens, I. W., Myers, P. C., et al. 2019, ApJS, 245, 2
Sadavoy, S. I., Stutz, A. M., Schnee, S., et al. 2016, A&A, 588, A30
Santos, M., Bull, P., Alonso, D., et al. 2015, in Proc. of Science 215, Advancing Astrophysics with the Square Kilometre Array (AASKA14) (Trieste: SISSA), 19
Sarazin, C. L. 1988, X-ray Emission from Clusters of Galaxies (Cambridge: Cambridge Univ. Press)
Sato, K. 1981, MNRAS, 195, 467
Schaan, E., Ferraro, S., Amodeo, S., et al. 2021, PhRvD, 103, 063513
Schaan, E., & White, M. 2021, JCAP, 2021, 068
Schillaci, A., Ade, P. A. R., Ahmed, Z., et al. 2020, JLTP, 199, 976
Schreiber, C., Elbaz, D., Pannella, M., et al. 2017, A&A, 602, A96
Schreiber, C., Pannella, M., Elbaz, D., et al. 2015, A&A, 575, A74
Seifried, D., Walch, S., Reissl, S., & Ibáñez-Mejía, J. C. 2019, MNRAS, 482, 2697
Seljak, U., & Zaldarriaga, M. 1997, PhRvL, 78, 2054
Serra, P., Doré, O., & Lagache, G. 2016, ApJ, 833, 153
Shu, F. H. 1977, ApJ, 214, 488
Shu, F. H., Adams, F. C., & Lizano, S. 1987, ARA&A, 25, 23
Silva, M., Santos, M. G., Cooray, A., & Gong, Y. 2015, ApJ, 806, 209
Simons Observatory Collaboration, Ade, P., Aguirre, J., et al. 2019, JCAP, 2019, 056
Smith, C. H., Wright, C. M., Aitken, D. K., Roche, P. F., & Hough, J. H. 2000, MNRAS, 312, 327
Smith, C. M. A., Gear, W. K., Smith, M. W. L., Papageorgiou, A., & Eales, S. A. 2019, MNRAS, 486, 4304
Soler, J. D., Ade, P. A. R., Angilè, F. E., et al. 2017, A&A, 603, A64
Soler, J. D., Hennebelle, P., Martin, P. G., et al. 2013, ApJ, 774, 128
Spinoglio, L., Dasyra, K. M., Franceschini, A., et al. 2012, ApJ, 745, 171
Springel, V., Pakmor, R., Pillepich, A., et al. 2018, MNRAS, 475, 676
Stacey, G. J. 2011, ITTST, 1, 241
Stacey, G. J., Geis, N., Genzel, R., et al. 1991, ApJ, 373, 423

Stacey, G. J., Hailey-Dunsheath, S., Ferkinhoff, C., et al. 2010, ApJ, 724, 957
Stacey, G. J., Parshley, S., Nikola, T., et al. 2014, Proc. SPIE, 9153, 91530L
Starobinsky, A. A. 1979, JETPL, 30, 682
Starobinsky, A. A. 1982, PhLB, 117, 175
Stein, G., Alvarez, M. A., & Bond, J. R. 2019, MNRAS, 483, 2236
Stein, G., Alvarez, M. A., Bond, J. R., van Engelen, A., & Battaglia, N. 2020, JCAP, 2020, 012
Stephens, I. W., Looney, L. W., Dowell, C. D., Vaillancourt, J. E., & Tassis, K. 2011, ApJ, 728, 99
Stevens, J. R., Goeckner-Wald, N., Keskitalo, R., et al. 2018, Proc. SPIE, 10708, 1070841
Stompor, R., Leach, S., Stivoli, F., & Baccigalupi, C. 2009, MNRAS, 392, 216
Strandet, M. L., Weiss, A., Vieira, J. D., et al. 2016, ApJ, 822, 80
Stutz, A. M., & Gould, A. 2016, A&A, 590, A2
Stutz, A. M., & Kainulainen, J. 2015, A&A, 577, L6
Subroweit, M., García-Marín, M., Eckart, A., et al. 2017, A&A, 601, A80
Sun, G., Chang, T.-C., Uzgil, B. D., et al. 2021, ApJ, 915, 33
Sun, G., Hensley, B. S., Chang, T.-C., Doré, O., & Serra, P. 2019, ApJ, 887, 142
Sun, G., Moncelsi, L., Viero, M. P., et al. 2018, ApJ, 856, 107
Sunyaev, R. A., & Zeldovich, Y. B. 1970, Ap&SS, 7, 3
Sunyaev, R. A., & Zeldovich, Y. B. 1972, CoASP, 4, 173
Switzer, E. R., Anderson, C. J., Pullen, A. R., & Yang, S. 2019, ApJ, 872, 82
Tahani, M., Plume, R., Brown, J. C., & Kainulainen, J. 2018, A&A, 614, A100
Tahani, M., Plume, R., Brown, J. C., Soler, J. D., & Kainulainen, J. 2019, A&A, 632, A68
Takahara, F., & Sasaki, S. 1991, PThPh, 86, 1021
Tetarenko, A. J., Casella, P., Miller-Jones, J. C. A., et al. 2021, MNRAS, 504, 3862
Tetarenko, A. J., Sivakoff, G. R., Miller-Jones, J. C. A., et al. 2017, MNRAS, 469, 3141
The CMB-S4 Collaboration, Abazajian, K., Addison, G. E., et al. 2020, ApJ, 926, 54
The CONCERTO Collaboration, Ade, P., Aravena, M., et al. 2020, A&A, 642, A60
Thorne, B., Dunkley, J., Alonso, D., & Næss, S. 2017, MNRAS, 469, 2821
Thornton, R., Ade, P. A. R., Aiola, S., et al. 2016, ApJS, 227, 21
Tristram, M., Banday, A. J., Górski, K. M., et al. 2021, A&A, 647, A128
Urata, Y., Huang, K., Asada, K., et al. 2015, AdAst, 2015, 165030
Vavagiakis, E. M., Ahmed, Z., Ali, A., et al. 2018, Proc. SPIE, 10708, 107081U
Vikram, V., Lidz, A., & Jain, B. 2017, MNRAS, 467, 2315
Vogelsberger, M., McKinnon, R., O'Neil, S., et al. 2019, MNRAS, 487, 4870
Vorobyov, E. I., & Elbakyan, V. G. 2018, A&A, 618, A7
Walch, S., Girichidis, P., Naab, T., et al. 2015, MNRAS, 454, 238
Walter, F., Decarli, R., Aravena, M., et al. 2016, ApJ, 833, 67
Wang, T., Schreiber, C., Elbaz, D., et al. 2019, Natur, 572, 211
Wechsler, R. H., & Tinker, J. L. 2018, ARA&A, 56, 435
Whitehorn, N., Natoli, T., Ade, P. A. R., et al. 2016, ApJ, 830, 143
Wielgus, M., Akiyama, K., Blackburn, L., et al. 2020, ApJ, 901, 67
Wolz, L., Blake, C., & Wyithe, J. S. B. 2017, MNRAS, 470, 3220
Wright, E. L. 1979, ApJ, 232, 348
Yan, Z., van Waerbeke, L., Tröster, T., et al. 2021, A&A, 651, A76
Yen, H.-W., Koch, P. M., Hull, C. L. H., et al. 2021, ApJ, 907, 33
Yu, Q., Spergel, D. N., & Ostriker, J. P. 2001, ApJ, 558, 23
Yue, B., Ferrara, A., Pallottini, A., Gallerani, S., & Vallini, L. 2015, MNRAS, 450, 3829
Zaldarriaga, M., & Seljak, U. 1997, PhRvD, 55, 1830
Zandanel, F., Pfrommer, C., & Prada, F. 2014, MNRAS, 438, 124
Zhu, Z., Hartmann, L., & Gammie, C. 2010, ApJ, 713, 1143